THE RELATIONSHIP OF SMALL EARTHQUAKES TO STRAIN ACCUMULATION ALONG MAJOR FAULTS IN SOUTHERN CALIFORNIA

Thesis by

James Christopher Pechmann

In Partial Fulfillment of the Requirements

for the Degree of

Doctor of Philosophy

California Institute of Technology

Pasadena, California

1983

(Submitted March 24, 1983)

To my wife, Judy,

and to my parents

ACKNOWLEDGEMENTS

I thank the faculty, students, and staff of the Seismological Laboratory and the Division of Geological and Planetary Sciences, who have made my years as a graduate student both enjoyable and rewarding. My thesis advisor, Hiroo Kanamori, was a pleasure to work with because of his exceptional scientific insight and his ready availability to students. Clarence Allen and Karen McNally provided guidance and encouragement with the work in Chapter 1. Bernard Minster, Dave Hadley, Carl Johnson, Jim Whitcomb, and Ed Corbett taught me a great deal about analysis of local network data and supplied numerous computer programs to facilitate this research. Discussions with Art Frankel were particularly helpful in organizing my thoughts for Chapter 4. Many other people have contributed to this thesis by supplying ideas, suggestions, or merciless reviews of preliminary versions of this work, including John Cipar, Gene Humphreys, Keith Echelmeyer, Judy Pechmann, Chris Sanders, Peter Molnar, Richard Strelitz, Don Helmberger, Steve Hartzell, Peter German, Tracy Johnson, Ronan LeBras, and Luciana Astiz.

This research would not have possible without the hard work throughout the years of the staff of the Caltech Seismological Laboratory and the U.S. Geological Survey in building and operating the Southern California Seismographic Network, archiving the network data, and doing all the first-order analysis of these data. Special credit must be given to Carl Johnson, who developed the CEDAR system for digital detection and recording of earthquakes.

During my first three years at Caltech I benefitted greatly from my association with Jay Melosh, who provided instruction, inspiration, and advice on some work not represented in this thesis. Don Potter at Hamilton College first introduced me to research, and gave me guidance and encouragement regarding graduate school.

I am indebted to my wife, Judy, for her personal support and patience. I am grateful to my fellow students and to the members of the Ingersoll house, past and present, for their companionship.

The professional-looking figures in this thesis were drafted by Joe Galvan and Laszlo Lenches. Roslyn Scherr and Terry Golley provided expert assistance with the typing.

This research was supported in part by the U.S. Geological Survey under contracts 14-08-0001-15258, 14-08-0001-19265, and 14-08-0001-19270, the NASA Office of Applications under grant NSG5224, and by the National Science Foundation under Grant EAR78-05352.

ABSTRACT

Fault-plane solutions for recent small ($M_L \leq 4.6$) earthquakes in the central Transverse Ranges, California, were determined using an azimuthally-varying crustal model. The dominant type of faulting observed is reverse faulting on east-striking planes, which suggests a regional stress field characterized by north-south compression. Some strike-slip faulting also occurs. There is some indication that strike-slip earthquakes may be more common than reverse-slip earthquakes during episodes of crustal dilatation (Sauber et al., 1983). The rate of north-south crustal shortening attributable to small earthquake deformation during 1974-1976 is two orders of magnitude smaller than the 0.3 parts per million per year north-south contraction measured at the surface by Savage et al. (1978). The scatter in earthquake hypocenters and general inconsistency of focal mechanisms with geologically determined motions on nearby major faults indicate that the small earthquakes in this region are not associated with large-scale block movements along major fault systems. Rather, they appear to represent fracturing along random minor zones of weakness in response to the regional stress field, or alternatively, small-scale block movements that are below the resolution of this study. Earthquakes in the San Gabriel Mountains north of the Santa Susana-Sierra Madre-Cucamonga frontal fault system tend to concentrate near the eastern and western ends of the range where good evidence for late Quaternary movement along the frontal faults has been found. Seismicity is markedly lower north

of the central section of the frontal fault system where evidence for late Quaternary movement is lacking.

Digitally-recorded waveforms of M_L 2.0-2.8 earthquakes that occurred in two small areas along the Imperial fault before and after it broke in the M_L 6.6 Imperial Valley earthquake on October 15, 1979, were examined and compared. Eight preshocks (1977-1979) from a $4^1/_2$ by $1^1/_2$ km area centered 4 km southeast of the mainshock epicenter have strikingly similar waveforms over the entire record length (~30 s), with an average peak cross correlation between seismograms of 0.74. The seismograms are well correlated at frequencies up to at least 4 Hz. This implies similar source mechanisms and hypocenters within $^1/_4$ of the 4-Hz wavelengths, i.e., <200-400 m. Five aftershocks from the same area show an average peak cross correlation between seismograms of only 0.23. Any associated changes in mechanism must be small because they are not reflected in the first motion data. Analysis of frequency content of these events using bandpass-filtering techniques showed no systematic temporal changes in spectral shape.

Ten preshocks and 24 aftershocks from a $1^1/_2$ by 2 km source area centered along the Imperial fault 16 km northwest of the 1979 mainshock epicenter were also studied. First motion data suggest that all of the aftershocks and a swarm of six preshocks on December 7-9, 1978, were associated with the main fault but that four earlier preshocks were not. The six preshocks on December 7-9, 1978, were tightly clustered, as evidenced by the strong similarity of the waveforms (most peak cross correlations >0.6). During this swarm the 8- to 16-Hz spectral

amplitude increased relative to the 1- to 2-Hz spectral amplitude over the whole record length by about a factor of 3, suggesting a systematic increase in stress drop. Groups of like events are also present among the aftershocks in this data set. The average peak correlation for pairs of aftershocks, 0.43, is almost the same as that for pairs of preshocks, 0.45, if all 10 preshocks are included. However, several sources appear to have been active simultaneously during the aftershock period so that no more than two to three consecutive aftershocks have maximum cross correlations ≥ 0.6.

A search was undertaken for earthquakes with similar waveforms within two small (<5 km) areas along the San Jacinto fault zone northwest of the Anza gap, but none were found. Focal mechanisms for most of the earthquakes in these two study areas agree very well with the faulting observed geologically at the surface. This, together with the concentration of hypocenters near the San Jacinto fault zone, suggests that small earthquakes are occurring along the main faults traces here, in contrast to the situation in the central Transverse Ranges.

The highly localized sources characterized by waveform similarity may represent fault asperities or clusters of asperities. The observations above are consistent with a decrease in the number of these asperities as the weaker ones fail under increasing stress during the intervals between large earthquakes.

TABLE OF CONTENTS

Page

Acknowledgements iii

Abstract v

Introduction 1

Chapter 1. Tectonic Implications of Small Earthquakes in the Central Transverse Ranges, California 9

Introduction 9

Seismicity, 1933-1977 13

Focal Mechanism Determinations 18

Results of Regional Focal Mechanism Study 27

Evidence for Temporal Changes in Focal Mechanisms 33

Conclusions 42

Chapter 2. Waveforms and Spectra of Preshocks and Aftershocks of the 1979 Imperial Valley, California, Earthquake: Evidence for Fault Heterogeneity? 45

Introduction 45

Selection of Events and Stations 50

Waveforms and Focal Mechanisms 62

Spectral Analysis 86

Discussion 98

Conclusions 107

Page

Chapter 3. A Preliminary Study of Waveforms of Small Earthquakes Along the San Jacinto Fault Zone, California 109

Introduction 109

Waveform Analysis 112

Focal Mechanisms 126

Conclusions 133

Chapter 4. Source Studies of Small Earthquakes: A Review 137

References 154

INTRODUCTION

The problem of the relationship of small earthquakes to strain accumulation along major faults is closely tied to fundamental problems in earthquake mechanics and earthquake prediction. Most earthquakes in southern California larger than about magnitude 6 occur on major faults that are recognizable from surface or subsurface geology and have a history of Quaternary displacements (Allen et al., 1965). Since most of the seismic energy release and moment release occurs during these larger earthquakes, they are clearly the most important from the standpoint of both tectonics and earthquake hazards. Smaller earthquakes, however, are much more numerous than larger earthquakes and could therefore provide some important information if their relationship to large earthquakes can be understood. This thesis presents some investigations of this relationship using focal mechanisms, waveforms, and spectra of small earthquakes in southern California.

In general, small earthquake activity and large earthquake activity are spatially related in only a very regional sense. During the last ten years, improved recording techniques and dramatic expansions of seismic arrays in both northern and southern California have led to much more accurate earthquake locations and lower detection thresholds. The locations from the northern and southern California arrays show contrasting patterns in the distribution of small earthquake hypocenters relative to major faults, as discussed by Allen (1981). In northern California (Figure I-1), most of the small earthquakes are concentrated

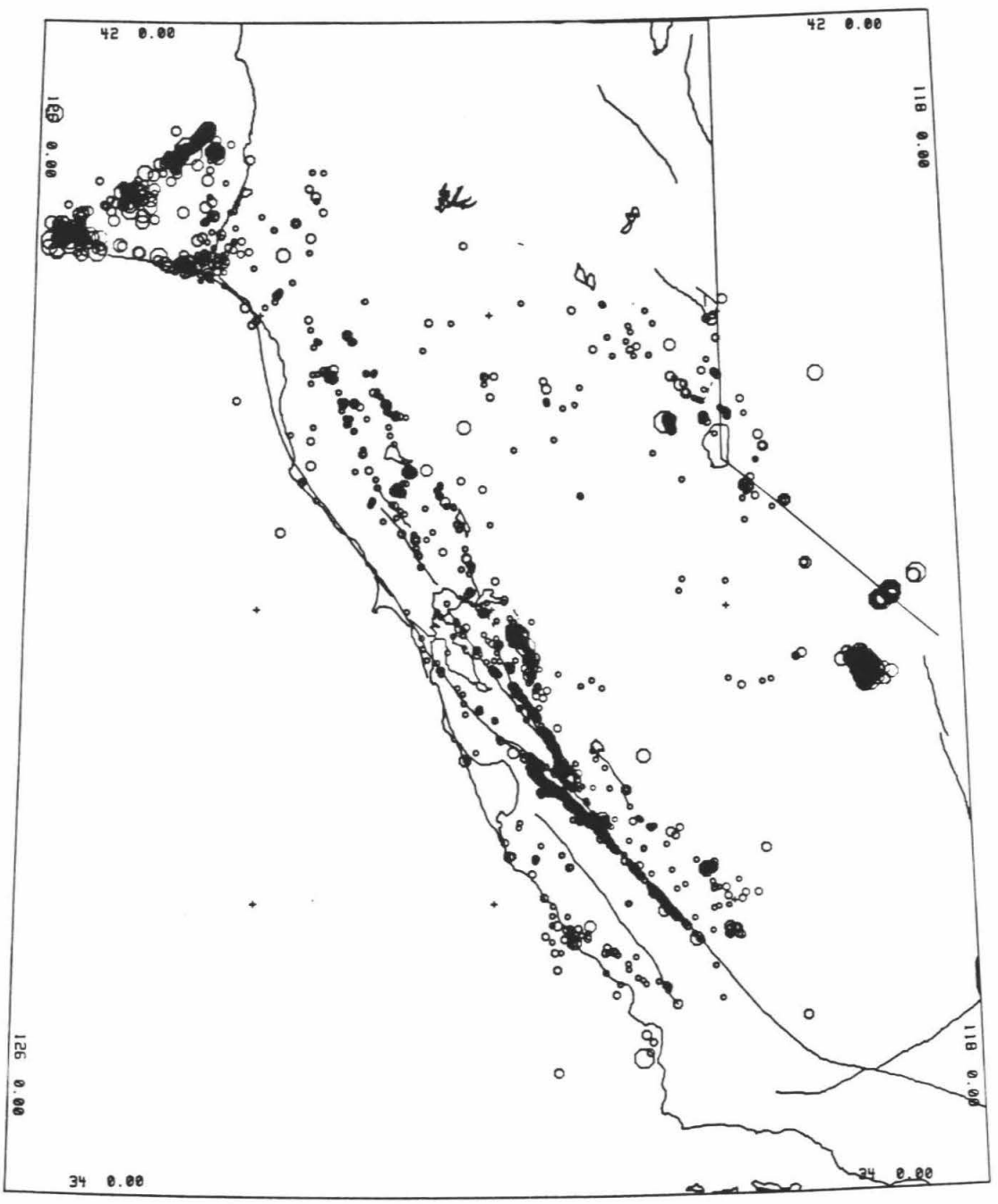

Figure I-1. Epicenters of earthquakes in central California for the year 1980, based on data from the U.S. Geological Survey Central California Seismographic Network. Figure courtesy of R. S. Cockerham, U.S. Geological Survey.

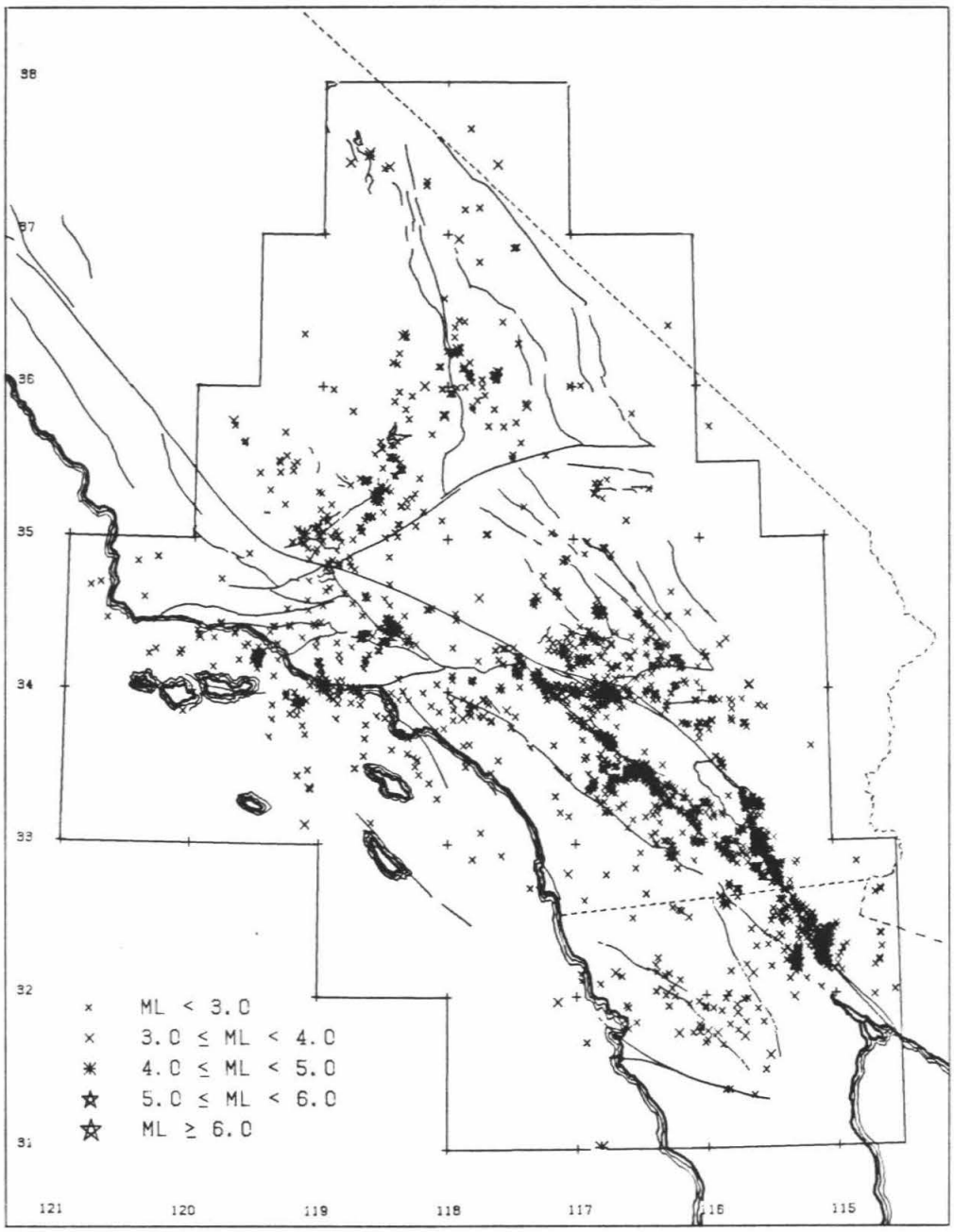

Figure I-2. Epicenters of earthquakes in the southern California region for the 6-month period January 1 to July 1, 1978. Outlined area is region of coverage of the California Institute of Technology/ U.S. Geological Survey Southern California Seismographic Network. Earthquake locations and magnitudes are from the Caltech/USGS catalog. Solid lines are major faults from Jennings et al. (1975). Some of these faults are identified in Figure I-3.

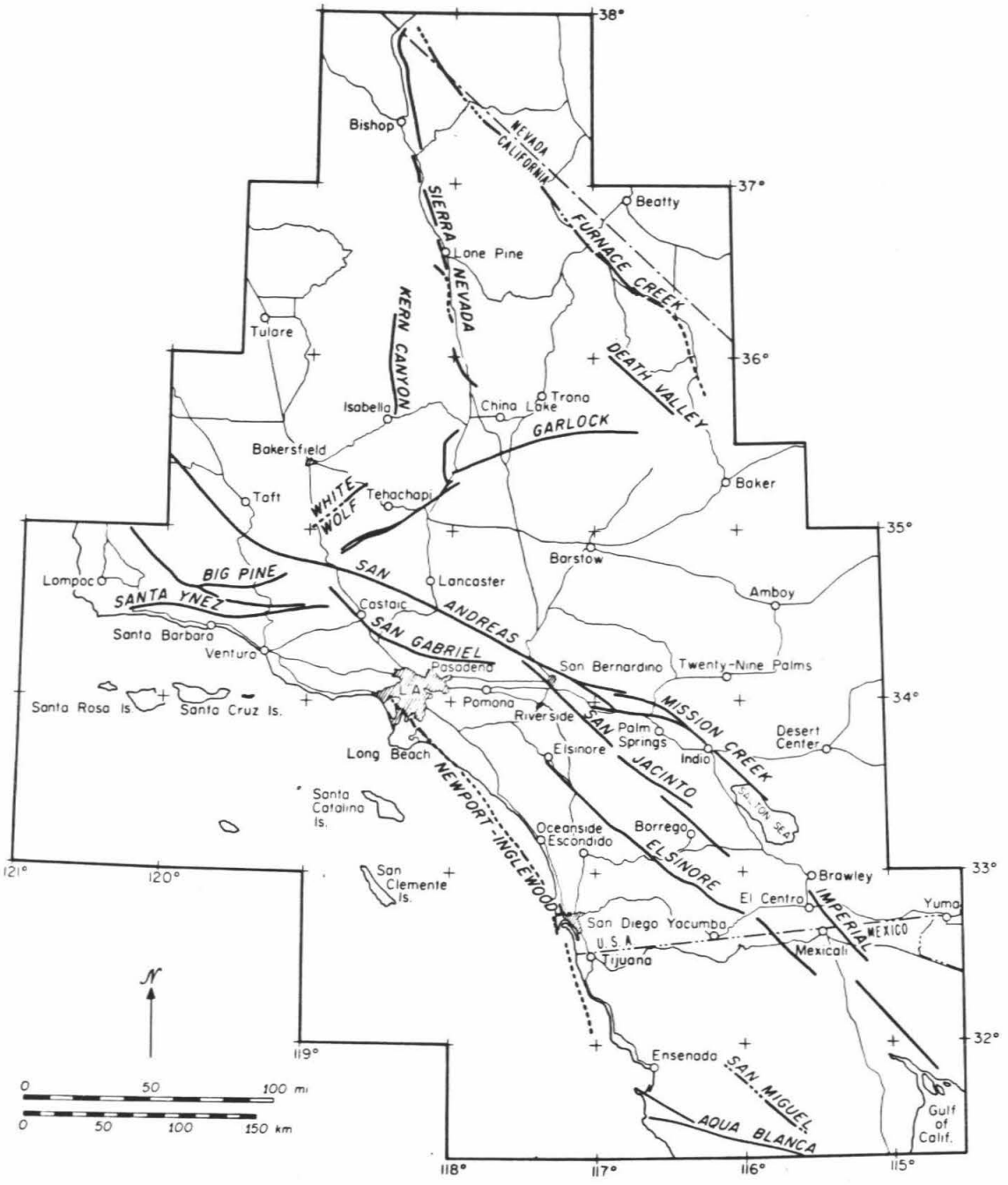

Figure I-3. Base map of southern California region with major faults. From Hileman et al. (1973).

in narrow zones along creeping segments of major strike-slip, vertical faults (Wesson et al., 1977). Their focal mechanisms are, in general, consistent with the long-term sense of slip along these faults (e.g., McNally and McEvilly, 1977). It is therefore reasonable to assume that most of them represent slip along the main fault traces. Other active fault segments in northern California are seismically quiescent at the present time. In southern California, the situation is somewhat more complicated. There are concentrations of activity along some important faults such as the San Jacinto and Imperial faults (Figures I-2, I-3), where evidence for fault creep has been found (Keller et al., 1978; Goulty et al., 1978). However, the seismicity elsewhere is very scattered. Even where lineations of seismicity exist, in detail the hypocenters do not always define simple fault traces. For instance, along the zone of seismicity connecting the northern end of the Imperial fault to the southern end of the Mission Creek branch of the San Andreas fault (Figures I-2, I-3), detailed studies have shown that many of the earthquakes are associated with structures transverse to the overall trend of this zone (Johnson and Hadley, 1976; Johnson, 1979; Hutton and Johnson, 1981; Johnson and Hutton, 1982). In southern California as in northern California, there is a conspicuous lack of seismic activity along many of the active faults. In particular, most sections of the San Andreas and Garlock faults in southern California appear to be seismically quiescent (Figures I-2, I-3).

Although spatial and temporal variations in earthquake activity are extremely large, the size distribution of earthquakes within a given

region follows the simple relation log N = a - bM, where N is the number of earthquakes with magnitude greater than or equal to M and a and b are empirical constants (Gutenberg and Richter, 1949). The constant b is usually close to 1. The Gutenberg-Richter magnitude-frequency relation does not, in general, apply to individual faults. This relation, with b values near 1, does appear to adequately describe the magnitude distribution of the smaller earthquakes on a single fault, which in many cases consist largely of aftershocks of the larger events. There is, however, evidence for a deviation to lower b values (relatively more large earthquakes) or perhaps even a complete breakdown of this relation at magnitudes approaching the maximum magnitude characteristic of the fault. This evidence comes from comparisons of observed seismic moment rates to those calculated from geologic data under the assumption that the Gutenberg-Richter relation with b=1 holds for each fault all the way up to its maximum magnitude (Wesnousky et al., 1983; Lahr and Stephens, 1982). Thus, on a regional scale the earthquake frequency distribution may be primarily a function of the regional distribution of fault lengths and slip rates (Wesnousky et al., 1983). The size distribution of earthquakes along a given fault is probably governed by variations in stress and frictional strength along the fault, as proposed by Nur (1978), Hanks (1979), Andrews (1980), and Von Seggern (1980).

The tectonic interpretation of seismicity data poses a number of problems. One problem is how scattered 'intrablock' seismicity is related to the long-term deformation and to cycles of strain

accumulation and release along the major bounding faults. This question is addressed in Chapter 1 through a comparison of focal mechanisms of small earthquakes in the central Transverse Ranges, California, with geologic data concerning long-term deformation and geodetic measurements of short-term deformation. Despite considerable variety in the observed mechanisms, their compression axes cluster around a north-south, horizontal axis. This is consistent with the geologic and geodetic evidence for strong north-south compression in the central Transverse Ranges. Studies of small earthquake focal mechanisms in other regions have also found that the compression or tension axis is the most stable faulting parameter, and that the inferred principal stress directions agree well with those inferred from geologic data and in situ stress measurements (Zoback and Zoback, 1980). Thus, it may be useful to think of diffuse intrablock seismicity as fracturing of small zones of weakness that are favorably oriented to the applied stress field. Focal mechanisms of small earthquakes, when integrated, may be a better indicator of the regional stress field than focal mechanisms of large earthquakes because there is likely to be a greater variety of potential slip surfaces available for the smaller earthquakes.

Another important question regarding seismicity data is under what conditions do small earthquakes occur on major, throughgoing faults, and what limits their size when they do. Various authors have proposed that small earthquakes represent the sudden failure of strong, locked portions of fault surfaces that are assumed to be very weak elsewhere, perhaps freely slipping (Kanamori, 1981; Mikumo and Miyatake, 1983).

The strong areas of the fault are called asperities. In these models, the area of fault which breaks is controlled by mechanical heterogeneities along the fault. Some predictions of these models regarding waveforms and stress drops of small earthquakes are examined in Chapters 2 and 3 using digital data from the Southern California Seismic Network. The waveform observations presented in these chapters provide some support for the concept of asperities. Chapter 4 reviews source studies of small earthquakes in the context of asperity models.

Chapter 2 of this thesis has been published in the Journal of Geophysical Research (Pechmann and Kanamori, 1982). An earlier version of Chapter 1 was accepted in 1979 for inclusion in a U.S. Geological Survey Professional Paper on the Transverse Ranges and may someday be published. The section of Chapter 1 entitled "Evidence for Temporal Changes in Focal Mechanisms" is condensed from a paper by Sauber, McNally, Pechmann, and Kanamori (1983) in the Journal of Geophysical Research.

CHAPTER 1

Tectonic Implications of Small Earthquakes in the Central Transverse Ranges, California

Introduction

The Transverse Range province of Southern California is a complex east-trending geomorphic and structural unit which interrupts the northwest-trending tectonic grain of the Pacific-North American plate boundary (Jahns, 1973; Bailey and Jahns, 1954). In this region the San Andreas fault turns sharply from its general southeast orientation and strikes east-southeasward across the Transverse Ranges before splintering into several major branches and continuing southeastward to the Gulf of California (Allen, 1968). South of the San Andreas 'big bend' is a broad zone of roughly east-trending, north-dipping thrust and reverse faults including the Santa Monica, Santa Susana, Sierra Madre, and Cucamonga frontal fault systems (Figure 1-1), along which mountain blocks of the central and western Transverse Ranges have been thrust upward and southward.

Interest in the tectonics of the central Transverse Ranges has been excited in recent years by several developments, notably: (1) The documentation of right-lateral shear strain accumulation along the locked big bend segment of the San Andreas fault (Prescott and Savage, 1976; Savage et al., 1981a, b) contemporaneous with at least partial

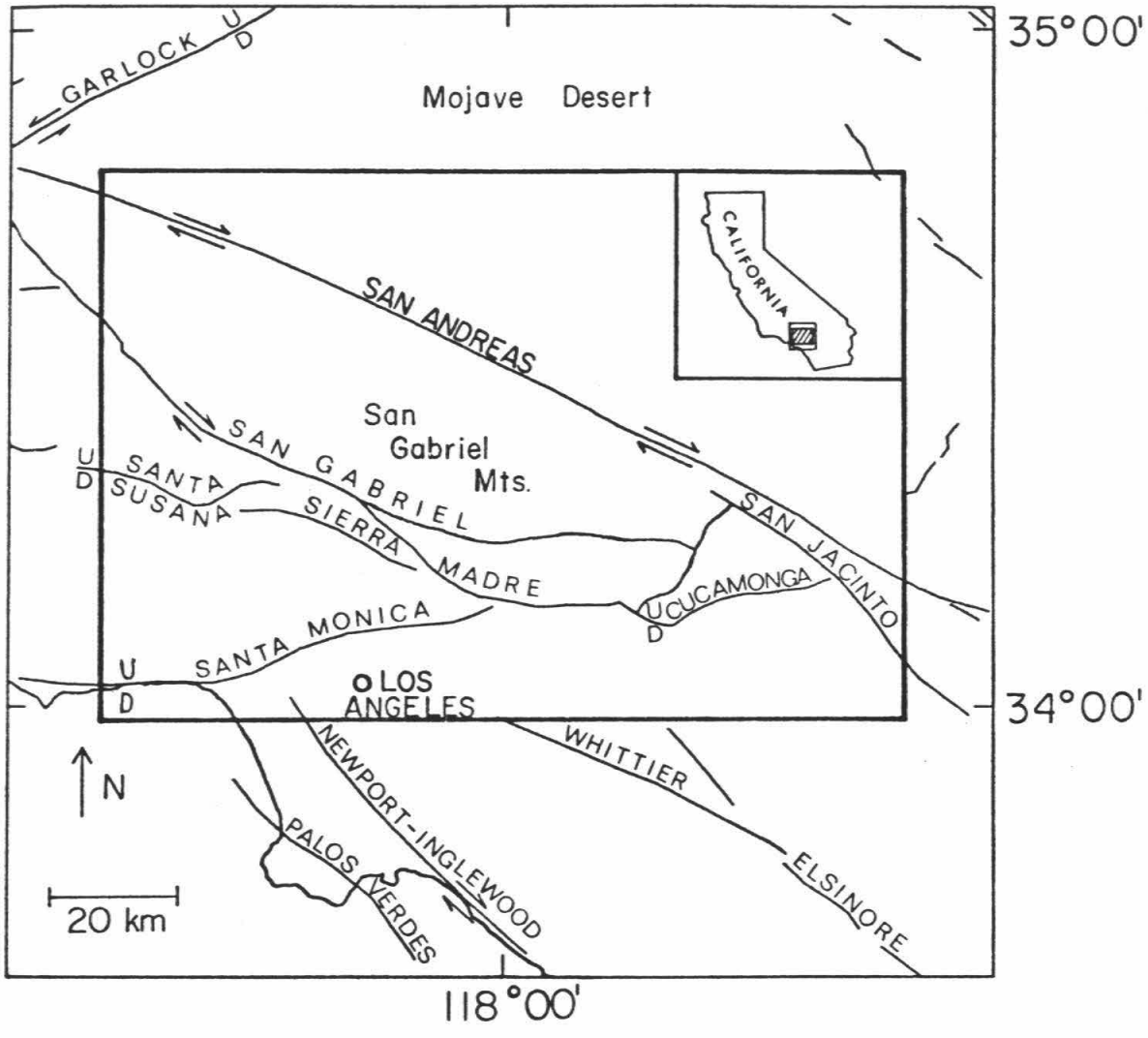

Figure 1-1. Base map showing the locations and senses of motion of major fault systems within the central Transverse Ranges, generalized from Jennings et al. (1975). Arrows show strike-slip motion. 'U' and 'D' indicate upthrown and downthrown sides of dip-slip faults.

strain release along the fault system to the northwest and southeast by creep and moderate earthquakes (Allen, 1968, 1982; Burford and Harsh, 1980; Harsh et al., 1978). (2) The occurrence of the 1971 San Fernando earthquake (local magnitude, M_L = 6.4) along the western end of the Sierra Madre fault system (Oakeshott, 1975; Murphy, 1973; U.S. Geological Survey, 1971). (3) The reported formation between 1959 and 1974 of a vertical crustal uplift throughout most of the Transverse Ranges province (Castle et al., 1976). Leveling data indicate that this uplift, the so-called Palmdale Bulge, reached a maximum of 35 cm within the boxed area shown in Figure 1-1 and then partially subsided between mid-1974 and mid-1976 (Bennett, 1977; Mark et al., 1981). However, serious questions have been raised regarding the accuracy of the leveling data which define the uplift (Jackson and Lee, 1979; Strange, 1981) and the Palmdale Bulge is currently a matter of great controversy (Kerr, 1981). (4) The occurrence from 1976 to 1977 of an earthquake swarm along the locked section of the San Andreas fault shown in Figure 1-1. This swarm was the first observed along this section of the San Andreas since cataloging of instrumental data began in 1932 (McNally et al., 1978). (5) Abrupt changes in the horizontal strain accumulation patterns in southern California which were detected in 1978 and 1979. The measured changes were particularly large on geodetic networks in the Transverse Ranges (Savage, et al., 1981a, b).

During the last few years, vastly improved data on earthquakes in Southern California have become available due to the increase in the number of stations in the California Institute of Technology/ U.S.

Geological Survey seismographic network from 39 stations in 1972 to nearly 150 stations in 1978 (Whitcomb, 1978) to over 200 stations in 1983. Studies of Southern California crustal structure using the expanded array (Kanamori and Hadley, 1975; Hadley and Kanamori, 1977; Hadley, 1978) have made possible more accurate interpretations of the earthquake data. Previous studies of earthquakes in the central Transverse Ranges have dealt primarily with the San Fernando earthquake and its aftershocks (Hadley and Kanamori, 1978; Whitcomb et al., 1973) and with microearthquake data from small temporary arrays (Cramer and Harrington, 1979; Murdock, 1979; Hadley and Combs, 1974). The purpose of this paper is to present seismicity and focal mechanism data for the entire central Transverse Ranges area and to discuss its tectonic significance in terms of the geologic evidence concerning long-term deformation and also the available geodetic evidence pertaining to short-term deformation. The first three sections present a regional study of seismicity and focal mechanisms completed in January, 1979. The following section summarizes some results of a later study by Sauber et al. (1983) which suggest that changes in the regional strain accumulation pattern which took place in late 1978-1979 triggered changes in focal mechanisms and in the level of small earthquake activity near Palmdale. These two studies suggest a model for the relationship of small earthquakes in the central Transverse Ranges to strain accumulation on the San Andreas and frontal fault systems which is outlined in the concluding section.

Seismicity, 1933-1977

Figures 1-2 and 1-3 show epicenters of all earthquakes located by the California Institute of Technology (Caltech) between 1933 and 1977 within the boxed area shown in Figure 1-1. Faults shown in Figure 1-1 are generalized from Jennings et al. (1975). Epicenters and magnitudes are taken directly from the Caltech/ U.S. Geological Survey southern California earthquake catalog (Whitcomb et al., 1978; Friedman et al., 1976; Hileman et al., 1973). Since location techniques and the density of seismographic stations have changed greatly throughout the years, these maps must be interpreted with care. Prior to 1961 epicentral determinations were done graphically and reported to the nearest minute. This explains the tendency of epicenters to line up in north-south and east-west directions in the earlier maps. The 1977 catalog is preliminary, meaning that hypocentral locations are subject to slight modification, quarry blasts have not been removed, and magnitude determinations for the smaller events are incomplete. Quarry locations are indicated by 'Q' in Figure 1-3. Earthquakes in 1977 for which magnitudes have not yet been determined are plotted as having $M_L \leq 2$ in Figure 1-3 but may lie in the range $2 < M_L \leq 3$.

Examination of Figure 1-3 shows that despite a much improved detection capability and greater location accuracy, the epicenters still do not show much tendency to cluster near the surface traces of faults. The only exceptions are along the San Jacinto fault and along a northeast-trending feature south of the Cucamonga fault previously

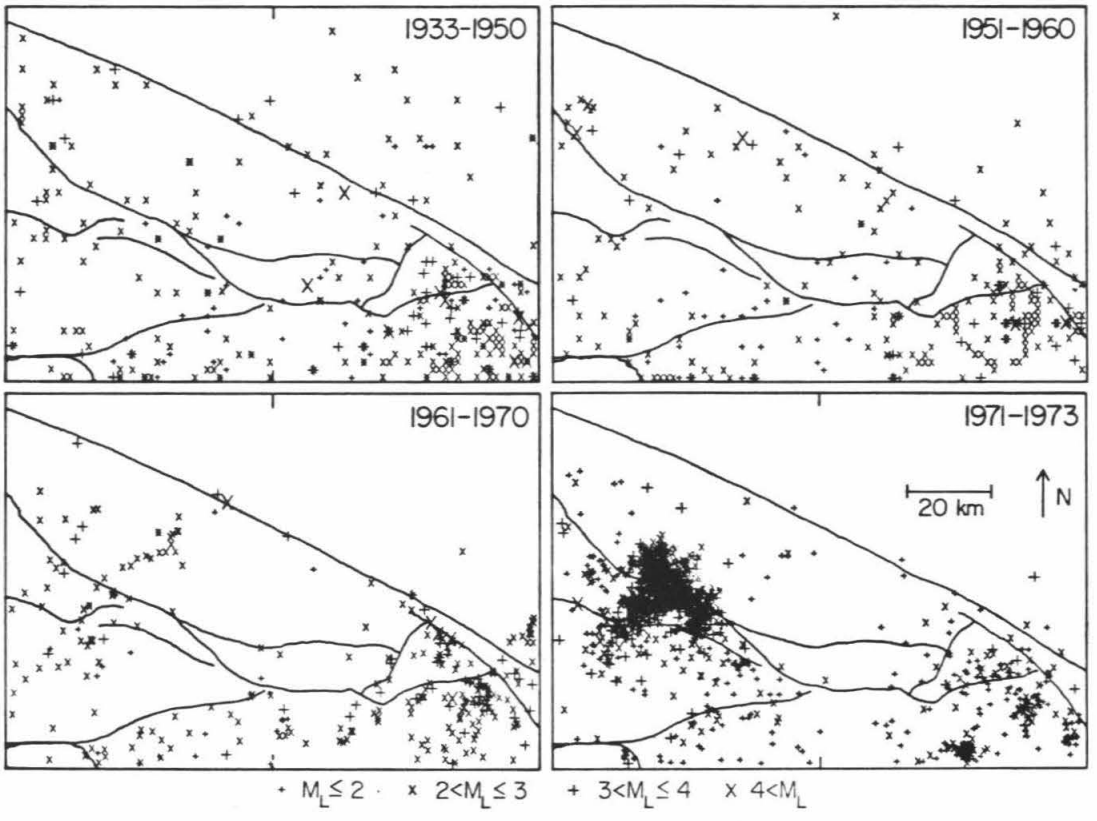

Figure 1-2. Map showing epicenters of all earthquakes located by the California Institute of Technology within the boxed area shown in Figure 1-1, for various time intervals. Different symbols indicate local magnitude (M_L) as shown.

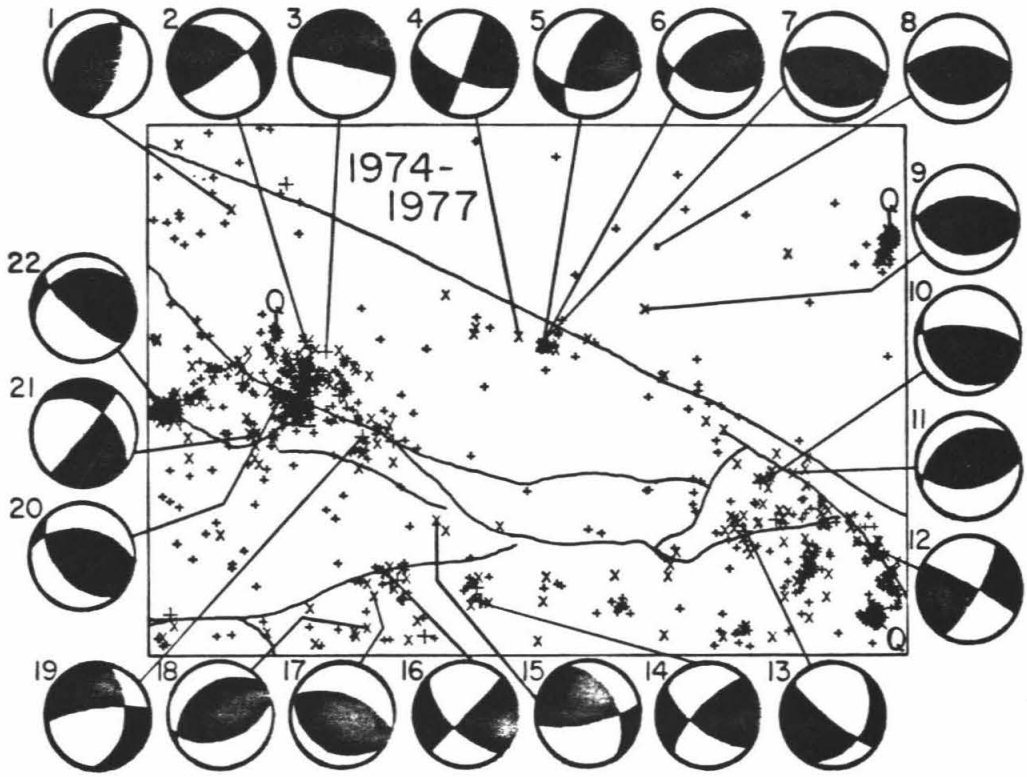

Figure 1-3. Map showing locations of focal mechanisms of Figure 1-5 and epicenters of all earthquakes located by the California Institute of Technology within the boxed area shown in Figure 1-1 for the time interval 1974-1977. Quarry locations are labelled with a 'Q'. Magnitude symbols are the same as those in Figure 1-2. Numbers next to focal mechanisms correspond to those in Figure 1-5. Shaded quadrants are compressional.

identified by Hadley and Combs (1974) on the basis of a microearthquake survey. Hadley and Combs actually found two northeast-trending clusters in this area 5 km apart, the northern one being coincident with the Fontana water barrier. Several aftershock sequences and localized swarms show up very well on the seismicity maps in Figures 1-2 and 1-3. The San Fernando aftershock zone is a prominent feature north of the Sierra Madre fault system in the western half of both the 1971-1973 and 1974-1977 maps. The 1972 Ontario swarm shows up very clearly as a dense cluster near the southeastern corner of the 1971-1973 map. The epicenters in Figure 1-3 near the western end of the surface trace of the Santa Susana fault are mostly aftershocks from a magnitude 4.6 event on April 8, 1976. This event is noteworthy because of its large number of aftershocks and its unusually great depth of 18 km. The 1976-1977 swarm just to the south of the San Andreas fault in Figure 1-3 has been studied by McNally et al. (1978). The recent increase in seismicity here and to the northwest along the San Andreas fault has been shown to be real. However, it is not clear whether the apparent recent increase in seismicity in the Mojave Desert to the northeast of the San Andreas fault (compare Figures 1-2 and 1-3) is real or merely an artifact of improved station coverage.

The scatter in the epicenters of small (M_L<6.0) shocks in Southern California and the general lack of clear spacial relationships between these shocks and recognized faults has often been noted (Richter, 1958; Allen et al., 1965). Important exceptions to the rule are the concentrations of seismicity to the southeast of the study area

associated with the Imperial, Brawley, and San Jacinto faults (Friedman et al., 1976; Whitcomb et al., 1978). All of these faults are dominantly strike-slip faults which are known to be creeping (Johnson and Hadley, 1976; Goulty et al., 1978; Keller et al., 1978). Although the San Jacinto fault and its zone of seismicity extends into the southeastern corner of the study area (Figures 1-1 and 1-3), creep has not been demonstrated along this segment of the San Jacinto but only along sections to the southeast. The general scattering of epicenters throughout most of the central Transverse Ranges is perhaps not surprising given the large number of Quaternary dip-slip faults in the area, most of which are either known or presumed to be of shallow dip (Jennings et al., 1975). Although most recent epicentral determinations are probably accurate to within 2-3 kilometers in this area, comparable accuracy in the hypocentral depth is difficult to obtain. The available data are of sufficient quality to exclude the existence of a concentration of hypocenters along a single great megathrust outcropping along the frontal fault system and dipping northward beneath the mountains. However, careful relocations using a master event technique may in the future serve to delineate and characterize a series of separate faults, as has been done for the western Transverse Ranges (Lee et al., 1979).

An interesting feature of the 1974-1977 seismicity map (Figure 1-3) is that in the mountains north of the Santa Susana-Sierra Madre-Cucamonga frontal fault systems most of the seismicity is concentrated to the west and to the east with comparatively few

epicenters located in the central part of the San Gabriel mountains between the eastern Sierra Madre and San Andreas fault zones. This same pattern is present at least as far back as 1961 when computer location of earthquakes began at Caltech (Figure 1-2). Relocation of selected earthquakes before 1961 using arrival times on file at Caltech has shown that additional work is necessary in order to extend this analysis further back in time. Available geologic evidence concerning the long-term seismicity correlates well with these observations. Crook et al. (1979) have found that evidence for late Quaternary movement is lacking in the central part of the San Gabriel frontal fault system south of this gap but is present to the east and to the west. Since geodolite measurements by Savage et al. (1978; 1981a, b) indicate that the post-Miocene north-south crustal shortening of the Transverse Ranges (Jahns, 1973) is still going on, it appears that within the central San Gabriel mountains this deformation must be at present taking place aseismically. This may mean that the deformation here is taking place at a greater depth than elsewhere.

Focal Mechanism Determinations

In the determination of local earthquake focal mechanisms from P-wave first-motion diagrams, the principal uncertainty is in calculating the takeoff angles for first arrival ray paths. These are highly dependent upon the assumed crustal structure and hypocentral depth. For this study a four-layer crustal model based on Hadley and Kanamori (1977) and Hadley (1978) was used. The model consists of a 5

km thick, 5.5 km/sec layer at the surface underlain successively by 6.1 to 6.3 km/sec upper crust, 6.6-6.8 km/sec lower crust, and a 7.8 km/sec upper mantle halfspace beginning at a depth of 33 km (inset, Figure 1-4). The interface between the low velocity upper crust and the high velocity lower crust, the Conrad discontinuity, is located at a depth of about 15 km in the central part of the study area. To the northeast in the Mojave Desert this discontinuity is much deeper, only about 5 km above the Moho, but in the southwest corner of the study area in the Santa Monica mountains, it shallows to a depth of perhaps 10 km. Although in general the Conrad discontinuity appears to dip to the northeast in the central Transverse Ranges, the details of its geometry are poorly known. This creates particular problems in locating earthquakes and determining focal mechanisms, especially since in some areas the discontinuity is located within the seismic zone which here ranges down to about 15 km. One approach to this problem is to employ a model consisting of many horizontal layers, so that the Conrad discontinuity can be smoothed out into a gradient over a depth of about 10 km. This technique was used by Hadley and Kanamori (1978). The advantage of this technique is that it reduces the sensitivity of the focal mechanism to changes in the depth of the source. In this study a different and hopefully more accurate method is used.

Events for the regional focal mechanism study were chosen more or less at random, although some attempt was made to obtain a representative geographical distribution within the study area. Twenty-two events ranging in magnitude from 2.2 to 4.6 were selected for

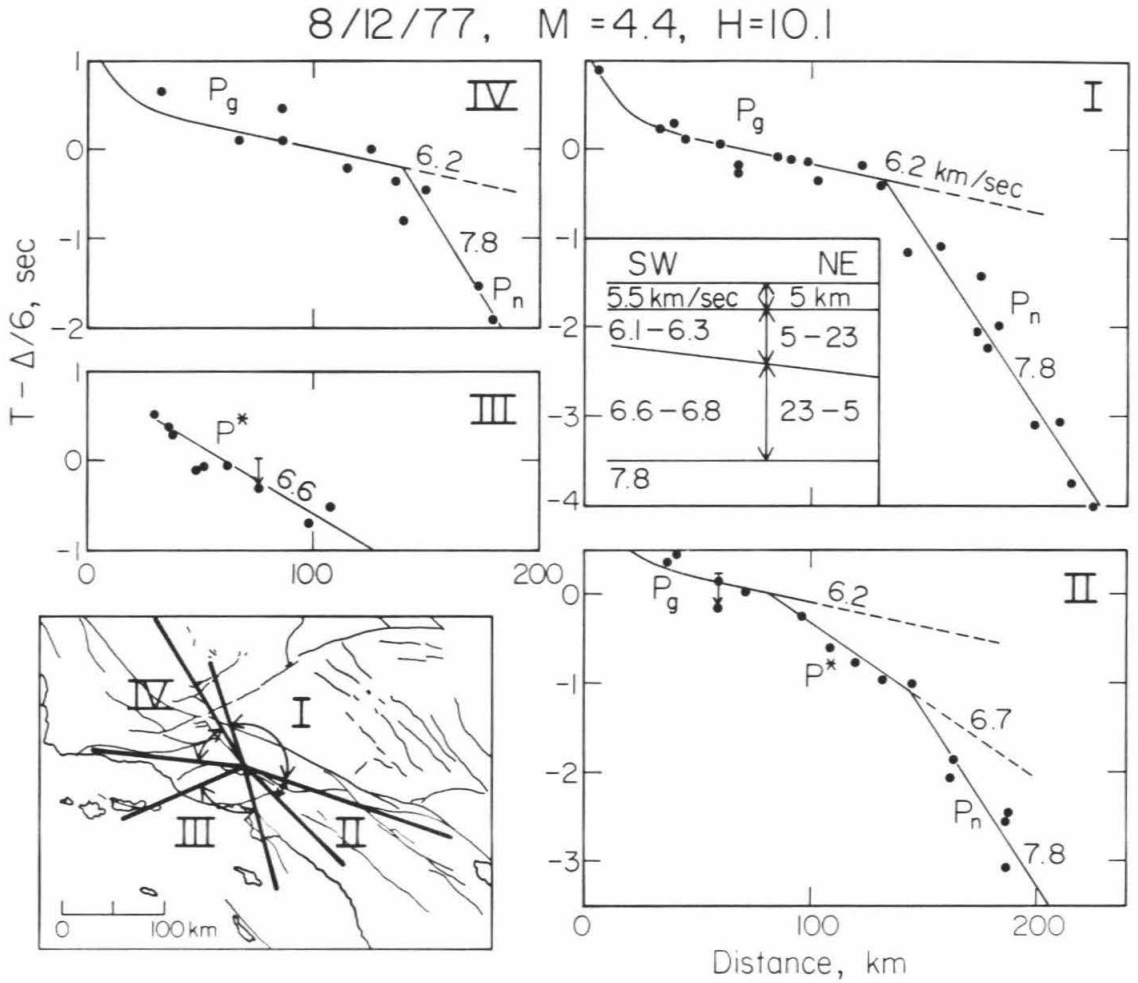

Figure 1-4. Plots of reduced travel time, T-Δ/6, versus distance, Δ, for the four azimuth ranges shown in the map at lower left. Source is a local magnitude 4.4 event at a depth (H) of 10.1 km. Vertical arrows above some points show deep sediment corrections determined by Raikes (1978). Inset shows the velocity model used to interpret the plots (Hadley and Kanamori, 1977; Hadley, 1978). Dip on the Conrad discontinuity is exaggerated.

study from the time period 1974 to 1978 (Table 1-1). To determine the focal mechanisms, arrival times and first motions were first read from 16mm/develocorder film viewed at a scale of 1 sec/cm. These data were supplemented in many cases by readings from helicorder paper records, films from temporary trailer stations, and computer-stored seismographic traces from the Caltech Earthquake Detection and Recording (CEDAR) system (Johnson, 1979). The twenty-two earthquakes were then relocated using the computer program HYP071 (Lee and Lahr, 1975) and a horizontally-layered version of the model shown in Figure 1-4. Only stations within 60 km of the epicenter were used in order to maximize the depth resolution and minimize the use of arrival times from the dipping Conrad discontinuity, placed at a depth of 15 km in the location model. The average number of stations used for each relocation was 12. Reduced travel time, $T-\Delta/6.0$, was then plotted versus distance, Δ, for various azimuth ranges. An interpretation of each plot was made in terms of the Hadley-Kanamori model, and then travel-time information was used to individually assign takeoff angles for each station. An example of this method is shown in Figure 1-4 for a local magnitude 4.4 event which occurred on August 12, 1977, at a depth of about 10 km. The reduced travel-time plots for azimuth ranges I and IV clearly show two branches. Arrivals labelled P_g are interpreted as direct waves with an apparent velocity near 6.2 km/sec beyond about Δ = 50 km. The branch labelled P_n corresponds to critically refracted waves from the Moho with an apparent velocity of about 7.8 km/sec. Refracted waves from the lower crust called P* are not observed as first arrivals in regions I

TABLE 1-1. Events Selected for Regional Focal Mechanism Study

Event No.	Date Mo/Dy/Yr	Time	M_L	Catalog Location			Revised Depth, km*
				Latitude	Longitude	Depth, km	
1	11/07/76	1421	2.6	34°40.20′	118°33.10′	8.0	7.5
2	12/08/76	0213	3.3	34°28.13′	118°24.52′	12.4	13.3
3	10/17/76	0538	3.9	34°27.16′	118°22.26′	14.9	11.2
4	12/13/76	0826	2.2	34°28.56′	118° 0.60′	5.9	8.2
5	1/01/77	0100	2.8	34°27.49′	117°57.69′	5.4	8.7
6	3/07/77	1104	3.0	34°27.68′	117°58.18′	8.0	9.1
7	9/06/77	0508	3.0	34°27.95′	117°57.93′	7.2	8.7
8	6/19/78	0741	3.0	34°37.07′	117°45.02′	6.7	7.6
9	11/03/76	1741	2.6	34°31.11′	117°46.40′	8.0	10.1
10	12/30/76	0225	2.6	34°15.64′	117°32.37′	5.0	10.2
11	5/29/76	2038	3.0	34°15.93′	117°29.86′	4.7	13.3
12	11/05/75	0237	3.0	34° 9.66′	117°22.70′	7.2	8.0
13	1/13/75	2328	3.3	34°10.64′	117°35.16′	3.6	8.0
14	12/19/74	1236	3.5	34° 4.38′	118° 4.80′	9.2	6.4
15	11/06/74	0038	3.0	34°11.71′	118° 9.96′	1.0	3.4
16	3/15/77	0801	2.2	34° 6.94′	118°15.73′	8.8	10.1
17	11/30/76	2355	2.5	34° 4.76′	118°16.93′	8.0	8.0
18	6/27/76	2211	2.9	34° 1.86′	118°17.67′	10.4	8.0
19	12/27/75	2108	3.1	34°19.37′	118°18.14′	2.1	4.7
20	8/12/77	0219	4.5	34°22.78′	118°27.52′	9.5	10.1
21	8/09/76	1054	2.8	34°19.62′	118°30.97′	8.0	0.4
22	4/08/76	1521	4.6	34°20.81′	118°39.34′	14.5	17.9

*The changes in epicentral locations averaged 2.2 km and in all cases were less than 6 km.

and IV because the Conrad discontinuity deepens too quickly in these directions. However, to the south of the source in region III, where the Conrad shallows, the reduced travel times show an apparent velocity close to 6.6 km/sec., indicating that all of the arrivals in this azimuth range are probably P*. The reduced travel-time plot for azimuth range II, which is roughly along the strike of the Conrad, shows three branches corresponding to P_g, P*, and P_n. Since the dip on the Conrad is not well known but is probably small, the takeoff angles for all three branches of the travel-time curves were calculated using the horizontally-layered location model. The resultant P-wave first-motion plot is shown in Figure 1-5 (Number 20).

Use of the technique just described eliminates much of the uncertainty in determining takeoff angles when the source depth is not well constrained. A problem still remains, however, if the event is located near a discontinuity in the velocity model, since the travel-time curves for a source located just above a discontinuity are nearly identical to those for a source located just below it, but the takeoff angles are quite different. When this problem was encountered, the mechanisms were determined for sources located on both sides of the discontinuity, and the mechanism with the fewest stations in error was chosen. Only in one instance were the two mechanisms significantly different and of equal quality, and for this event (Number 13, Figure 1-5) both solutions are shown.

Figure 1-5. Lower hemisphere P-wave fault-plane solutions for 22 events in the central Transverse Ranges. Solid circles indicate compressional first motions; open circles indicate dilatational ones. The large circles represent good-quality readings; the small circles, fair-quality readings. Slip vectors, compression axes, and tension axes are shown with triangles. The date, local magnitude M, and depth H, for each event are given. Numbers correspond to those in Figure 1-3.

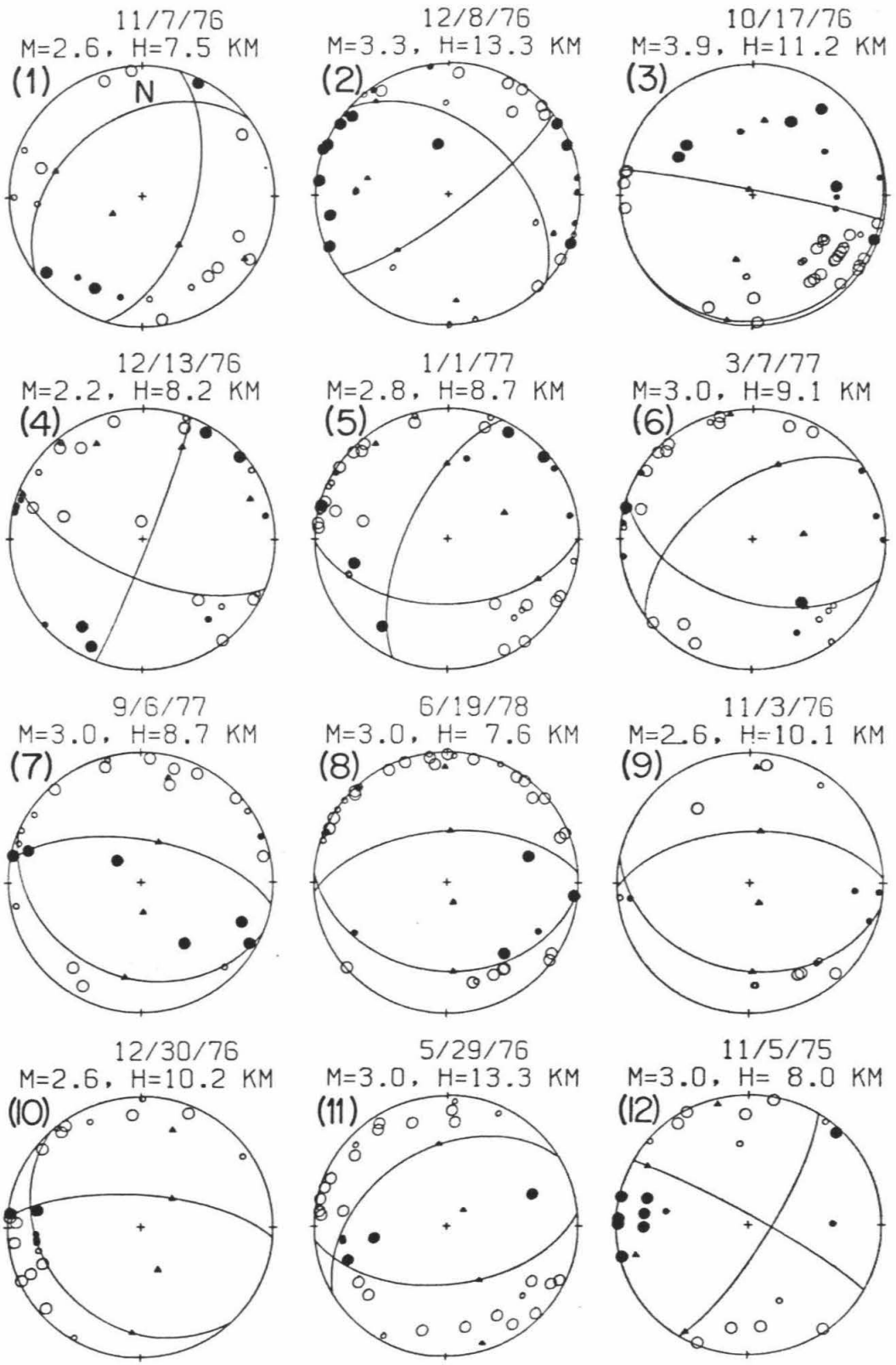
11/7/76
M=2.6, H=7.5 KM
(1)
N
12/8/76
M=3.3, H=13.3 KM
(2)
10/17/76
M=3.9, H=11.2 KM
(3)
12/13/76
M=2.2, H=8.2 KM
(4)
1/1/77
M=2.8, H=8.7 KM
(5)
3/7/77
M=3.0, H=9.1 KM
(6)
9/6/77
M=3.0, H=8.7 KM
(7)
6/19/78
M=3.0, H= 7.6 KM
(8)
11/3/76
M=2.6, H=10.1 KM
(9)
12/30/76
M=2.6, H=10.2 KM
(10)
5/29/76
M=3.0, H=13.3 KM
(11)
11/5/75
M=3.0, H= 8.0 KM
(12)

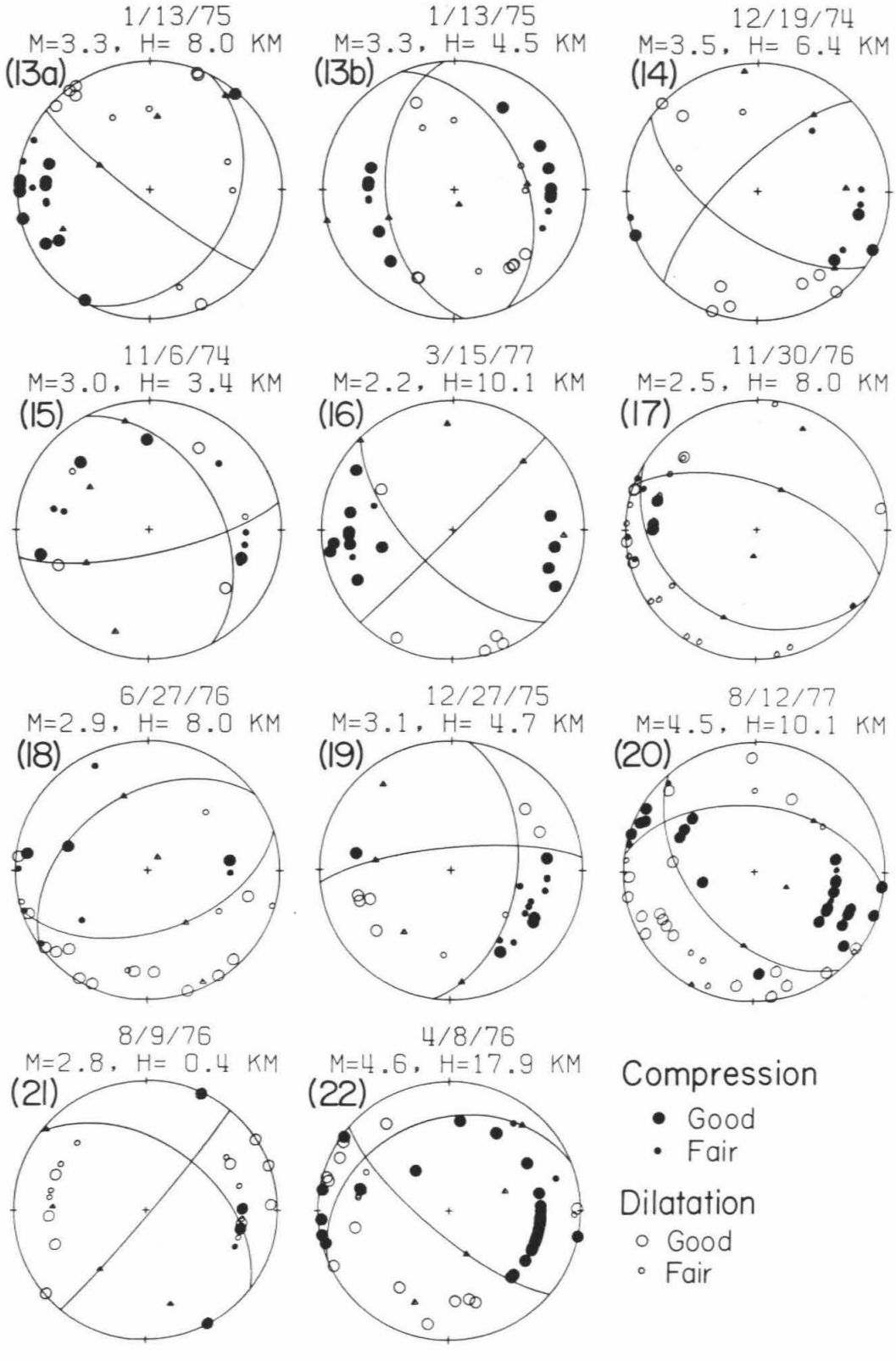
1/13/75
M=3.3, H= 8.0 KM
(13a)
1/13/75
M=3.3, H= 4.5 KM
(13b)
12/19/74
M=3.5, H= 6.4 KM
(14)
11/6/74
M=3.0, H= 3.4 KM
(15)
3/15/77
M=2.2, H=10.1 KM
(16)
11/30/76
M=2.5, H= 8.0 KM
(17)
6/27/76
M=2.9, H= 8.0 KM
(18)
12/27/75
M=3.1, H= 4.7 KM
(19)
8/12/77
M=4.5, H=10.1 KM
(20)
8/9/76
M=2.8, H= 0.4 KM
(21)
4/8/76
M=4.6, H=17.9 KM
(22)
Compression
Good
Fair
Dilatation
Good
Fair

Results of Regional Focal Mechanism Study

Figure 1-5 shows the P-wave first-motion plots for the events studied. The nodal planes were determined with the aid of the computer program FOCPLT developed by Whitcomb and Garmany (Whitcomb, 1973). This program tests a grid of trial mechanisms spaced at approximately 5 degree intervals on the focal sphere and then chooses a mechanism which minimizes the number of first motion readings in error. Less reliable readings are given half the weight of other readings, and a linear function is used to downweight stations within 3 degrees of a nodal plane. Most of the focal mechamisms shown in Figure 1-5 are well constrained. The numbers are keyed to Figure 1-3, which shows the location of each mechanism.

Examination of Figure 1-3 shows that there is little systematic variation in mechanism from place to place within the study area. Most of the solutions show strike-slip faulting, reverse faulting, or a combination of strike-slip and reverse faulting. In general, the fault-plane orientations and senses of motion do not agree very well with those of the major faults shown. Along the San Jacinto fault, mechanism No. 12 is consistent with geologic evidence for right-lateral strike-slip motion on a northwest-trending fault. However, 20 km to the northwest along the same fault zone, thrusting is observed. Mechanisms 4, 5, 6, and 7 are especially interesting because master event relocations for these events by McNally et al. (1978), show that they all cluster within a small volume 3 km in maximum dimension, centered 2 km southwest of the mapped surface trace of the San Andreas fault at a

depth of about 8 km. Although No. 4 is consistent with the long-term sense of motion on the San Andreas fault, the others are not and, furthermore, show systematic changes in mechanism with time. This swarm may be associated with the San Andreas fault or with one of several subparallel faults that splay southward from the main fault at this point. Focal mechanisms for events 20, 3, and 22 agree well with those determined independently by Hadley and Kanamori (1978). The latter two are consistent with motion on either nearly vertical or nearly horizontal planes. Hadley and Kanamori argue on the basis of these mechanisms and other evidence that regional horizontal decollements may exist within the central Transverse Ranges. If the horizontal plane in mechanisms 3 and 22 is chosen as the fault plane, then movement of the upper block is towards the south or southwest.

Although the fault-plane solutions in Figure 1-5 show considerable diversity, the compression axes for most of them are oriented nearly north-south and horizontal. Other investigators have obtained similar results in the central Transverse Ranges (Whitcomb et al., 1973; Cramer and Harrington, 1979). In the western Transverse Ranges the compression axis is still the most stable parameter, but the preferred orientation is closer to northeast-southwest horizontal (Yerkes and Lee, 1979; Stierman and Ellsworth, 1976). To produce a combined plot of the compression axes which reflected the degree of constraint of the mechanisms, I used the grid of scores calculated by FOCPLT for each event. Positions of the compression axes corresponding to best-fit solutions with the minimum number of stations in error were assigned a

weight of 3. Positions which allowed less than one additional good quality reading or two additional fair quality readings to be in error were assigned a weight of 2. Positions with the number of stations in error beyond the minimum lying in the range 1-2 good or 2-4 fair were given a weight of 1. Scores worse than this were given zero weight. The weights for all the events were added up at each focal sphere grid point and the results contoured to give the plot shown in Figure 6. A similar diagram for the tension axes is also shown.

Figure 1-6 clearly demonstrates that focal mechanisms in the central Transverse Ranges are characterized by a horizontal north-south compression axis and a near vertical tension axis. The dominant type of faulting is, therefore, reverse faulting on east-striking planes with dip near 45^{o}. Even though compression and tension axes for individual earthquakes do not necessarily reflect the actual tectonic stress field (McKenzie, 1969), the well-defined maxima in Figure 1-6 suggest that these parameters have physical significance in a statistical sense. The north-south compression suggested by the fault plane solutions is consistent with the NNW orientations for maximum horizontal compressive stress measured in boreholes in this region (Zoback et al., 1980; Flaccus et al., 1980). There is, in addition, abundant geologic evidence to suggest strong north-south compression in the Transverse Ranges province during post-Miocene times. This north-south compression has resulted in folding along east-west axes, thrust and reverse faulting with some components of strike-slip, and major uplift of several crustal blocks (Jahns, 1973).

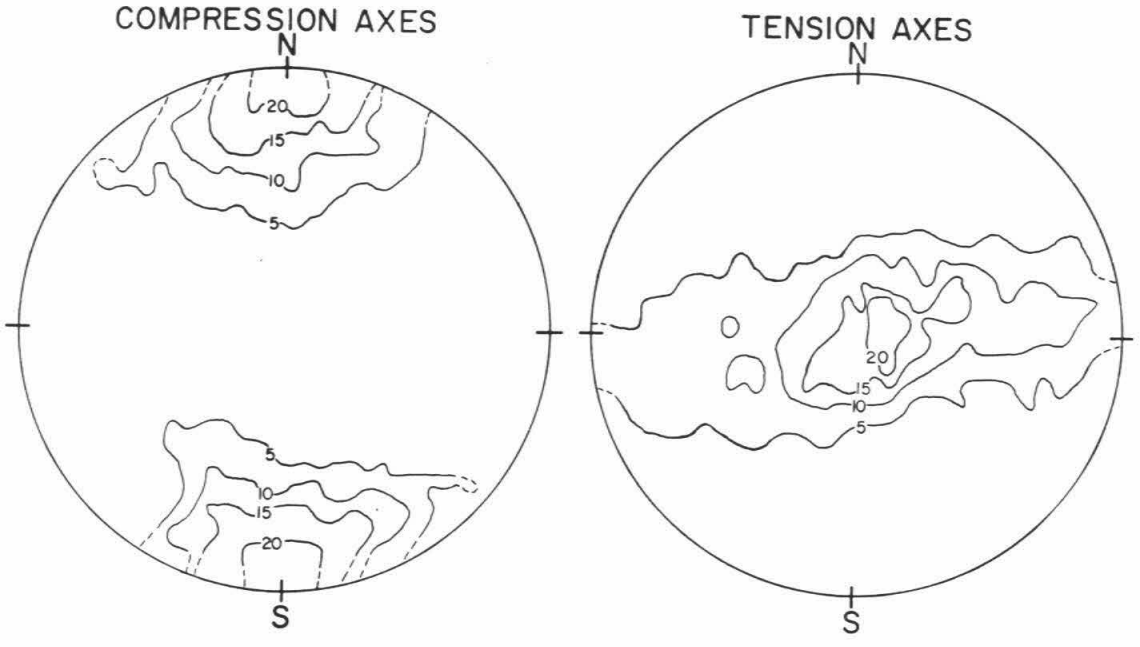

Figure 1-6. Contour maps showing the orientation of compression and tension axes on the focal sphere, taking into account variation of quality of mechanisms in Figure 1-5. See text for explanation.

A more direct conclusion which can be drawn from Figure 1-6 is that the average deformation resulting from small earthquakes in this region is north-south crustal shortening and vertical extension, at least for the time period 1974 to 1978. Since this is permanent deformation, it constitutes a form of elastic strain relief. Geodolite measurements of horizontal strain accumulation by Savage et al. (1978) in the interval 1972 to 1978 indicate a remarkably consistent uniaxial north-south contraction of about 0.2-0.3 parts per million per year (ppm/yr) throughout Southern California. This strain appeared to accumulate uniformly with time. The amount of north-south contraction attributable to faulting during small earthquakes is therefore relevant to the rate of stress accumulation across both the San Andreas and frontal fault systems.

Kostrov (1974) derives an expression to describe how movements in separate earthquakes along numerous randomly located fractures can be summed in a quasi-plastic deformation process. The expression is:

$$\dot{\varepsilon}_{ij} = \frac{1}{2\mu\Delta v\Delta t} \sum_{\kappa} M_{oij}^{(\kappa)}$$

where $\dot{\varepsilon}_{ij}$ is the mean tensor of the rate of deformation due to the seismic flow of rock masses, Δv and Δt are the volume and time interval, respectively, over which the $M_{oij}^{(\kappa)}$ are summed, μ is the rigidity, and $M_{oij}^{(\kappa)}$ is the ij'th component of the moment tensor of the κ'th earthquake. If M_o is the moment,

$$M_{oij} = M_o(b_j n_i + b_i n_j)$$

where $\underline{b}$ is a unit vector in the displacement direction and $\underline{n}$ is a unit

vector perpendicular to the fault plane. To estimate the mean tensor of the rate of seismic deformation in the central Transverse Ranges, we assume that the average $\underline{b}$ and $\underline{n}$ vectors are those corresponding to the average mechanism indicated by Figure 1-6. In a coordinate system with the X_1-axis directed eastward, the X_2-axis northward, and the X_3-axis upward, the expression for $\dot{\varepsilon}_{ij}$ reduces to

$$\dot{\varepsilon}_{33} = -\dot{\varepsilon}_{22} = \frac{1}{2\mu\Delta v\Delta t} \sum_{\kappa} M_o^{(\kappa)}$$

with all other components zero. Since the mechanisms were determined for earthquakes during the time period 1974-1978, but post-1976 magnitudes are incomplete, we calculate $\dot{\varepsilon}_{33}$ for the three-year period 1974-1976. Define n(M) to be the number of events with local magnitude greater than or equal to M during this period within the boxed area of Figure 1-1. Since all earthquakes which occurred during this time were less than magnitude 5.0, and earthquakes of magnitude less than 0.0 have negligibly small moments, we can write

$$\dot{\varepsilon}_{33} \simeq \frac{-1}{6\mu\Delta v} \int_0^{5.0} M_o(M) \frac{dn(M)}{dM} \, dM$$

where $M_o(M)$ is an empirical moment-magnitude relationship. From Wyss and Brune (1968) and Thatcher and Hanks (1973) $M_o(M)$ is given by

$$\log M_o = 1.5M + 16.0$$

The function n(M) was found to be given to a good approximation by

$$\log n = 4.5 - 1.0M$$

Since most earthquakes in the study area occur at depths less than 15 km, we set Δv equal to the (area of the box in Figure 1-1) X (15 km).

This gives $\Delta v = 1.7 \times 10^{20}$ cm^3. Assumimg $\mu = 2 \times 10^{11}$ dynes/cm^2 and substituting into the above expression, the result is $\dot{\varepsilon}_{33} = -\dot{\varepsilon}_{22} \simeq 1 \times 10^{-9}$ /year.

This number is two orders of magnitude smaller than the rate of north-south contraction determined geodetically at the surface for the same time period. We conclude that seismic faulting during 1974-1976 within the study area can account for only a negligibly small amount of the measured north-south contraction. Hence, most of the contraction must represent either elastic strain accumulation or aseismic deformation.

Evidence for Temporal Changes in Focal Mechanisms

Shortly after the regional focal mechanism and seismicity study presented above was completed in January 1979, changes were detected in the horizontal strain accumulation patterns in southern California through two different geodetic monitoring techniques: interferometry measurements using extraterrestrial radio sources (P. F. MacDoran, unpublished data from the Aries Project, 1980) and ground-based trilateration with a laser-ranging device (Savage et al., 1981a, b). The horizontal strain accumulation across all three of the U.S. Geological Survey trilateration networks which lie within or partially within the central Transverse Ranges - the Tehachapi, Palmdale, and Cajon nets (Figure 1-7) - was a uniaxial north-south contraction of 0.2-0.3 ppm/yr from when measurements began in 1971-1974 through 1978 (Savage et al., 1978). Between late 1978 and 1979, an episode of NS and

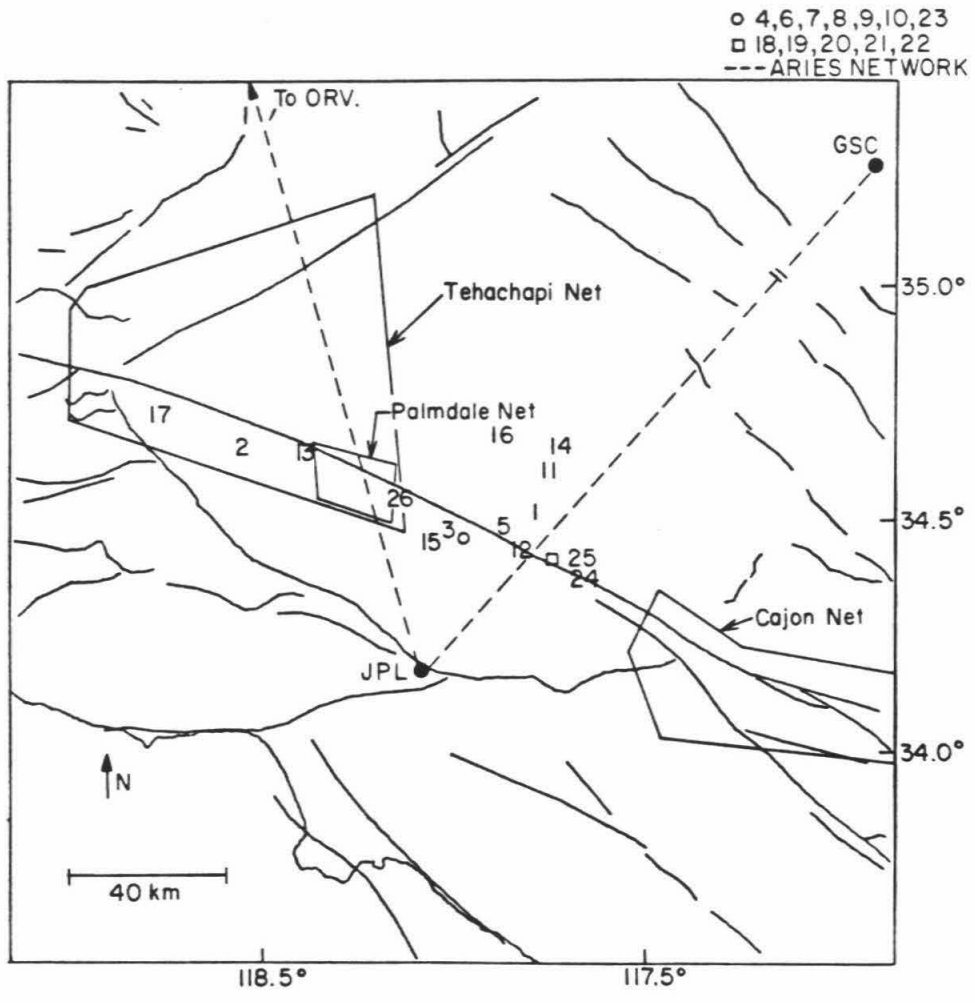

Figure 1-7. Locations of events for which a focal mechanism was determined by Sauber et al. (1983). Event numbers are chronological, and do not correspond to event numbers in Figures 1-3 and 1-5 or Table 1-1. The areas covered by the U. S. Geological Survey Tehachapi, Palmdale, and Cajon trilateration networks are shown along with the ARIES baselines. JPL is the Caltech Jet Propulsion Laboratory, GSC is the Goldstone tracking station, and ORV is the Owens Valley Radio Observatory.

EW extension was observed on the Tehachapi and Palmdale networks. The total dilatation observed amounted to about 1 part per million on the Tehachapi net and about 2 parts per million on the Palmdale net (Savage et al., 1981a, b). No corresponding dilatation was detected within the Cajon network. The measured rate of shear strain accumulation has been fairly constant on all three networks.

The remarkable agreement between the principal strain directions determined from trilateration measurements at the surface and the principal axes of the deformation tensor inferred from small earthquake mechanisms during the period 1974-1978 (Figure 1-6) suggests that small earthquake mechanisms may accurately reflect the regional strain field even though their contribution to the regional deformation is quite minor. A question therefore arises as to whether or not the 1978-1979 strain anomalies were accompanied by changes in the dominant faulting mechanism. In order to search for such changes, a systematic study of focal mechanisms of earthquakes during 1976-1980 in the big bend region of the San Andreas fault was undertaken by several workers including the author (Sauber et al., 1983). The results of this study are reviewed briefly below.

P-wave first motion studies were made for 26 events which occurred during the time period November 1976 through December 1980 within a 45 x 140 km region centered along the San Andreas fault in the vicinity of the Palmdale trilateration network (Figure 1-7). Focal mechanisms could be determined for all but one of the 15 events of $M_L \geq 2.5$ in this region during this time period. Focal mechanisms were determined for events of

$2.0 \leq_L < 2.5$ either from the areas of highest seismic activity (circle and square, Figure 1-7) or from other areas for better temporal coverage around the time when rapid crustal dilatation was reported. Seven of the 26 mechanisms are from the regional study discussed above. The rest of the mechanisms were determined using a similar procedure, except that the bulk of the first motion readings are from computer-stored seismographic traces from CEDAR rather than from develocorder film.

To facilitate comparison of the earthquake data to horizontal strain data, strain data from the Palmdale network (Savage et al., 1981b) are superimposed on a time/distance plot of the seismicity in Figure 1-8, together with mechanisms for 13 of the 14 events of $M_L \geq 2.5$ and as many additional mechanisms as could fit on the graph. The Palmdale strain data are used for this comparison because the Palmdale network is located closest to the earthquakes for which mechanisms were done (Figure 1-7) and more frequent measurements were taken there than on the other networks. Figure 1-8 suggests that the strain anomaly of late 1978-1979 was accompanied by changes in focal mechanisms and in the level of microearthquake activity in the big bend region of the San Andreas fault. Small earthquake activity increased in this entire region in November 1976 concurrent with the initiation of the earthquake swarm at Juniper Hills (JNH in Figure 1-8, circle in Figure 1-7; see McNally et al., 1978). The time/distance plot in Figure 1-8 and a more detailed plot in Sauber et al. (1973) show an abrupt decrease in this activity near the beginning of 1979 to the northwest and southeast of Juniper Hills. Most focal mechanisms in Figure 1-8, like those in

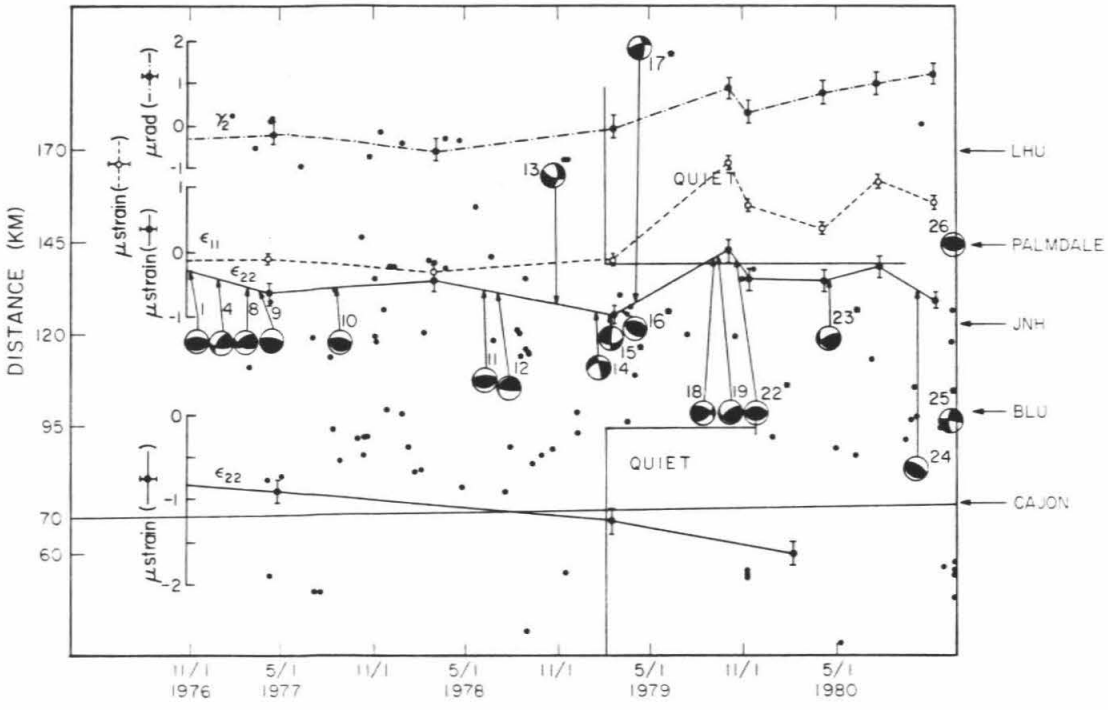

Figure 1-8. Time/distance plot of seismicity with strain data and focal mechanisms superimposed. The top three graphs are strain data from the Palmdale network. The error bars represent one standard deviation on either side of the plotted point. The strain components shown are: ε_{11}, east-west strain, compression is downward; ε_{22}, north-south strain, compression is downward; $\gamma_2 = \varepsilon_{11} - \varepsilon_{22}$, engineering shear strain (twice the tensor shear strain), right-lateral strain accumulation on a northwest-striking plane is positive. The bottom graph is north-south strain from the Cajon network. The positions of the focal mechanisms correspond (as closely as possible) to their temporal and spatial location on the graph. Their occurrence in time is more closely indicated by the arrows pointing to the north-south strain data. An asterisk appears next to the focal mechanisms for events of $2.0 \leq M_L < 2.5$. Figure is taken from Sauber et al. (1983).

Figure 1-3, show reverse faulting, strike-slip faulting, or a combination of the two and are consistent with north-south compression. Reverse faulting on northeast- to southeast-striking planes appears to be the most common faulting mechanism, as was found for the regional study (Figures 1-5 and 1-6). However, there appears to be an unusually large number of strike-slip events around the time of the crustal dilatation episode.

The temporal changes in focal mechanism are best seen by examining the orientations of the P (compression) and T (tension) axes (Figure 1-9). The angles ϕ_P and ϕ_T between the vertical and the P and T axes, respectively, are plotted versus time for all 26 events. Although there is some fluctuation in ϕ_P, the P axis is generally horizontal to subhorizontal with no systematic changes with time. ϕ_T, however, ranges from near vertical to near horizontal. There are two time periods where ϕ_T is generally greater than 45 degrees, indicating that the mechanisms are closer to strike slip than to thrust. The first period (December 1976 to February 1977) corresponds to the beginning of the Juniper Hills swarm. No strain anomaly was reported during this period, although measurements were only being taken about once a year. The second period (November 1978 to April 1979) approximately coincides in time with the change in the trend of the strain data from uniaxial north-south compression to dilatation.

Although Figures 1-8 and 1-9 suggest that a change in focal mechanism accompanied the strain changes, this correlation must be considered tentative because of the limitations of the data. First,

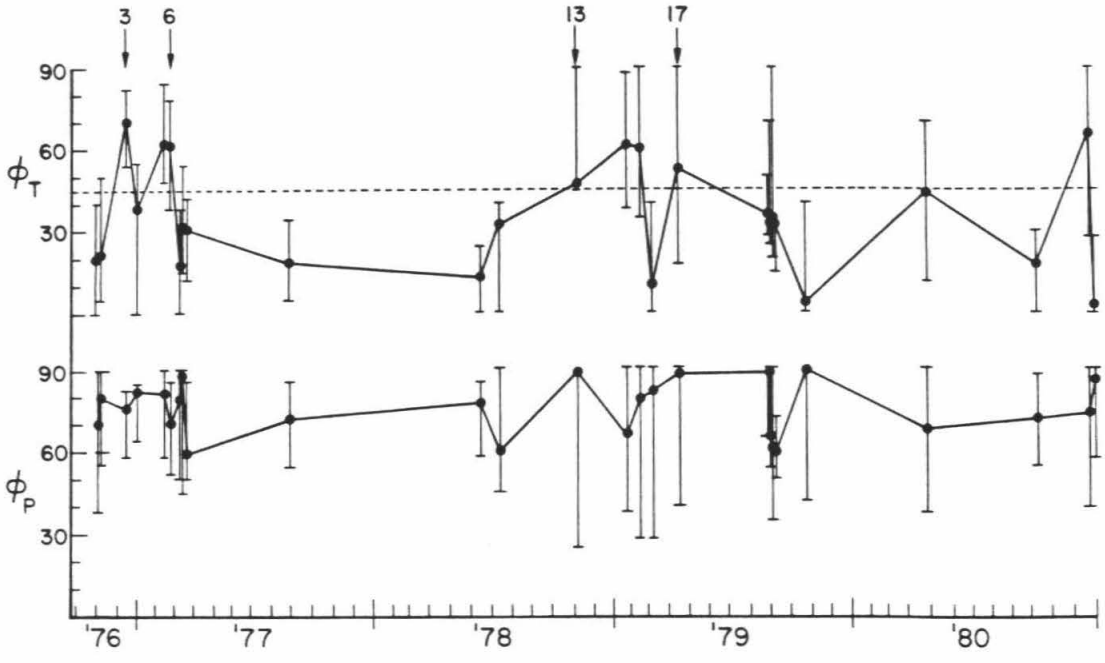

Figure 1-9. The angles Φ_P and Φ_T between the vertical and the P and T axes respectively, plotted against time for the 26 events for which locations are shown in Figure 1-7. The error bars correspond to the range of possible angles for the P and T axes with up to one 'good' or two 'fair' additional readings in error. Figure is from Sauber et al. (1983).

many of the focal mechanisms for the smaller events are not well constrained, as illustrated by the error bars in Figure 1-9. Second, the strain data are probably aliased. Prior to 1979, the strain measurements were taken only on a yearly basis on the Palmdale net. Later measurements showed significant strain changes between surveys taken only a few months apart. Biweekly observations of a nearby network with a two-color laser Geodimeter during 1980-1982 revealed short-term fluctuations in dilatation at rates as high as about 8 ppm/year for periods of a month (Langbein et al., 1982). A further problem is that strain changes between individual measurements on the Palmdale network from 1977 to February 1979 are not statistically significant, although the general trend of uniaxial north-south contraction from 1971 to 1978 does appear significant (Savage et al., 1981b). For these reasons, it is not possible to define the time of onset of relative dilatation in late 1978-1979 to within better than approximately ±6 months, or to know if the subsequent period of compression began before or after the October 1979 survey (Figure 1-8). Thus, although the second group of strike-slip earthquakes (November 1978 to April 1979) appears to be roughly concurrent with the dilatation, a temporal coincidence cannot be conclusively proven or disproven with the data at hand.

In the area around the big bend of the San Andreas fault, the most compressive principal stress is roughly north-south. Anderson's (1951) theory of faulting predicts strike-slip failure for this region if the intermediate principal stress is vertical and the least principal stress

is east-west. Thrust events can occur if the least principal stress is vertical and the intermediate principal stress is east-west. Therefore, a change in mechanism from thrust to strike slip suggests that the least principal stress has changed from vertical to horizontal east-west. Although Anderson's theory does not take into account preexisting zones of weakness, the variations in mechanism suggest that a wide variety of potential fault surfaces exists regionally and that small earthquakes occur on those most favorably oriented to the current stress field.

The change in mechanism from thrust (events 11 and 12, Figures 1-8 and 1-9) to predominantly strike slip (events 13, 14, 15, and 17) during the period mid-1978 to mid-1979 is at least qualitatively consistent with the measured horizontal strain changes and may reflect a change in the tectonic stress field. The east-west extension which began in 1978-1979 could cause a rotation of the least principal stress axis from near vertical to near horizontal, depending on the preexisting stress and the magnitude and sign of any changes in the vertical stress component. Although north-south extension was also observed at this time, it was smaller in magnitude than the north-south compressive strain accumulated over the previous 7 years, and hence the orientation of the greatest compressive principal stress probably remained approximately north-south.

A decrease in the level of seismic activity and a change in the predominant type of mechanism to more strike-slip motion around the time when there is a change from relative compression to dilatation suggests that regional strain changes might influence small earthquake faulting.

The maximum linear strain change observed on the Palmdale network is 1.5 μ strain. If we assume a linear relation between stress and strain and take the elastic modulus to be 3.3×10^{11} dynes/cm^2, this strain change roughly corresponds to a stress change of 0.5 bar. Changes in the level of microearthquake activity and a change in the predominant type of fault mechanism might therefore occur as a result of small changes in stress. However, the data are incomplete, and further monitoring is necessary to substantiate this conclusion.

Conclusions

The overall seismicity within the central Transverse Ranges can best be described as diffuse. Focal mechanisms for recent small earthquakes in this region similarly indicate that most of the seismicity is not directly related to the major Quaternary faults (Figure 1-3). The dominant mechanism of faulting at present appears to be reverse faulting on east-striking planes. Less commonly, strike-slip faulting on generally northwest- or northeast-striking planes is observed. Most mechanisms represent a combination of these two principal fault types, which correspond to the major categories of active fault systems found in this region.

Horizontal strain accumulation across geodetic networks in the central Transverse Ranges appears to consist of 0.2-0.3 ppm/year of approximately north-south compression which is occasionally interrupted by episodes of both north-south and east-west extension. The average deformation resulting from small earthquakes in this region is very

similar to the pattern of strain accumulation inferred from surface measurements: north-south crustal shortening and vertical extension with a lesser amount of east-west extension. However, calculations show that the small earthquakes ($M_L \leq 5$) are relieving only a negligible amount of the accumulating strain. There is some evidence to suggest that strike-slip earthquakes are more common than reverse-slip earthquakes during periods of dilatation. If this is true, faulting in small earthquakes may be sensitive to small changes in the applied stress.

The above observations suggest that a reasonable physical model for the deformation in between large earthquakes in this region is quasi-homogeneous north-south crustal shortening accompanied by vertical and east-west extension which involves elastic strain accumulation and brittle seismic fracturing near the surface together with viscous or viscoelastic flow at depth. Most of the small earthquakes appear to be part of this quasi-homogeneous deformation process and are not associated with large-scale block movements along major faults. Detailed studies may in some cases serve to identify small earthquakes with small-scale block movements. However, it seems likely that a wide variety of pre-existing zones of weakness exists throughout the region and that slip occurs on those most favorably oriented to the local stress field.

The central Transverse Ranges stress field inferred from fault-plane solutions and near-surface measurements appears to be dominated by north-south compression with the least principle stress axis near vertical. However, the origin of this stress field is not

well understood. Simple dislocation models of the San Andreas fault system predict north-northwest to north-northeast compression in the central Transverse Ranges, with an equal amount of horizontally directed tension perpendicular to the compression (Prescott and Savage, 1976; Rodgers and Chinnery, 1973). Bird and Piper (1980) have developed a plane-stress finite-element nonlinear tectonic flow model for southern California which includes a weakened zone along the San Andreas fault. This model comes closer to reproducing the observed stress field, but fails in other respects. Even more puzzling than the origin of the stress field is the cause of the fluctuations in the isotropic strain which occur despite the nearly uniform shear strain accumulation. Inasmuch as earthquakes are the only source of information about stress conditions deep within the earth, their continued study should prove useful in investigating the above problems.

CHAPTER 2

Waveforms and Spectra of Preshocks and Aftershocks of the 1979 Imperial Valley, California, Earthquake: Evidence for Fault Heterogeneity?

Introduction

Seismological and geological observations suggest that the mechanical properties of a fault zone are not homogeneous. Inspection of active and inactive fault zones in outcrops and in tunnels has shown them to be very heterogeneous in geometry, pore fluid pressure, and fault zone material (Wu, 1980). Surface rupture accompanying large earthquakes is usually complex, with irregular variations in displacement along the fault (Das and Aki, 1977; Aki, 1979). Seismic body waves radiated by large events are also complex and are usually interpreted using multiple event source models (Imamura, 1937, p. 267; Wyss and Brune, 1967; Rial, 1978; Kanamori and Stewart, 1978). Detailed modeling of short-period waveforms suggests that much of the higher-frequency energy comes from small, high stress drop areas on the fault plane (Cipar, 1981; Ebel, 1981; Wallace et al., 1981). The highly randomized nature of strong motion accelerograms implies large variations in effective stress during fault rupture (Housner, 1955; Nur, 1978).

Those parts of a fault with higher than average strength, commonly called asperities, may play an important role in the processes leading

up to large-scale failure. Jones and Molnar (1979) proposed that foreshocks represented accelerating failure of asperities due to concentration of stress on the unbroken asperities. Kanamori (1981) and Mikumo and Miyatake (1983) were able to explain with simple asperity models many of the longer-term spatio-temporal seismicity patterns which commonly precede major earthquakes. These include precursory swarms, quiescence, doughnut patterns, and foreshocks. Although the success of simple asperity models in explaining observed seismicity patterns is encouraging, the patterns themselves are too varied to be used reliably for earthquake prediction or to provide a good test of the models. Thus, it is desirable to examine other consequences of the models.

The key elements of asperity models that relate small earthquakes to large-scale seismic strain accumulation and release, such as those proposed by Kanamori (1981) and Mikumo and Miyatake (1983), are (1) fault surfaces are held together by a number of strong points or asperities, (2) weaker asperities fail during small earthquakes as tectonic stress increases, thereby transferring more stress to the remaining asperities, and (3) the fault becomes unstable when most, but not necessarily all, of the asperities have broken (Das and Aki, 1977; Brune, 1979). These assumptions lead to two predictions about foreshocks: (1) On the average, stress drops of foreshocks should be higher than stress drops of previous events from the area, assuming that stress drop is proportional to tectonic stress, and (2) the foreshocks should be concentrated along strong asperities and hence should occur as groups of events with very similar locations and focal mechanisms and

thus very similar waveforms. The extent to which this will occur depends on the nature of the asperities. In this paper, we will use the term asperity model to refer to a specific family of models in which concentration of stress on the stronger parts of the fault is an important factor controlling the locations and source parameters of small earthquakes.

Efforts to test the first of the predictions outlined above have produced mixed results (Reyners, 1981). This may be due to problems with the data rather than with the model. In the numerical simulations of Kanamori (1981) a ratio of 4 of the stress drop of foreshocks to other events is enough to produce the observed seismicity patterns. Since frequency content depends on many other factors such as rupture velocity and direction, near-source velocity structure, and focal mechanism, it may be difficult to detect temporal changes in stress drop of this magnitude, especially since data from only one or two stations are usually available. Furthermore, changes in anelastic attenuation near the fault caused by opening or closing of cracks or movement of pore fluids may complicate the situation.

Relatively few studies have been made of waveforms of foreshocks. Ishida and Kanamori (1978) observed that seismograms of five events that occurred in the epicentral region of the 1971 San Fernando earthquake during the 2 years before this earthquake were remarkably similar. Frankel (1982a) found that six out of seven preshocks to a magnitude 4.8 earthquake in the Virgin Islands occurred as pairs of events with very similar waveforms. Waveform similarity, however, does not appear to be

unique to foreshocks, and not all foreshocks exhibit waveform similarity. Hamaguchi and Hasegawa (1975) noted that many of the aftershocks of the 1968 Tokachi-Oki earthquake had similar waveforms and concluded that these similar events occurred at approximately the same location under the same mechanical conditions. Groups of events with similar waveforms that are not closely associated in time with major earthquakes have been reported by Stauder and Ryall (1967) in central Nevada and by Geller and Mueller (1980) and Spieth and Geller (1981) along the San Andreas fault in central California. Unpublished data collected by Kanamori show that waveforms of small earthquakes from the southeast portion of the Anza gap on the San Jacinto fault in California (Thatcher et al., 1975) have been nearly the same from 1933 to the present. Waveforms of foreshocks to the 1952 Kern County earthquake, in contrast to the San Fernando foreshocks, differed significantly from event to event (Ishida and Kanamori, 1980). The seismograms for two foreshocks to the 1966 Parkfield earthquake shown in Figure 2 of Bakun and McEvilly (1979) do not look very much alike, nor do the two foreshocks to the 1975 Oroville earthquake shown in Figure 5 of the same paper. Tsujiura (1979a) reported that seven swarms in the Kanto district of Japan were characterized by similarity of waveforms but that the waveforms of foreshocks to the 1978 Izu-Oshima earthquake showed substantial variation. The Izu-Oshima earthquake, however, had a very complicated rupture zone, and there is a strong possibility that many of the foreshocks were not associated with the main fault (Tsumura et al., 1978). Furthermore, Tsujiura (1979b) notes that during one of the

stronger swarms studied, the percentage of events in groups with similar waveforms decreased after the largest event (M 5.5) occurred. This suggests that even in hindsight an a priori distinction between preshocks, swarms, and aftershocks is not necessarily straightforward.

It seems clear that even if the asperity model is correct, the number of foreshocks and the degree of waveform similarity among them will depend on the number, strength, and distribution of asperities involved. Furthermore, it is possible that failure of weaker asperities could produce small groups of similar events at any time. These complications must be considered when investigating the asperity model using waveforms.

In this study we test the predictions of the asperity model regarding temporal variations of waveform and spectra of small earthquakes along major faults. The data we use are digitally-recorded seismograms from the CEDAR system (Johnson, 1979) of preshocks and aftershocks of the October 15, 1979, M_L (local magnitude) 6.6 Imperial Valley earthquake. The low detection threshold and high location resolution of CEDAR and the California Institute of Technology/U.S. Geological Survey southern California array enables comparison of many events from small (<5 km) source regions during different time periods, which was not possible in most previous studies of waveforms and spectra. Since the CEDAR system has only been in operation since January 1, 1977, the time span of observations is rather short compared to the time between the last two major earthquakes along the Imperial fault (39 years). Nevertheless, if we consider these aftershocks and

preshocks to be representative of the beginning and end of the seismic cycle, respectively, then some information regarding longer-term temporal variations can be inferred. We find some evidence to support both predictions of the asperity model outlined above. However, on the basis of this study it appears that waveform is a more reliable indicator of stress conditions along faults than is frequency content.

Selection of Events and Stations

The 1979 Imperial Valley earthquake was accompanied by right-lateral surface faulting along the northernmost 30 km of the Imperial fault (Figure 2-1), with coseismic displacements exceeding 40 cm in some places (K. Sieh, written communication, 1979). Along the northern half of the rupture zone, vertical slip (NE side down) of up to 30 cm also occurred. A segment of the Brawley fault, east of the Imperial fault, also broke during the earthquake. The 1979 faulting was very similar to the faulting which occurred in 1940 along the northern part of the Imperial fault. However, the 1940 earthquake also produced very large right-lateral offsets (up to 5.8 m) on the southern half of the fault (Richter, 1958, pp. 489-491).

The mainshock epicenter of Chavez et al. (1982), calculated using stations in both the United States and Mexico, is located in Mexico about 8 km SE of the nearest surface faulting. Figure 2-1 shows the Caltech-USGS preliminary epicenter, which is slightly too far to the south, together with all well-located (epicentral error of less than 5 km) earthquakes in the area for the $3\frac{1}{2}$ months preceding the mainshock.

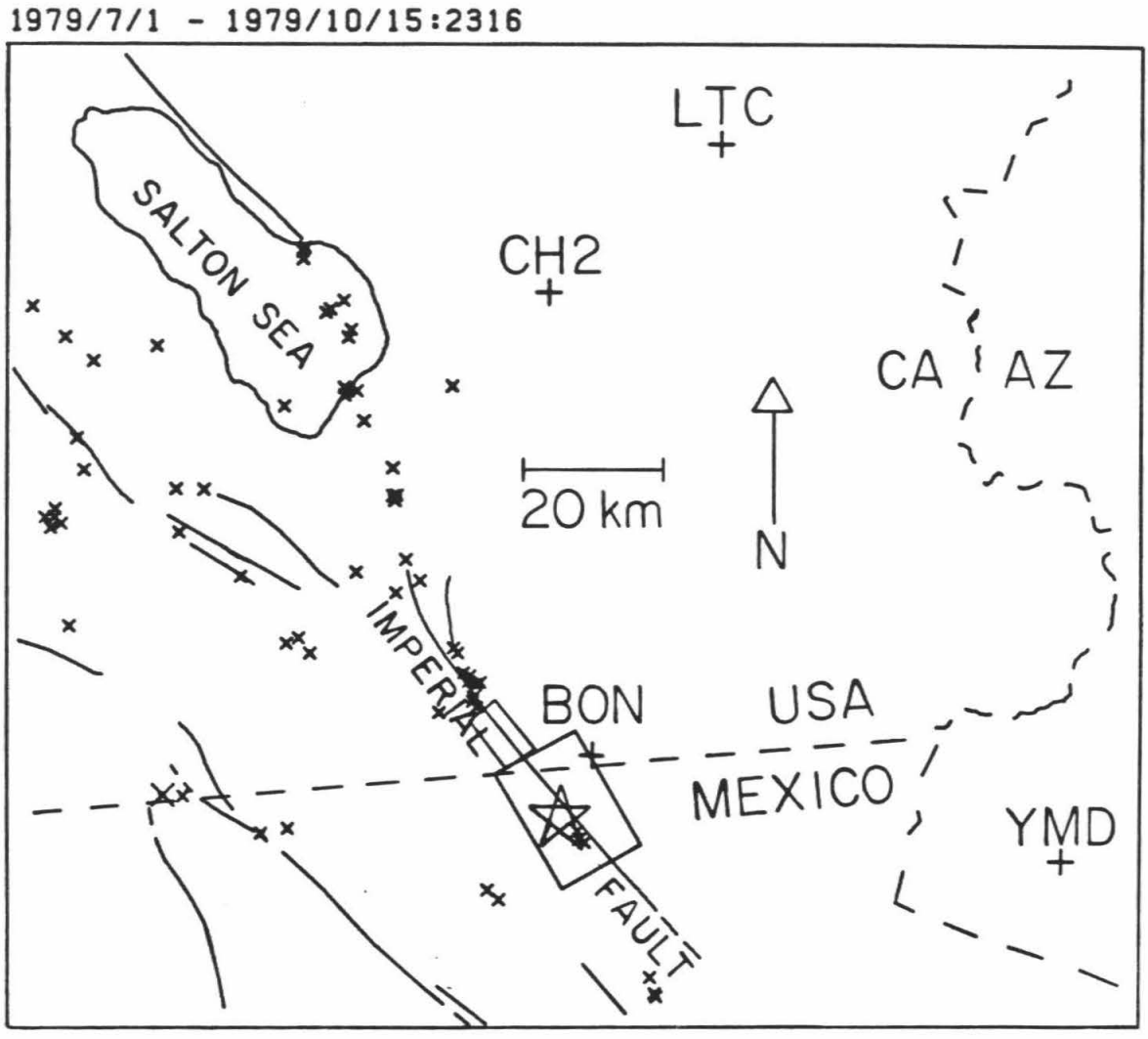

Figure 2-1. Map of Imperial Valley and surrounding area showing major faults (Jennings et al., 1975), key seismographic stations, and all well-located epicenters (epicentral error of less than 5 km) from the preliminary Caltech-USGS catalog for the period July 1, 1979, to October 15, 1979, 2316 (the time of the M_L 6.6 mainshock). The small crosses are $M_L<3.0$ events and the large crosses are events with $3.0 \leq M_L < 4.0$. The large star is the preliminary mainshock epicenter. The solid boxes show the areas for which relocations were done (Figures 2-2 and 2-3). The north-striking fault near the northern end of the Imperial fault is the Brawley fault (Sharp, 1976). The northwest-striking fault on the northeast side of the Salton Sea is the San Andreas fault.

This time period was reported by Johnson and Hutton (1982) to be anomalously quiet. Note that there are only three events during this period within ~15 km of the impending mainshock epicenter. This pattern of quiescence over a large part of the fault, accompanied by clustering near the future hypocenter, is often observed before large earthquakes (Kanamori, 1981). The aftershocks of the 1979 earthquake were concentrated at the northern end of the fault, but there was also significant aftershock activity along the central part of the rupture zone (Johnson and Hutton, 1982).

In looking for temporal changes, it is desirable to minimize changes in the source-receiver geometry and to compare events of roughly the same size. We therefore decided to select two small sections of the fault for study and to look at all $M_L \geq 2.0$ events from these areas. We chose this size range because most of the events in the regions of interest were less than magnitude 3 and the estimated uniform detection threshold in the border region is magnitude 2 (Johnson, 1979).

One place that is clearly of interest is the spot near the mainshock epicenter where three events occurred during the quiet period preceding the mainshock. In order to find previous events and aftershocks from this area, we relocated all $M_L \geq 2.0$ events from the box surrounding the epicenter in Figure 2-1. Relocations were done relative to the hypocenter of Chavez et al. (1982) using the master event technique (Johnson and Hadley, 1976) with the computer program HYPO71 (Lee and Lahr, 1975). The velocity model used was the same as that used by Chavez et al. (1982) (Table 2-1). It is a layered approximation to

TABLE 2-1. Imperial Valley Crustal Velocity Model

P-Wave Velocity of Layer, km/sec	Depth to Top of Layer, km
2.00	0.0
2.40	0.5
2.80	1.0
3.45	2.0
4.10	3.0
4.75	4.0
5.45	5.0
5.80	6.0
6.75	10.0
7.05	10.5
7.20	11.0

From Chavez et al. (1982). Based on refraction studies by Fuis et al. (1982).

the model derived by McMechan and Mooney (1980) for the southern Imperial Valley on the basis of synthetic seismogram modeling of refraction data (Fuis et al., 1982). The model matches P-wave travel times from these earthquakes quite well out to ~120 km distance. Arrival time picks were made by the Caltech-USGS staff as part of the routine data processing. Fifteen stations were used in the relocations, all in the United States and all at epicentral distances of less than 90 km. The absolute value of the average travel time residual was 0.08 sec or less at all these stations.

Figure 2-2 shows relocations of earthquakes from the time of the installation of the Imperial Valley array in July 1973 through July 1980. Relocated epicenters tend to be a few kilometers north and east of the catalog epicenters, consistent with the approximately 3 km north-northeastward shift of the mainshock location of Chavez et al. (1982) relative to the Caltech-USGS mainshock location. The relocated epicenters are more tightly aligned along the Imperial fault than those in the catalog. The depths for the relocated hypocenters are all less than 12 km, whereas many of the catalog depths are deeper than this, down to 23 km. This is because the standard locations are determined with an average southern California velocity model that does not include the thick layer of low-velocity sedimentary rocks at the surface in the Imperial Valley. The dashed box in Figure 2-2 shows the source area that we chose to investigate, $4^1/_2$ km by $1^1/_2$ km. The box includes the three preshocks shown in Figure 2-1, five additional preshocks for which digital data are available, and five aftershocks (Table 2-2). Local

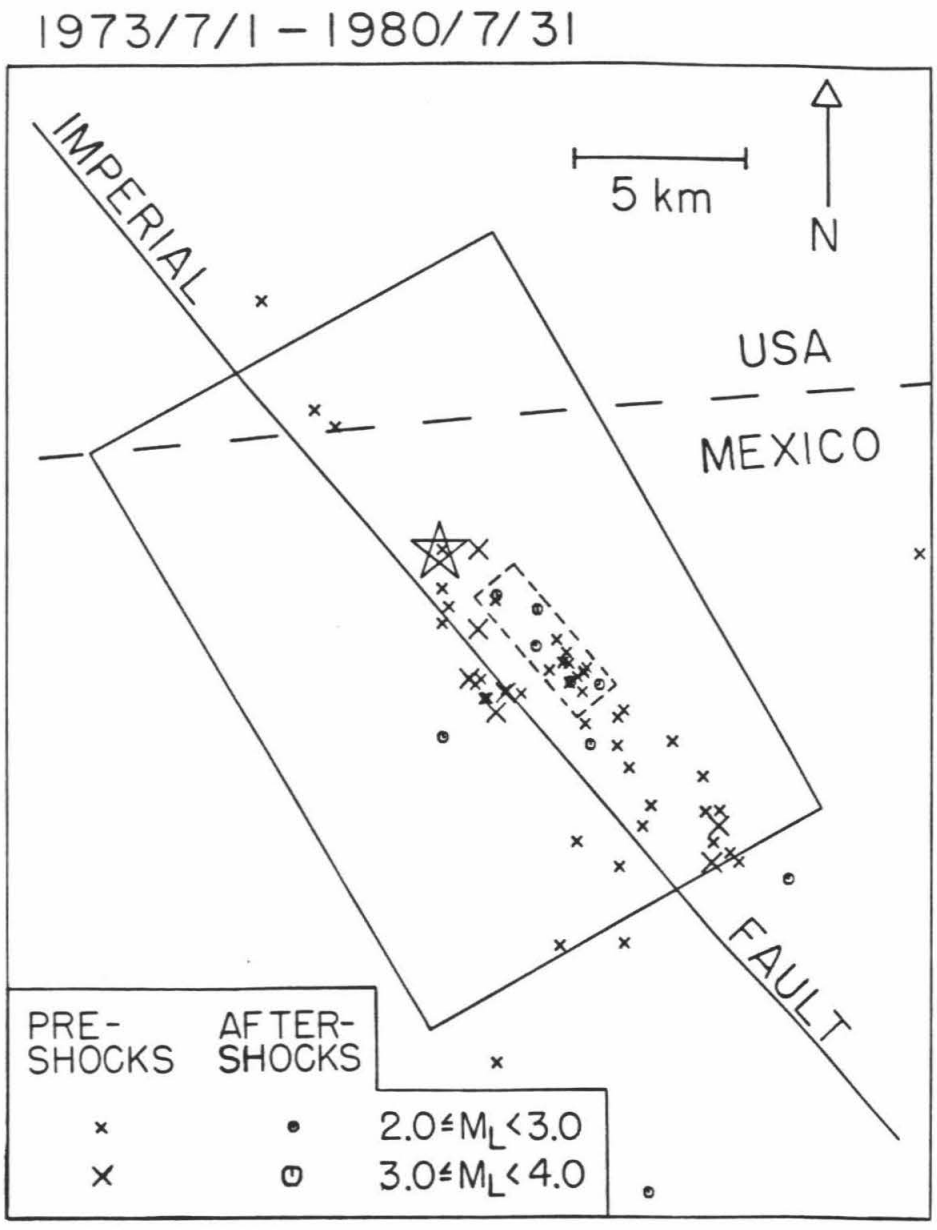

Figure 2-2. Relocated epicenters for all $M_L \geq 2.0$ events in the solid box from July 1, 1973, to July 31, 1980. The mainshock location of Chavez et al. (1982) (star) was used as a master event for the relocations. The dashed box encloses the events selected for study (Table 2-2).

TABLE 2-2. Relocated Hypocenters in Dashed Box in Figure 2-2

Date	Time	Latitude	Longitude	Depth, km	M_L	
May 13, 1974	1744:48.58	32°36.77′	115°15.87′	9.4	2.2	*
April 9, 1976	2347:52.46	32°36.73′	115°16.56′	9.5	2.2	*
Aug. 28, 1977	1607:40.62	32°36.85′	115°16.31′	9.4	2.4	
Sept. 15, 1977	2016:56.41	32°36.40′	115°15.95′	9.1	2.4	
June 8, 1978	0015:31.49	32°36.69′	115°15.93′	9.3	2.4	
Aug. 4, 1978	0059:58.29	32°37.01′	115°16.24′	9.5	2.4	
May 11, 1979	1924:32.78	32°36.84′	115°16.20′	9.6	2.4	
Aug. 7, 1979	1637:32.59	32°37.21′	115°16.42′	9.9	2.5	
Aug. 25, 1979	0440:46.01	32°36.54′	115°16.19′	9.6	2.5	
Sept. 10, 1979	1527:00.35	32°36.72′	115°15.93′	9.4	2.2	
Oct. 17, 1979	1106:50.72	32°37.69′	115°16.78′	8.7	2.0	
Oct. 27, 1979	2154:40.78	32°37.12′	115°16.81′	7.6	2.8	
Nov. 10, 1979	2035:42.97	32°37.91′	115°17.53′	9.5	2.6	
Dec. 17, 1979	0918:17.33	32°36.56′	115°16.17′	10.0	2.5	
May 21, 1980	0853:55.94	32°36.52′	115°15.64′	9.2	2.0	

* Digital data unavailable

magnitudes range from 2.2 to 2.5 for the preshocks and from 2.0 to 2.8 for the aftershocks. The calculated depths, although not well constrained, are all in the range 7-10 km.

A second region of interest is shown by the small solid box just north of the border in Figure 2-1. We decided to select a cluster of events for study from this section of fault because (1) coseismic and postseismic surface displacements were largest there, (2) strong motion modeling by Hartzell and Helmberger (1982) and LeBras (1981) suggests large subsurface slip in this area, up to 2.5 m, and (3) this section of fault straddles the boundary between the Brawley seismic zone to the NW and a 10-15 km nearly aseismic zone along the Mexican border, which separates the 1979 mainshock epicenter from the 1940 epicenter (Johnson and Hutton, 1982). The relocation procedure for this box was the same as for the box to the south except that the master event used was a well-located M_L 2.7 preshock on December 7, 1978, from the NW end of the box. Sixteen stations were used, all at distances less than 90 km. The absolute value of the average travel time residual for these master event relocations was 0.05 sec or less at 15 out of the 16 stations. The average residual for the other station was 0.20 s, probably because the first arrival was missed in some cases.

Figure 2-3 shows relocated epicenters of all $M_L \geq 2.0$ events from this area for the period January 1977 through March 1981. The relocated epicenters are again more tightly grouped along the fault trace, and many of the locations are several kilometers shallower than those in the catalog because of the different velocity model used. Because most of

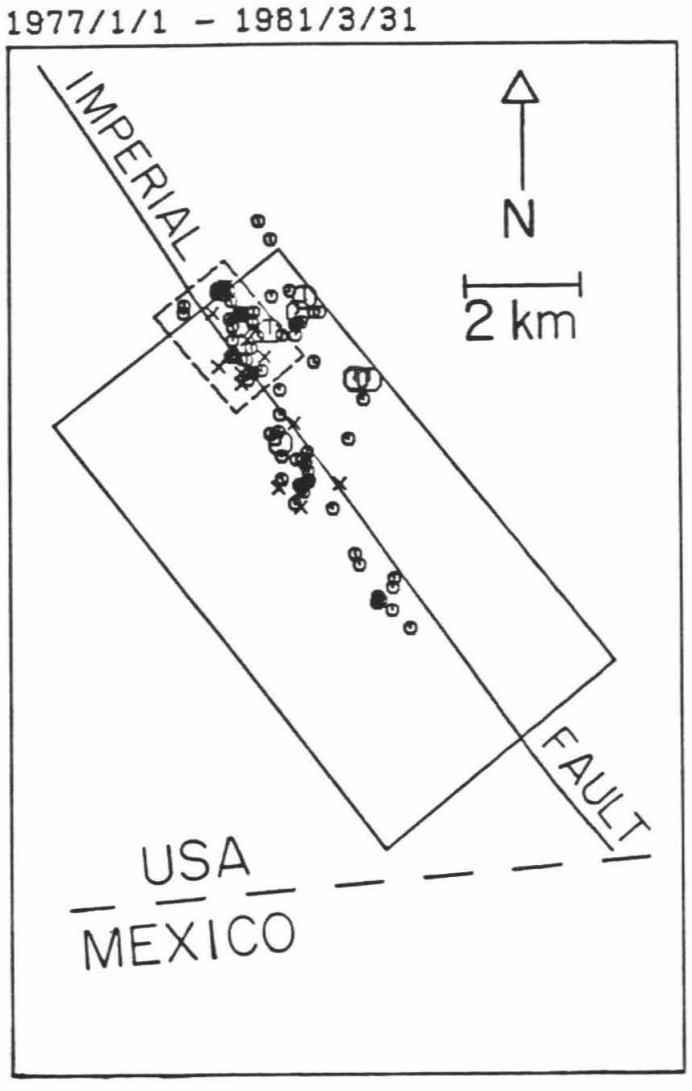

Figure 2-3. Relocated epicenters for all $M_L \geq 2.0$ events in the solid box from January 1, 1977, to March 31, 1981. The master event used was an M_L 2.7 preshock on December 7, 1978, located within the area selected for detailed study (dashed box). Magnitude key same as in Figure 2-2.

TABLE 2-3. Relocated Hypocenters in Dashed Box in Figure 2-3

Date	Time	Latitude	Longitude	Depth, km	M_L	
Dec. 14, 1977	0317:27.72	32°45.49′	115°25.75′	9.0	2.0	
Feb. 24, 1978	0636:38.37	32°44.93′	115°25.44′	4.4	2.4	
Feb. 24, 1978	0638:10.06	32°44.83′	115°25.44′	9.4	2.1	
Feb. 24, 1978	0758:27.44	32°44.99′	115°25.69′	10.1	2.0	
Dec. 7, 1978	2213:22.18	32°45.49′	115°25.44′	10.2	2.7	+
Dec. 8, 1978	0202:00.93	32°45.08′	115°25.19′	10.2	2.4	
Dec. 8, 1978	0838:23.01	32°45.74′	115°25.61′	11.2	2.8	
Dec. 8, 1978	0842:18.57	32°45.49′	115°25.44′	10.1	2.6	
Dec. 8, 1978	0847:48.47	32°45.49′	115°25.44′	10.4	2.7	
Dec. 9, 1978	0217:41.62	32°45.24′	115°25.38′	10.9	2.8	
Oct. 16, 1979	0048:03.41	32°45.32′	115°25.13′	10.1	3.1	**
Oct. 16, 1979	0953:47.57	32°45.49′	115°26.07′	10.1	2.7	*
Oct. 16, 1979	1703:33.04	32°45.56′	115°26.06′	9.6	2.5	
Oct. 16, 1979	1916:51.95	32°45.60′	115°25.56′	10.1	2.6	
Oct. 17, 1979	0506:42.96	32°45.05′	115°25.39′	10.1	2.1	
Oct. 17, 1979	0937:59.16	32°45.16′	115°25.34′	10.1	2.7	
Oct. 17, 1979	2307:03.62	32°45.28′	115°25.00′	10.6	2.2	
Oct. 19, 1979	0310:44.19	32°45.43′	115°25.57′	10.1	2.6	
Oct. 22, 1979	1922:27.44	32°45.67′	115°25.71′	10.1	2.2	
Oct. 24, 1979	0552:51.21	32°45.10′	115°25.53′	9.6	2.3	
Oct. 24, 1979	0619:04.68	32°45.69′	115°25.57′	10.1	2.7	**
Oct. 26, 1979	0911:16.68	32°45.39′	115°25.32′	10.9	2.5	
Oct. 28, 1979	0203:43.33	32°45.23′	115°25.54′	10.1	2.2	
Oct. 28, 1979	1621:31.41	32°45.46′	115°25.44′	10.2	2.0	**
Oct. 29, 1979	0204:53.55	32°45.49′	115°25.30′	9.6	2.3	**
Oct. 29, 1979	0647:55.70	32°45.49′	115°25.46′	10.1	2.7	
Oct. 30, 1979	2101:48.34	32°45.36′	115°25.54′	10.1	2.7	
Oct. 31, 1979	1708:34.17	32°45.08′	115°25.56′	10.8	2.3	
Nov. 2, 1979	2145:29.24	32°45.66′	115°25.63′	10.1	2.7	
Nov. 7, 1979	0200:54.77	32°44.95′	115°25.22′	10.1	2.4	
Nov. 7, 1979	1426:33.31	32°45.71′	115°25.70′	10.1	2.2	
Nov. 7, 1979	1433:22.70	32°45.73′	115°25.62′	10.1	2.2	
Nov. 9, 1979	2303:57.35	32°45.37′	115°25.48′	10.1	3.0	**
Nov. 10, 1979	0223:41.73	32°45.27′	115°25.26′	10.1	2.2	
Nov. 11, 1979	1532:45.66	32°45.42′	115°25.32′	10.2	2.7	
Nov. 11, 1979	1559:23.47	32°45.49′	115°25.31′	10.7	2.4	
Nov. 16, 1979	1435:04.95	32°44.93′	115°25.31′	9.1	2.4	
Nov. 19, 1979	1845:00.31	32°44.86′	115°25.37′	10.7	2.8	
Nov. 25, 1979	0856:31.20	32°45.47′	115°25.46′	10.1	2.1	
Feb. 25, 1981	2021:02.53	32°45.06′	115°25.44′	10.1	2.1	

\+ Master event
* Digital data unavailable
** Unuseable (multiple event)

the preshocks which we relocated were near the NW edge of the box, we selected the subset of events within the $1^1/_2$ by 2 km dashed box (Figure 2-3) for study. These events, 10 preshocks and 30 aftershocks, are listed in Table 2-3. Six of the aftershocks could not be used, either because seismic waves from another aftershock were arriving concurrently or because CEDAR data were not available. The magnitude range for both the preshocks and the useable aftershocks is 2.0-2.8. The depths of most of the events are 9-11 km. In general, these hypocenters are more accurate than those from south of the border (Table 2-2 and Figure 2-2) because the stations are closer and better distributed in azimuth.

Selection of stations for waveform and spectral studies was complicated by clipping of some of the signals during telemetry and by changes in instrumentation during the time period of interest. Changes in instrumentation implemented at most of the southern Imperial Valley stations on July 17, 1979, unfortunately rendered them unuseable for our purposes. At this time, Airpax discriminators were replaced with modified J-101 discriminators equipped with antialiasing filters. Since the Airpax discriminators showed considerable variation in frequency response from one unit to another (C. Koesterer, personal communication, 1980), it would have been difficult to correct for the change by digital filtering. Modified J-101 discriminators were also installed at stations in the southeastern Mojave desert several months earlier. Some of these stations, however, were previously equipped with unmodified J-101 discriminators, for which the response is well known. Using analytic expressions for the modified and unmodified system

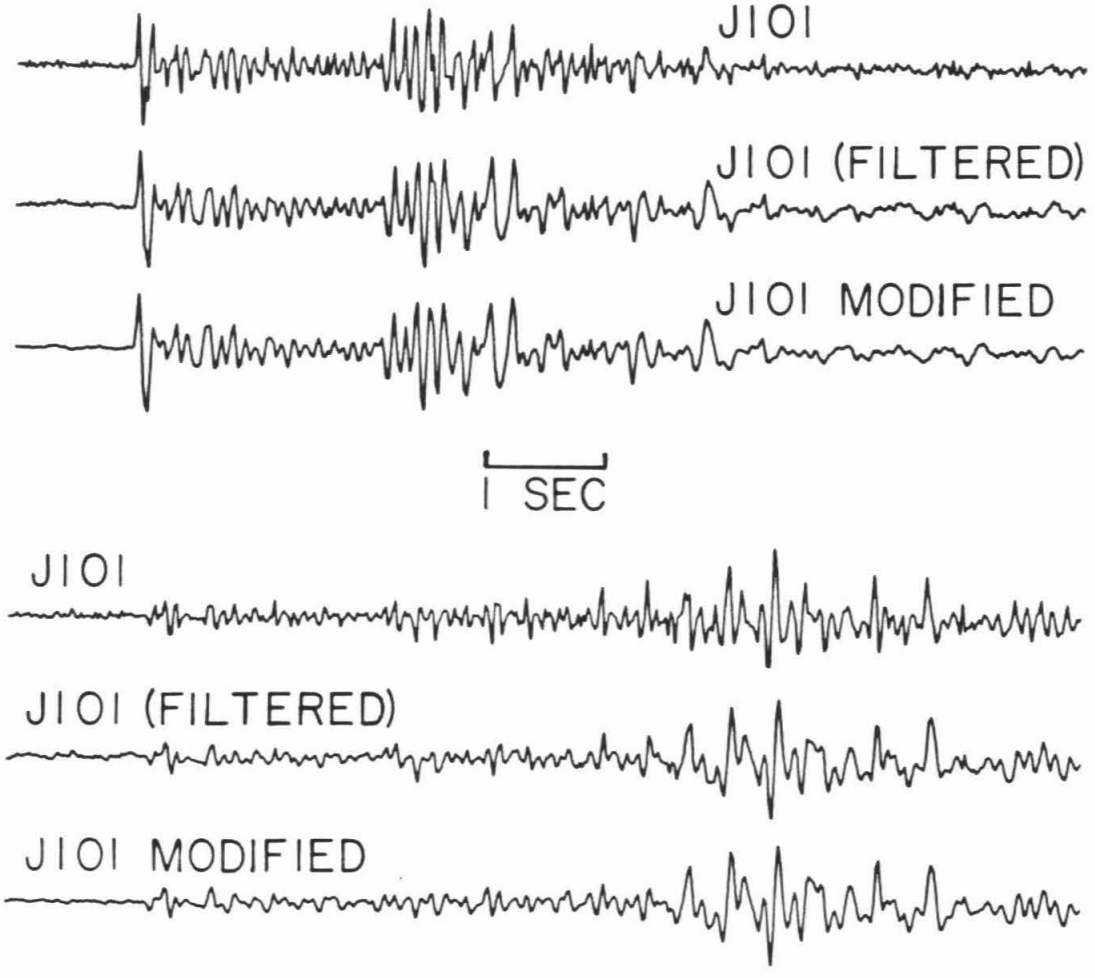

Figure 2-4. Test of digital filter to compensate for change of instrumentation. Traces labeled J-101 were recorded through J-101 discriminators, and those labeled J-101 modified were recorded through modified J-101 discriminators. Traces labeled J-101 (filtered) were recorded through J-101 discriminators and then filtered with a digital filter that approximates the modifications made to the J-101. The examples shown are from an M_L 1.8 event on May 26, 1978, near San Gorgonio Pass. Top records are from station WWR (Δ=10 km), and bottom records are from station RMR (Δ=34 km).

responses from Archambeau (1979), we designed a time-domain digital filter to mimic the instrumentation change. Figure 2-4 shows a test of this filter. The top seismogram in each group was recorded using the unmodified instrumentation, and the bottom one was recorded using the modified instrumentation. The second trace is the digitally filtered version of the first trace, and in both cases it resembles the third trace quite closely. This procedure is valid as long as the original signal does not contain significant energy above 25 Hz, the Nyquist frequency of CEDAR.

Good recordings of most of the events in Tables 2-2 and 2-3 were available at three stations for which it was possible to correct for the instrumentation change: YMD, CH2, and LTC (Figure 2-1). The standardized frequency response of these instruments is reasonably broadband, within a factor of 4 of the peak amplitude response (near 7 Hz) over the range 1-16 Hz (Archambeau, 1979). These stations were used for the studies of waveform and spectra discussed in the following sections.

Waveforms and Focal Mechanisms

Seismograms for events in the dashed box in Figure 2-2 (Table 2-2) are shown in Figures 2-5, 2-6, and 2-7. The change in instrumentation has been corrected for, and the instrument response has been deconvolved in the passband 1-16 Hz. Horizontal lines separate the preshocks from the aftershocks. At all three stations, the preshocks show remarkable similarity in waveform and in relative arrival times and amplitudes of

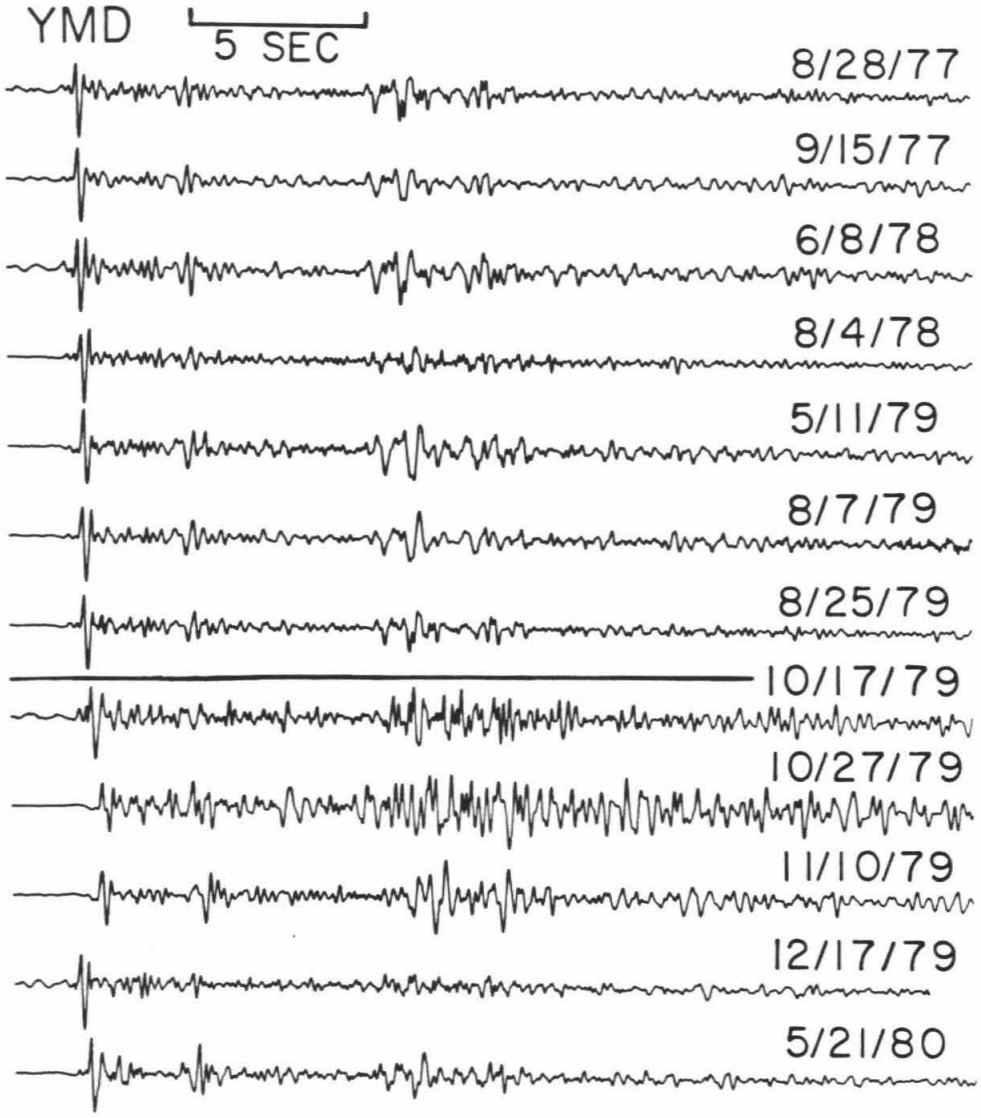

Figure 2-5. Vertical component seismograms recorded at YMD ($\Delta \simeq 68$ km) for earthquakes from the dashed box in Figure 2-2. The instrument response has been deconvolved in the passband 1-16 Hz. Seismograms are plotted with the same maximum amplitude and positioned horizontally according to the recalculated origin times. Note that the preshock records are all very similar to one another, whereas the aftershocks show more variability.

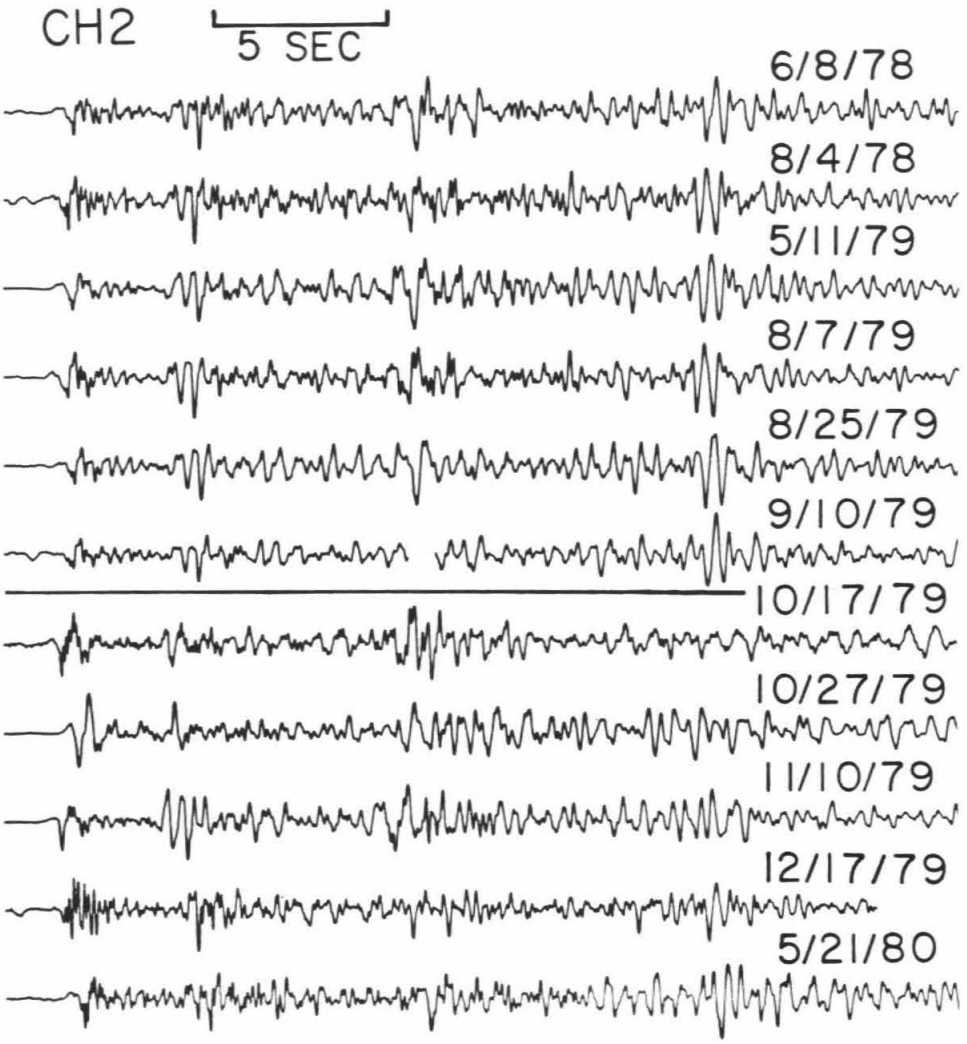

Figure 2-6. Deconvolved seismograms recorded at CH2 ($\Delta \simeq 76$ km). See Figure 2-5 for explanation. The data gap during the arrival of the third prominent phase from the September 10, 1979, event was caused by a disk drive failure.

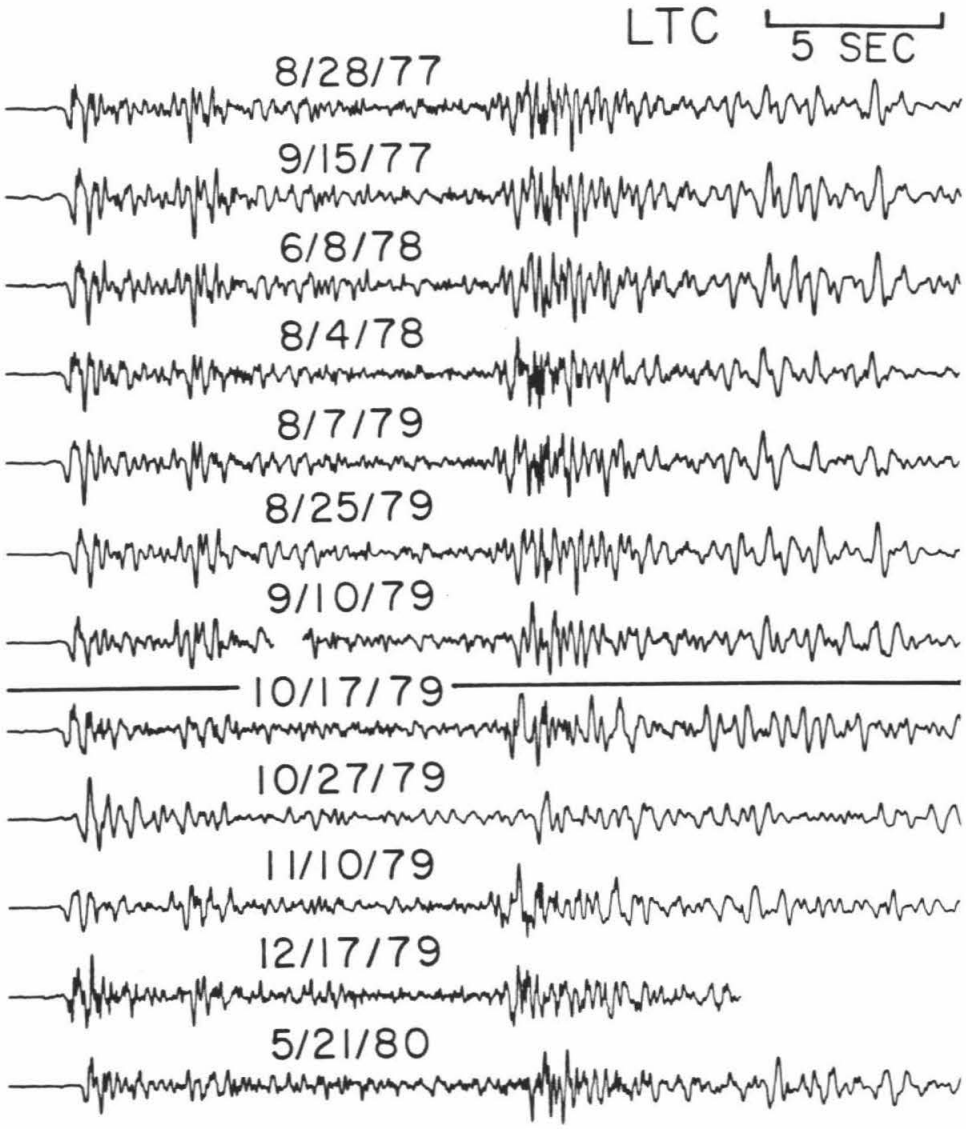

Figure 2-7. Deconvolved seismograms recorded at LTC ($\Delta \simeq 99$ km). See Figure 2-5 for explanation. The data gap at ~7 sec after arrival of the P wave from the September 10, 1979, event was caused by a disk drive failure.

various phases over the entire record length (~30 s). Because the character of the record is controlled by scattering from velocity heterogeneities in the crust, the similarity of the waveforms implies similar source mechanisms and hypocenters within $^1/_4$ of the shortest wavelength to which the similarity extends (Geller and Mueller, 1980). Available first motion data for the preshocks support the inference of similar source mechanisms (Figure 2-8), but by themselves are inadequate to constrain the solutions. However, SV/P amplitude ratios for these preshocks at station BON ($\Delta \approx 9$ km), together with the available first motions, suggest right-lateral strike-slip on a NW-striking plane or left-lateral strike-slip on a NE-striking plane (C. Jones, personal communication, 1980).

Seismograms of preshocks from this area are much more similar to one another at each station than seismograms of aftershocks. To demonstrate this, we cross correlated the seismograms. The normalized cross-correlation function $c_{xy}(m)$ for two real time series x and y of length N is given by

$$c_{xy}(m) = \frac{\frac{1}{N-|m|} \sum_n x(n)y(n+m) - \overline{x(n)}\ \overline{y(n+m)}}{\sqrt{\overline{x^2(n)} - \overline{x(n)}^2}\ \sqrt{\overline{y^2(n+m)} - \overline{y(n+m)}^2}}$$

where the bar indicates the mean

$$\overline{x(n)} = \frac{1}{N-|m|} \sum_n x(n)$$

and the summation is from n=0 to n=N-m-1 for $m \geq 0$ and from n=|m| to n=N-1 for $m<0$. The maximum of $c_{xy}(m)$ for $|m| \leq N/4$ for each pair of consecutive

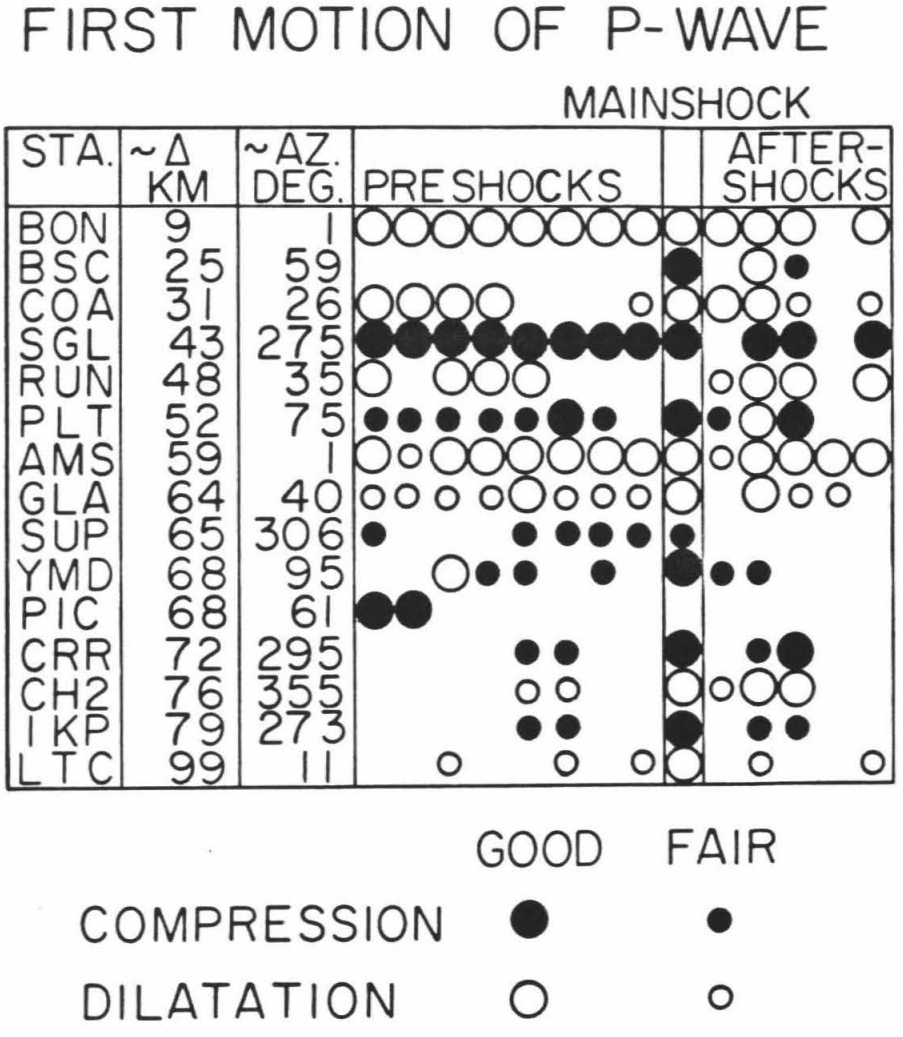

Figure 2-8. First motion readings for events shown in Figures 2-5, 2-6, and 2-7.

events is plotted versus time in Figure 2-9. These graphs show clear changes at the time of the mainshock, indicated by the vertical bar. Figure 2-10 shows for all possible event pairs the mean of the maximum $c_{xy}(m)$ values calculated for the three different stations. Each mean peak correlation is represented by a circle, where the radius of the circle is proportional to the mean peak correlation value. Values greater than or equal to 0.6 are shown by open circles and smaller values are shown by solid circles. It is evident from this figure that the preshocks display much greater coherency in waveform than do the aftershocks. The average peak correlation between preshocks (upper left box) is 0.74, whereas mean peak correlations between aftershocks (lower right box) are all small, less than 0.3, with an average value of only 0.23. The last two aftershocks correlate more strongly with the preshocks than the first three aftershocks do, but still not as strongly as most preshocks correlate with each other.

Examples of the cross-correlation function $c_{xy}(m)$ are shown in Figure 2-11. For well-correlated pairs of seismograms (top four examples), this function is sharply peaked near lag m=0 sec. For poorly-correlated pairs of seismograms (bottom four examples), this peak is small or nonexistent. Thus, the maximum value of $c_{xy}(m)$ appears to be a robust measure of the similarity of two seismograms.

As mentioned above, the similarity of the preshock waveforms places a strong constraint on the maximum distance between the hypocenters. To help quantify this constraint, we cross correlated selected pairs of seismograms after bandpass filtering them in four one-octave passbands.

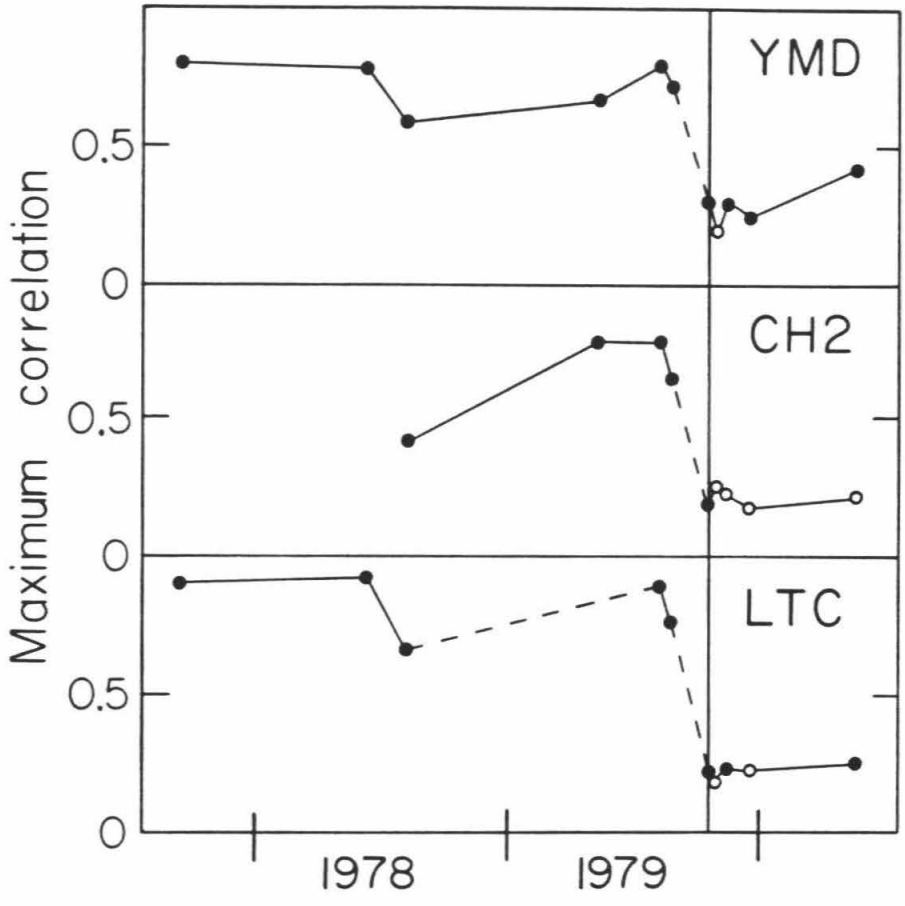

Figure 2-9. Maximum cross correlation between each seismogram in Figures 2-5, 2-6, and 2-7 and the one directly above it, plotted as a function of time. The vertical bar marks the time of the mainshock. Solid circles are correlation coefficients corresponding to time lags where the phases are properly aligned. Open circles correspond to lags where the phases are not properly aligned, and hence represent upper limits to the maximum correlation in the sense that these numbers would decrease if the range of allowable lags ($\pm 1/4$ of the record length) was decreased. Thirty seconds of record were used in the cross-correlation calculations, except for the December 17, 1979, event. Dashed lines indicate intervals containing earthquakes that could not be included in this analysis because the records were unavailable or unuseable because of data gaps (see Figures 2-6 and 2-7).

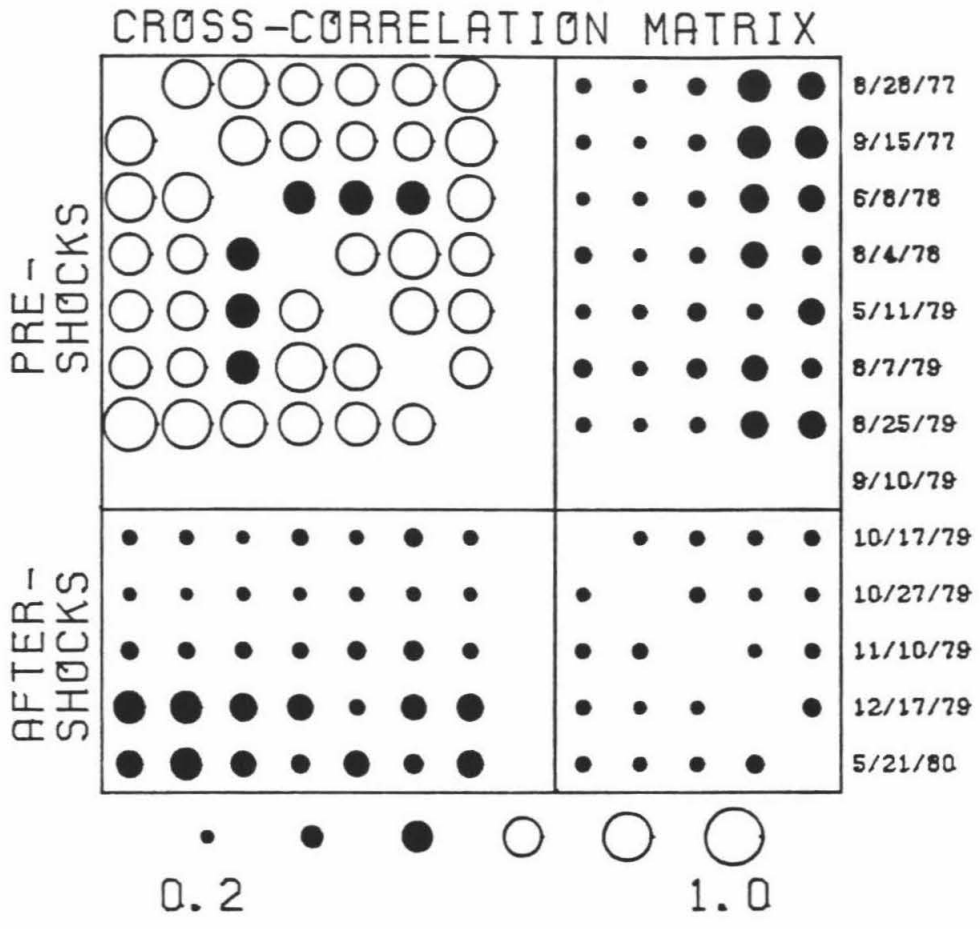

Figure 2-10. The mean of the maximum cross correlations calculated for seismograms from YMD, CH2, and LTC for all possible pairs of events in Figures 2-5, 2-6, and 2-7. Each circle represents the mean peak correlation for the event pair corresponding to its position in the matrix. The radius of the circle is proportional to the correlation value. Circles representing values less than 0.6 are solid.

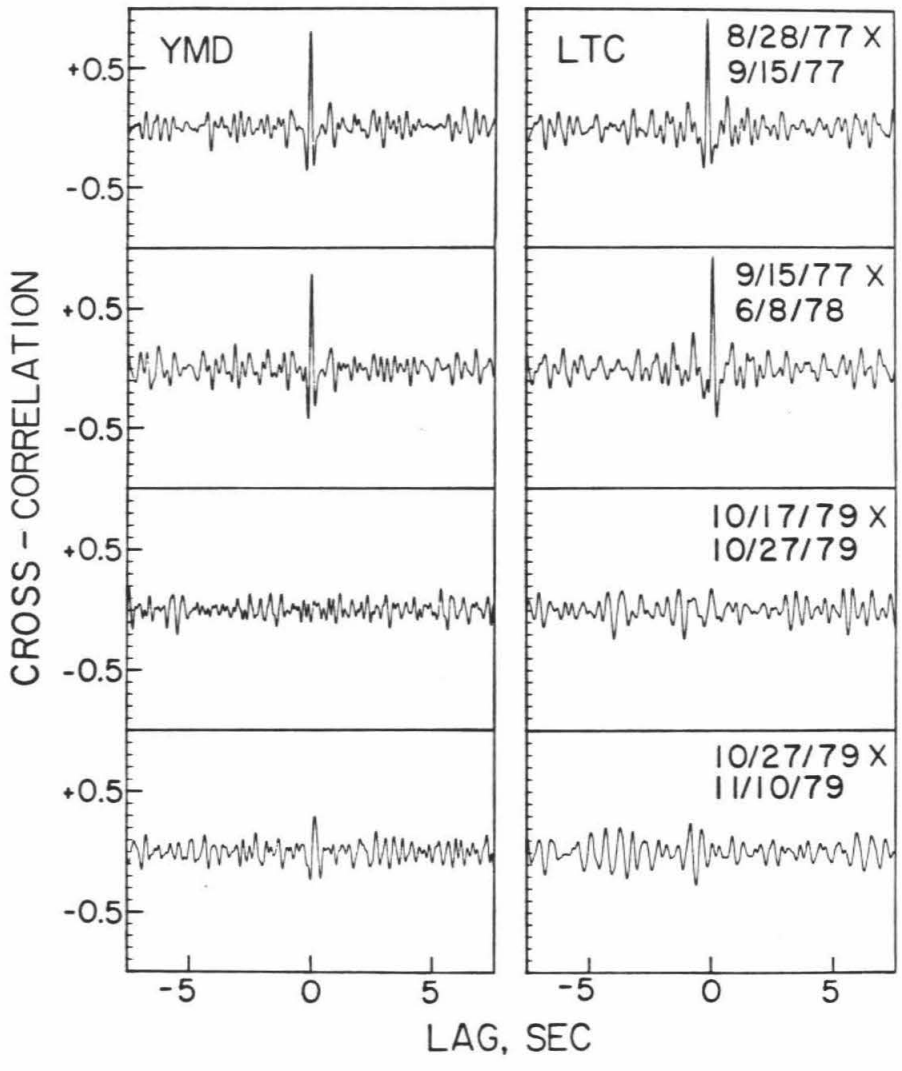

Figure 2-11. Cross-correlation functions calculated from records at YMD (left) and LTC (right) for two pairs of preshocks (top two sets) and two pairs of aftershocks (bottom two sets).

Figure 2-12 shows cross correlations between filtered seismograms for a pair of preshocks (left) and a pair of aftershocks (right). The peaks of these cross-correlation functions are well above the noise for well-correlated events, such as the example on the left in this figure. The peak cross correlations between filtered traces are shown in Figure 2-13 for the event pairs in Figure 2-12 and four other pairs, including the least well-correlated pair of preshocks (June 8, 1978; August 4, 1978). Peak cross correlations for the unfiltered, deconvolved seismograms are shown for reference by the solid symbols at the left of each graph. The preshocks (top four graphs) are well correlated (peak correlations generally ≥ 0.6) up through at least the 2-4 Hz frequency band, whereas the aftershocks shown (bottom two graphs) are not well correlated at any frequency. The near-source P-wave velocity is about 6 km/sec (Tables 2-1 and 2-2) and the S-wave velocity is probably of the order of 3.4 km/sec. At 4 Hz the wavelengths are therefore ~1500 m for P waves and ~850 m for S waves. The similarity of preshock waveforms at these wavelengths and longer implies a maximum event separation of $^1/_4$ wavelength, approximately 200-400 m in this case.

The greater diversity of aftershock waveforms may be due to several factors such as greater variability in location, size, source mechanism, or pattern of stress release. However, there is very little difference in magnitude among these events (Table 2-2) and any changes in mechanism must be small because they are not reflected in the first motion data (Figure 2-8). The rupture time for magnitude 2-3 events is only a few tenths of a second long, so at the frequencies which dominate in these

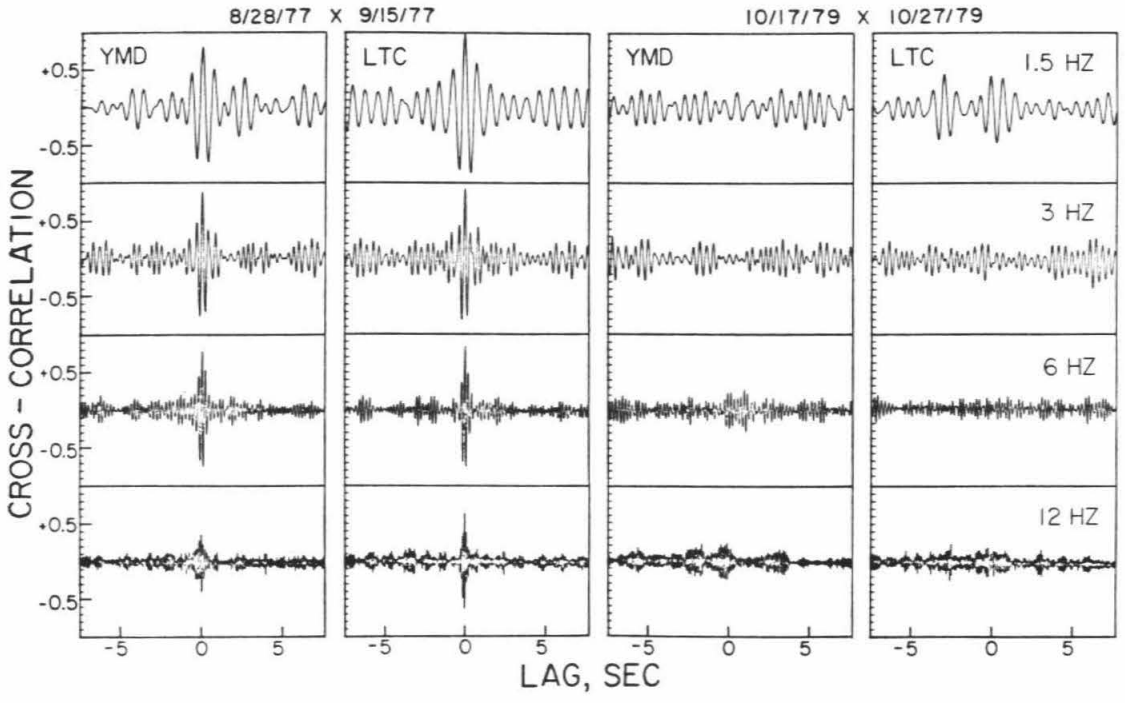

Figure 2-12. Cross-correlation functions calculated after bandpass filtering the deconvolved seismograms in the passbands 1-2, 2-4, 4-8, and 8-16 Hz with third-order recursive Butterworth filters. Results are shown for stations YMD and LTC for a pair of preshocks (left two columns) and a pair of aftershocks (right two columns).

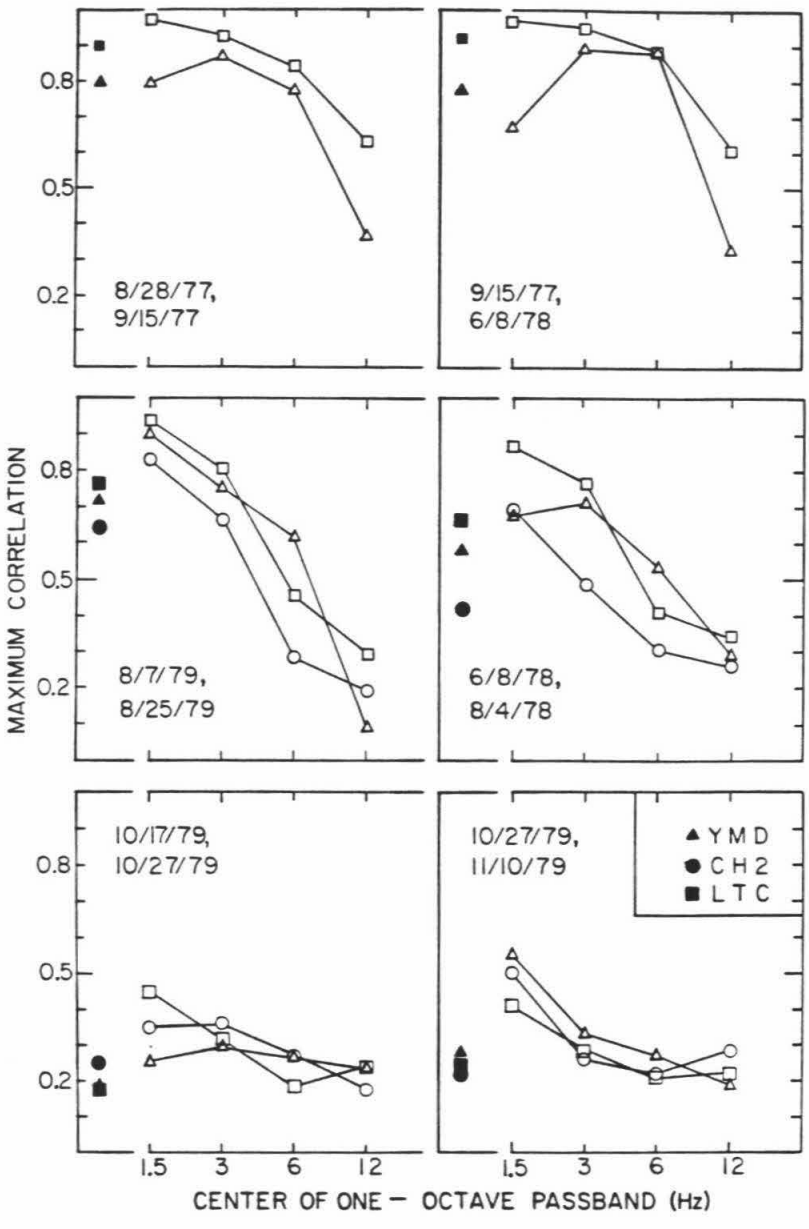

Figure 2-13. Maximum cross correlations between filtered records (open symbols) for selected pairs of preshocks (top four graphs) and aftershocks (bottom two graphs), including the examples in Figure 2-12. Maximum cross correlations for the unfiltered, deconvolved (1-16 Hz) seismograms are shown for reference by the solid symbols at the left of each graph.

records, 3-6 Hz, the waveforms are insensitive to the details of the rupture and are instead dominated by the effects of structure and radiation pattern. It therefore appears that location is the dominant factor controlling the waveforms. This phenomenon is apparently below the resolution of even master event locations, because there is no obvious relationship between waveform and location within the study area.

Seismograms of events from within the dashed box of Figure 2-3 (Table 2-3) are shown in Figures 2-14 and 2-15. These are the original records except that some preshocks have been filtered to correct for the change in instrumentation. The numbers at the left of each seismogram show the maximum correlation between it and the seismogram above it. These numbers are plotted versus time in Figure 2-16, along with analogous peak correlations from station YMD. The mean peak correlations for all possible event pairs are shown in Figure 2-17.

The distinction between preshocks and aftershocks from this source region is not as obvious as for the events from near the epicenter in Figures 2-5 to 2-7. The average peak correlation for pairs of aftershocks (lower right box, Figure 2-17) is 0.43, nearly the same as the average for the preshocks, 0.45 (upper left box). Nevertheless, a close examination of the data suggests that differences exist between the preshock and aftershock periods. Three of the 10 preshocks occurred in a swarm on February 24, 1978, and six occurred in a swarm on December 7-9, 1978. The events within each swarm have very similar waveforms (most peak correlations >0.6), but different from those of the other

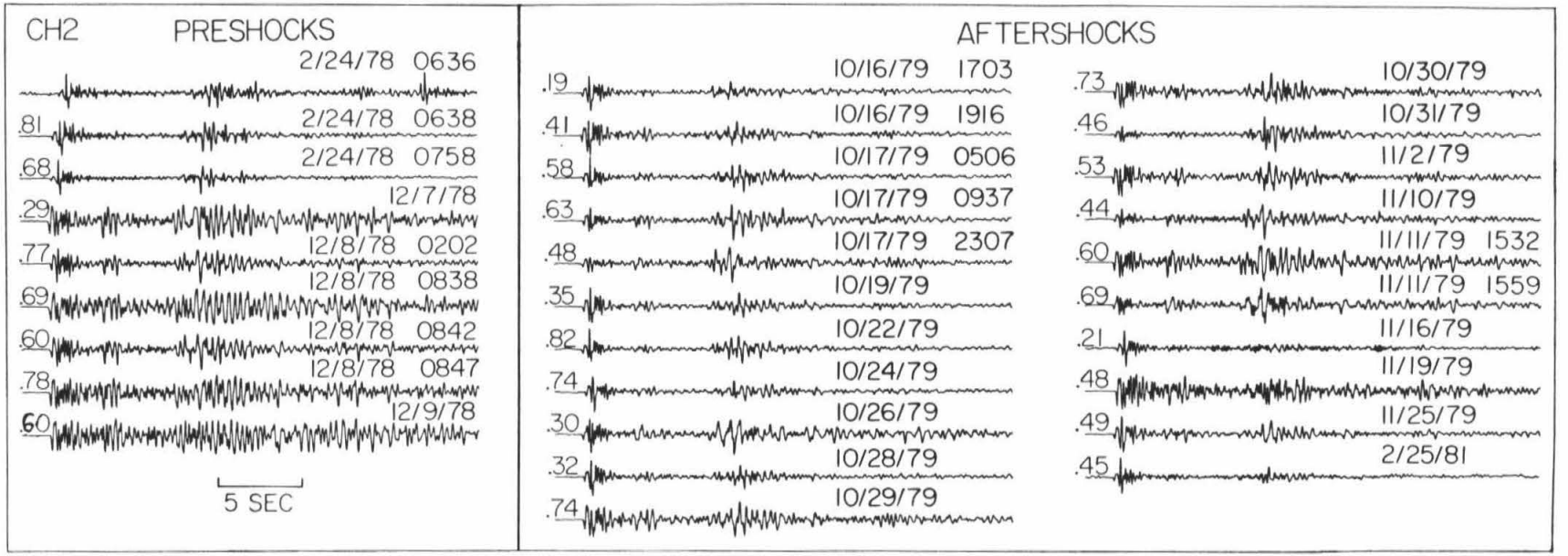

Figure 2-14. Vertical component seismograms for earthquakes from dashed box in Figure 2-3, recorded at station CH2 ($\Delta \simeq 60$ km). Seismograms are plotted with the same maximum amplitude and positioned horizontally within each column according to recalculated origin times. The numbers at the left of each seismogram show the maximum correlation between it and the seismogram above it. Thirty seconds of record were used in the cross-correlation calculations except for the February 24, 1978, 0636 event, where only 22 sec could be used because of the arrival of a P wave from another event.

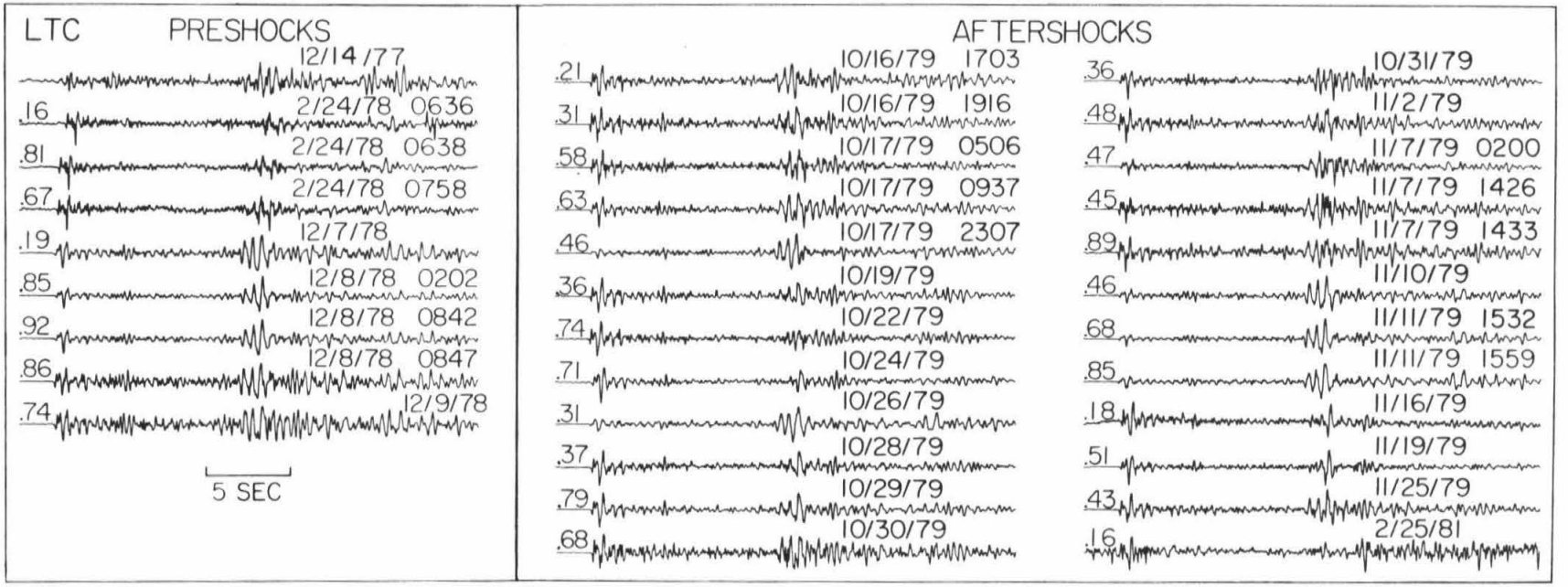

Figure 2-15. Same as Figure 2-14, for station LTC ($\Delta \approx 88$ km). Thirty seconds of record were used in the cross correlations except for the following events: February 24, 1978, 0636 (22 sec); February 24, 1978, 0758 (26 sec); October 24, 1979 (29 sec); October 28, 1979 (28 sec).

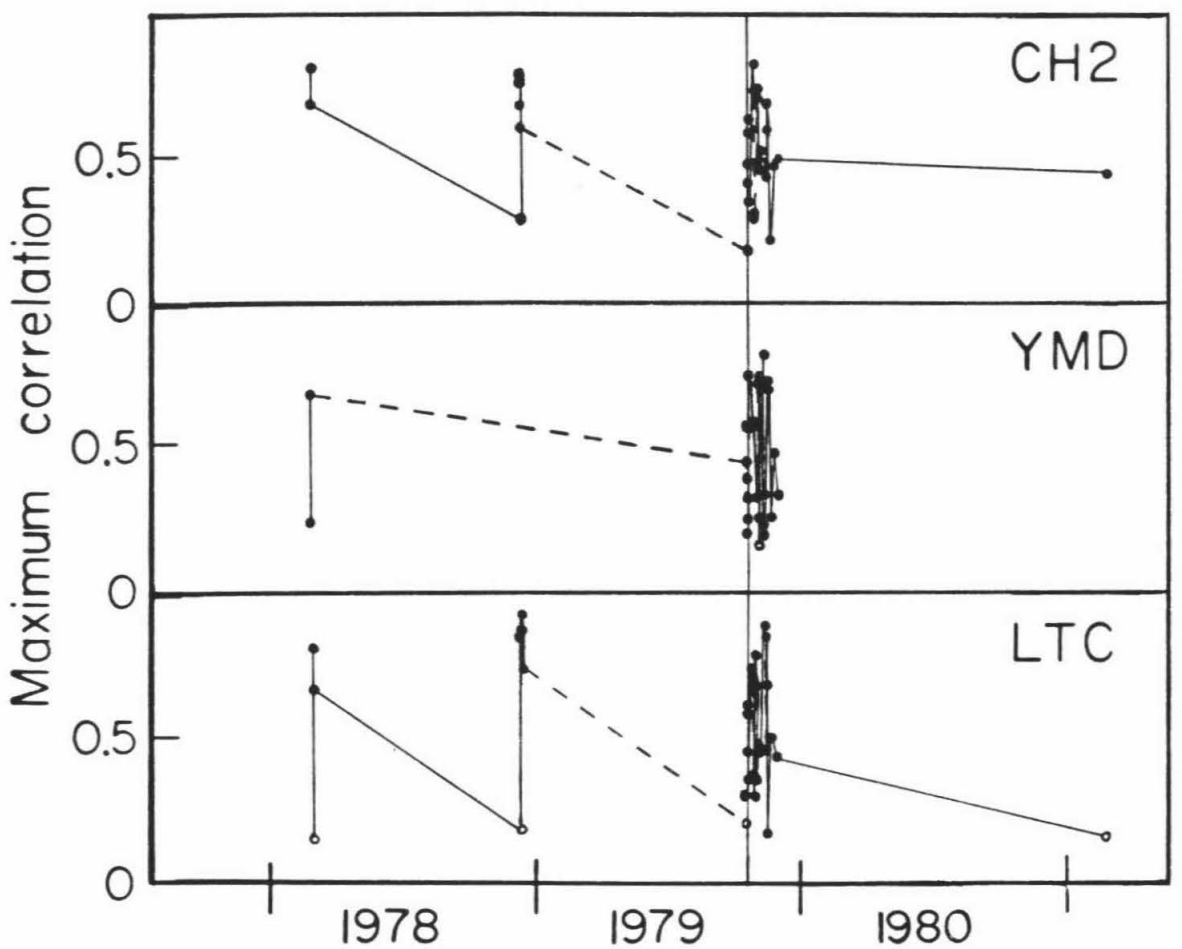

Figure 2-16. Peak correlations from Figures 2-14 and 2-15 and analogous peak correlations from station YMD ($\Delta \approx 85$ km), plotted as a function of time. See Figure 2-9 for explanation. Dashed lines indicate intervals containing earthquakes that could not be included in this analysis because the records were unavailable or unuseable due to interference from other events.

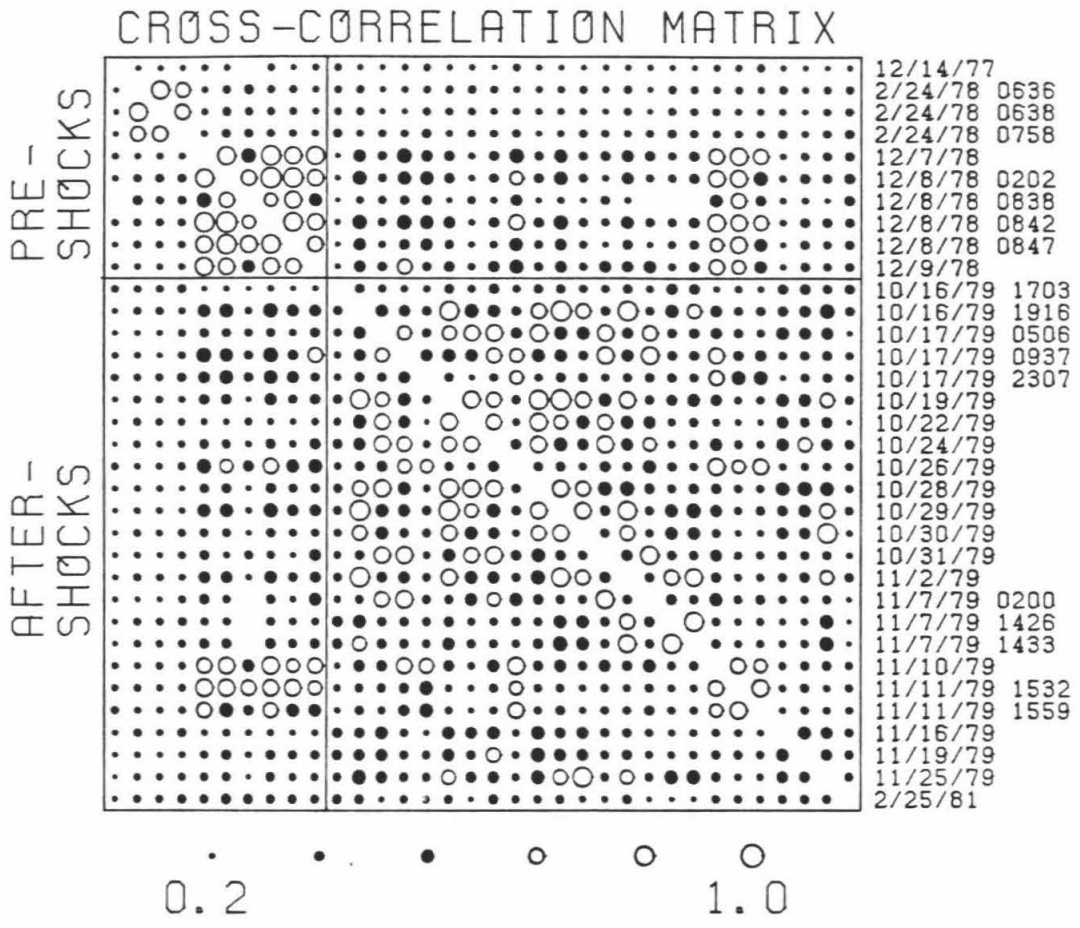

Figure 2-17. The mean of the maximum cross correlations calculated for seismograms from YMD, CH2, and LTC for all possible event pairs in Figures 2-14 and 2-15. See Figure 2-10 for explanation.

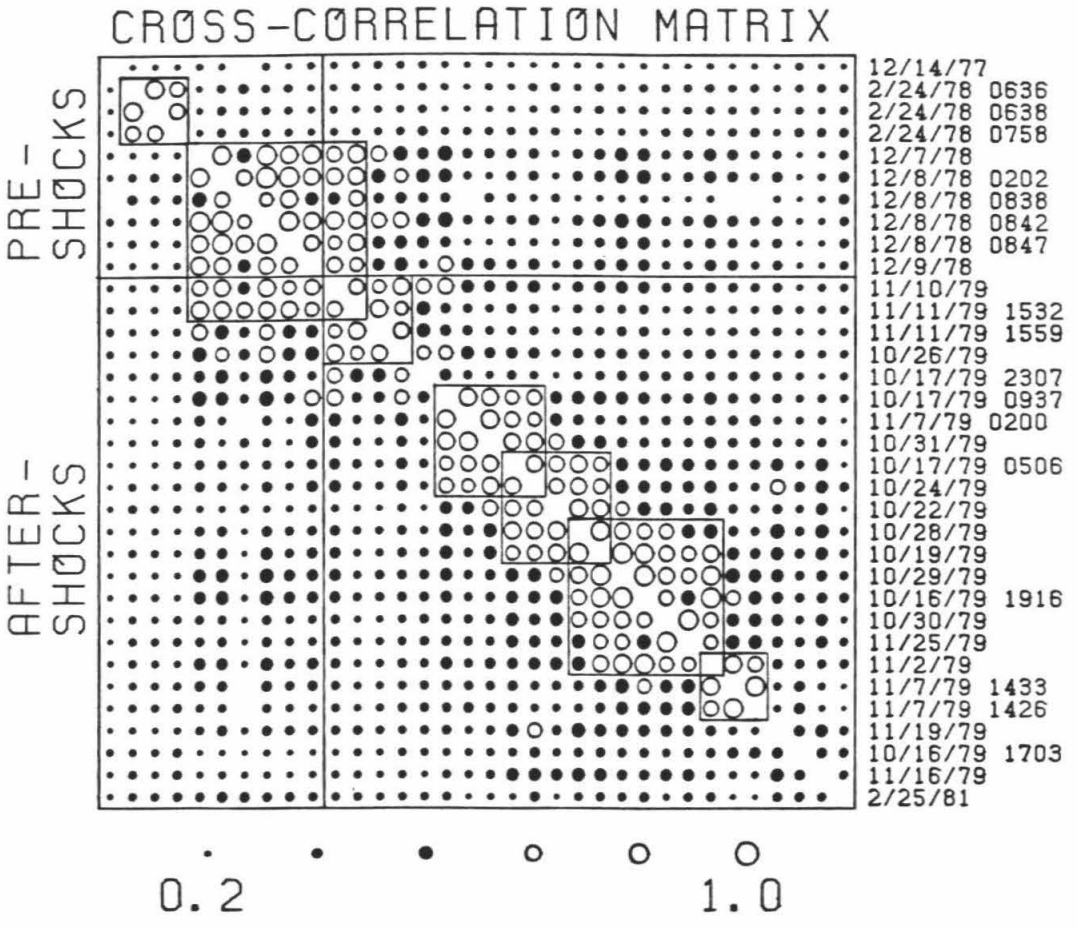

Figure 2-18. Same as Figure 2-17 except that the order of the aftershocks in the matrix has been rearranged. Boxes show one possible way to classify the events according to waveform.

swarm and the December 14, 1977, preshock (Figures 2-14 to 2-17). Sets of like events are also present within the aftershock sequence. However, after the mainshock it appears that several sources became active at once so that no more than two to three consecutive aftershocks have peak correlations >0.6.

Figure 2-18 shows the same data as Figure 2-17 except that the aftershocks are no longer chronological but have been rearranged to put similar events next to each other. This rearrangement effectively concentrates the larger circles near the diagonal. It is evident from Figure 2-18 that distinct groups of similar events exist among both the preshocks and the aftershocks, although there is some overlap between groups. The small boxes show one possible division of these earthquakes into groups. Only the preshock on December 14, 1977, and the aftershocks on October 16, 1979, 1703; November 16, 1979; and February 25, 1981, appear not to have close counterparts in this data set. At least two of the aftershocks have waveforms similar to those of the last preshocks to occur. These preshocks, the swarm on December 7-9, 1978, appear to be unique among these 34 events in terms of the number of consecutive earthquakes with similar waveforms.

The December 7-9, 1978, events are furthermore distinctive among the preshocks in that only these events have first motions consistent with the mechanism of the mainshock (Figure 2-19). The December 7-9, 1978, preshocks and about half of the aftershocks have first motions consistent with pure right-lateral strike-slip motion on a vertical fault plane striking N40°W, the approximate local strike of the Imperial

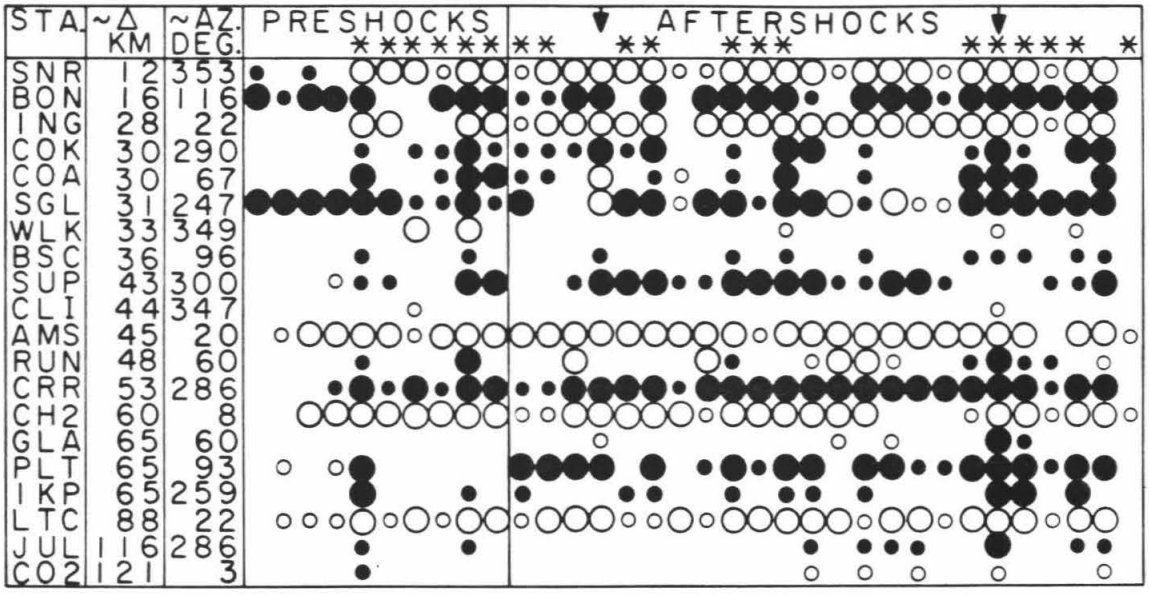

Figure 2-19. First motion readings for the events shown in Figures 2-14 and 2-15. Open and solid circles same as in Figure 2-8. Arrows indicate aftershocks for which first motion plots are shown in Figure 2-20. Asterisks indicate events for which first motions are consistent with pure right-lateral strike-slip motion on a vertical fault plane striking N40°W, the approximate local strike of the Imperial fault.

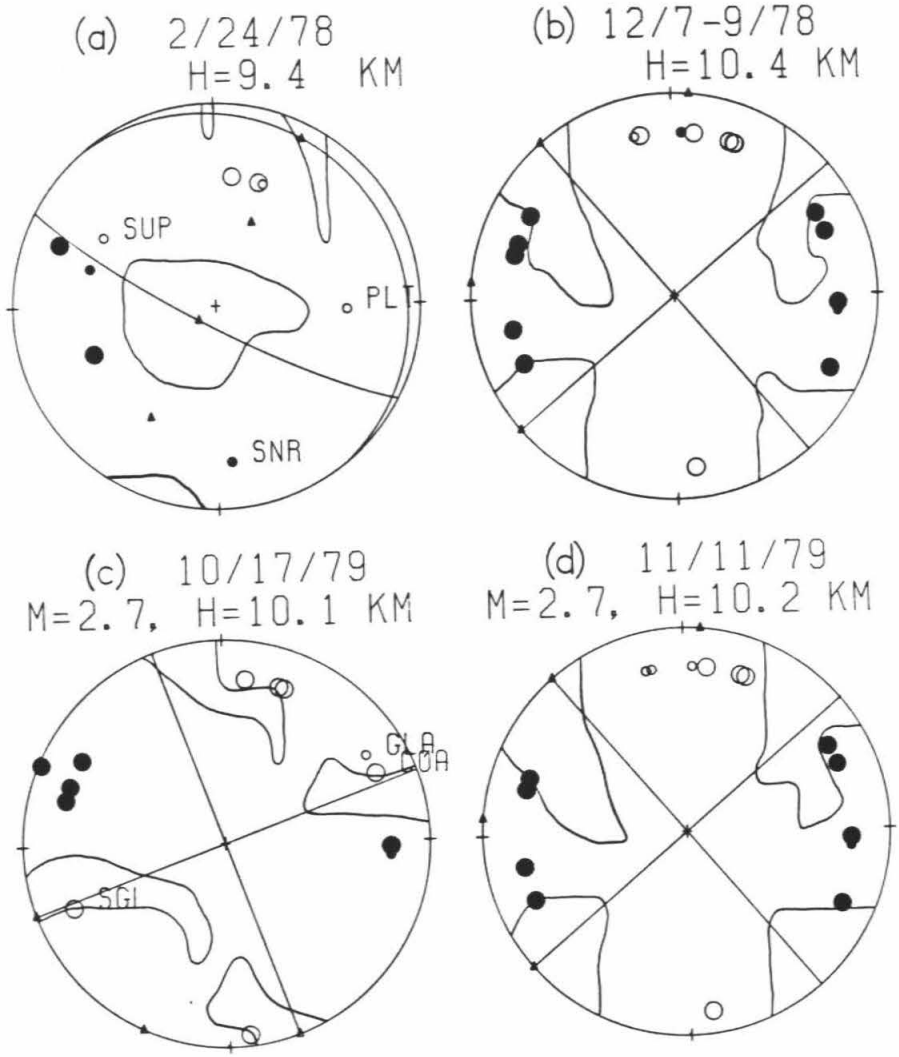

Figure 2-20. Lower hemisphere P-wave fault-plane solutions for selected preshocks and aftershocks. (a) Composite for the February 24, 1978, swarm. Hypocenter of 0638 event (Table 2-3) was used in calculating azimuths and takeoff angles. (b) Composite for the December 7-9, 1978, swarm. Hypocenter for the December 8, 1978, 0847 event (Table 2-3) was used in calculating azimuths and takeoff angles. (c) Mechanism for aftershock on October 17, 1979, 0937. (d) Mechanism for aftershock on November 11, 1979, 1532. Open and solid circles are as in Figure 2-8. Slip vectors, compression axes, and tension axes for the solutions shown are indicated by triangles. Contours enclose the locus of positions for slip vectors corresponding to solutions with the minimum number of readings in error. H is depth and M is local magnitude.

fault. These events are identified by asterisks in Figure 2-19. Figure 2-20 shows composite first motion plots for the two preshock swarms and also plots for two representative aftershocks. The contours in Figure 2-20 enclose the locus of positions for slip vectors corresponding to solutions with the minimum number of readings in error (zero for mechanisms a, c, and d and one for mechanism b). Figure 2-20d is typical of the aftershocks with asterisks in Figure 2-19 and Figure 2-20c is typical of the other aftershocks, which have different first motions at one or more of the following stations: COA, SGL, RUN, and GLA. Although the mechanism shown in Figure 2-20c, like the rest, is not well constrained, the data are consistent with right-lateral strike-slip motion on a plane deviating only about 15°-20° in strike from the average N40°W strike of the Imperial fault, as shown. It is therefore possible that all of the aftershocks in this set and the December 7-9, 1978, preshocks were associated with the main fault. On the other hand, the composite first motion plot for the February 24, 1978, swarm excludes mechanisms with shallowly-plunging slip vectors trending NW or SE. This is because of different first motions at SNR, SUP, and PLT (Figure 2-20a). Hence, these events and possibly the December 14, 1977, event may have occurred on a small nearby branch fault and not the main Imperial fault. If for this reason we exclude these preshocks from the data set, then the only preshocks remaining are the six in the December 7-9, 1978, swarm, which judging from their similarity in waveform must have occurred in a very tight cluster ($< \sim 1/2$ km).

The aftershock first motion plots (Figures 2-20c and 2-20d) suggest changes in fault strike of ~15°-20° within the region of the dashed box in Figure 2-3. No evidence for this was seen in the surface rupture (R. V. Sharp, personal communication, 1981). However, it is interesting to note that the slip model of Hartzell and Helmberger (1982) that best fits the strong motion data includes a change in fault strike from N37°W to N25°W (going north) at this point. They added this bend and others farther north to reproduce the P waveforms at the station nearest the fault. Their proposed change in fault strike fits the changes in aftershock first motions quite well except that there is no correlation between mechanism type and location within the box. This may be attributable to location error, since a comparison between waveforms and hypocenters suggests that location within the box is not well resolved by travel times.

True location appears to be the primary factor controlling the waveforms, as in the case of the events examined from near the mainshock epicenter. The classification of events by waveform in Figure 2-18 bears no relation to the magnitudes (Table 2-3). Radiation pattern may be of some importance given that waveforms from the first four preshocks do not correlate well with waveforms from later events (Figure 2-17) and that the mechanisms for these four preshocks apparently differ significantly from the others (Figures 2-19 and 2-20). However, the pattern of first motions for the rest of the events is similar, and the differences which do exist are sometimes present within groups having nearly the same waveforms at YMD, CH2, and LTC (e.g., the events on

October 19, 1979, and October 22, 1979). We therefore conclude that most families of similar events originate from small ($< \sim 1/2$ km), distinct source areas.

Spectral Analysis

Although the deconvolved records in Figures 2-5, 2-6, and 2-7 show no obvious preseismic or coseismic changes in frequency content, we decided to perform spectral analysis on them to search for more subtle changes. At least 30 sec of record is available in most cases, which makes it possible to look at frequency content of individual phases as well as for the record as a whole. The advantage of knowing the spectra for different parts of the record is that any observed changes in spectra from one event to another can be more easily interpreted. Changes in the attenuation or scattering properties of the medium are likely to affect P and S waves differently (Lockner et al., 1977), and might be especially noticeable in surface-reflected phases such as pP or sP. Frequency changes due to directivity effects would be strongly dependent on azimuth and/or takeoff angle. Changes in stress drop should cause similar frequency changes in all phases at all stations, although spectral content depends to some extent on the details of the stress release (Knopoff and Mouton, 1975).

Figure 2-21 is a record section illustrating the regional coherence of the three phases that we decided to study. Refraction studies in the Imperial Valley show several kilometers of sedimentary rocks at the surface (P-wave velocities less than 5.65 km/sec), underlain by a

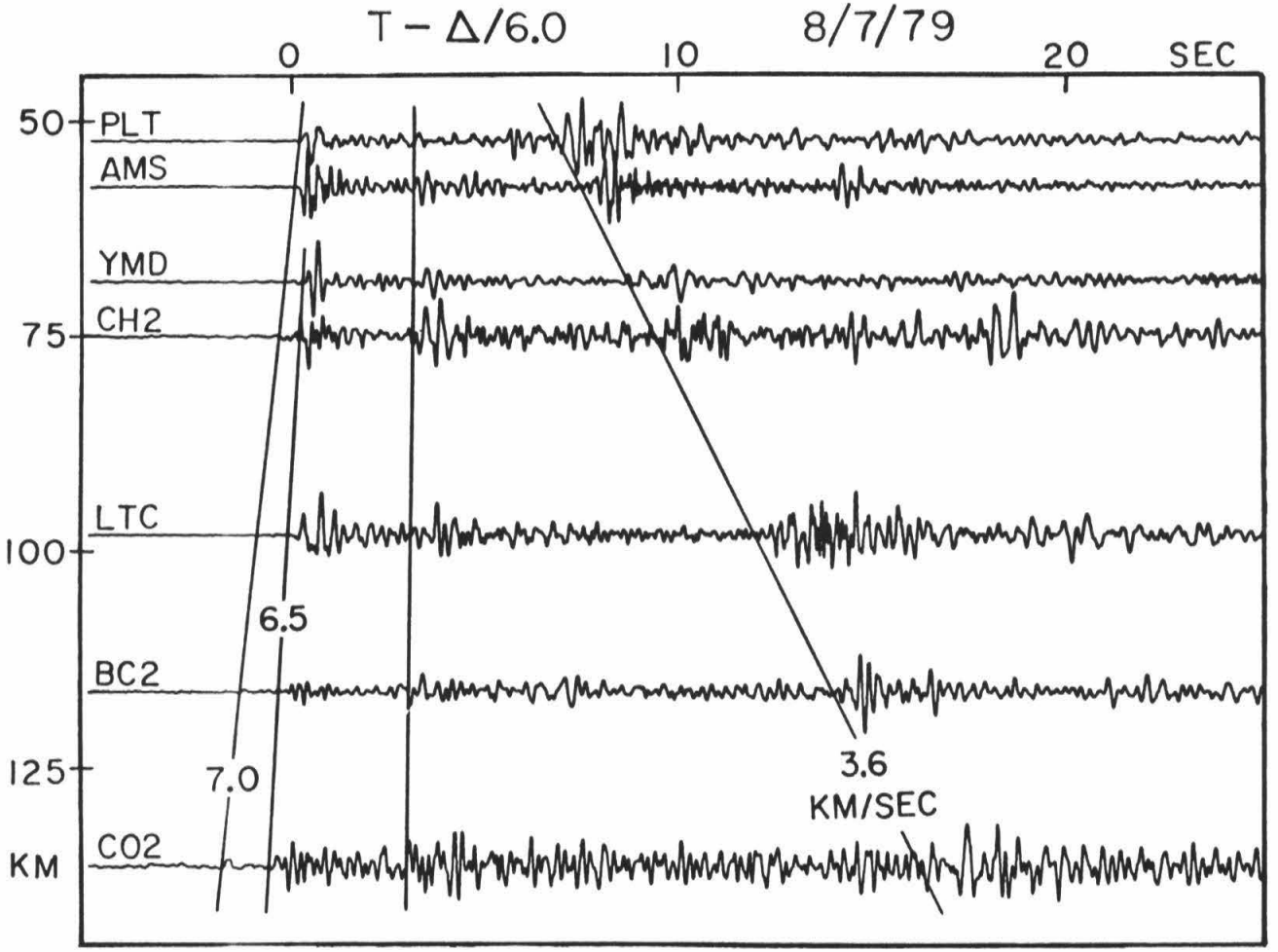

Figure 2-21. Seismograms for an M_L 2.5 preshock on August 7, 1979 (Table 2-2), recorded through modified USGS short-period vertical instruments (Archambeau, 1979).

'basement' probably composed of metasedimentary rocks (velocities of 5.65-5.85 km/sec), which in turn is underlain by a 'subbasement' (velocities greater than 6.6 km/sec) inferred to be mafic intrusive rocks (Fuis et al., 1982; McMechan and Mooney, 1980). Based on this crustal model (Table 2-1), the P phase is probably a combination of a refracted ray from the subbasement (apparent velocity 7.0 km/sec), a direct ray, and turning rays from the basement-subbasement transition. The strong phase that arrives 3 to $3^1/_2$ s later is tentatively identified as pP, but could also be sP. The phase with an apparent velocity of 3.6 km/sec is S.

We analyzed frequency content by bandpass filtering the deconvolved seismograms using third-order recursive Butterworth filters (Rader and Gold, 1967). These filters are computationally efficient approximations to ideal bandpass filters. There are two ways to estimate spectral amplitudes from filtered seismograms. Let s(t) be the seismogram of an arrival beginning at t=0 and let S(f) be its Fourier transform, where t is time and f is frequency. If s(t) is filtered with an ideal bandpass filter in the passband f_1 to f_2, the filtered seismogram $s_f(t)$ is given by

$$s_f(t) = 2\int_{f_1}^{f_2} |S(f)| \cos[\arg[S(f)] + 2\pi ft]\, df$$

Assume that $|S(f)|$ is slowly varying over the range of frequencies $f_1 \leq f \leq f_2$, such that $|S(f)| \simeq |S(f_o)|$, where $f_o=(f_1+f_2)/2$. Let $\arg(S(f))=A(f)$ and assume that A(f) can be adequately approximated by a first-order Taylor expansion about f_o:

$$A(f) \simeq A(f_o) + A'(f_o)(f-f_o)$$

With these approximations the integral becomes

$$s_f(t) \simeq 2|S(f_o)|\int_{f_1}^{f_2} \cos[2\pi ft + A(f_o) + A'(f_o)(f-f_o)]\, df$$

Evaluating this integral gives an expression for the filtered arrival:

$$s_f(t) \simeq 2|S(f_o)|(f_2-f_1)\,\frac{\sin[(f_2-f_1)(2\pi t + A'(f_o))/2]}{(f_2-f_1)(2\pi t + A'(f_o))/2}\cos[2\pi f_o t + A(f_o)]$$

Since the filtered arrival is approximately a cosine wave of amplitude $2|S(f_o)|(f_2-f_1)$, modulated by a (sin x)/x function, $|S(f_o)|$ can be estimated by measuring the maximum amplitude of the complex envelope of the filtered data (Farnbach, 1975) and then dividing by $2(f_2-f_1)$. Figure 2-22 shows a deconvolved seismogram filtered in four one-octave passbands. Since the duration of the impulse response of the filter is inversely proportional to the bandwidth (see expression above), the higher-frequency passbands give better time resolution. Thus, at high frequencies there is often more than one peak within each phase (Figure 2-22). In such cases, we simply measured the amplitude of the complex envelope of the largest one.

In order to avoid possible problems resulting from the variation in time resolution from one passband to another, we decided to make a second estimate of spectral amplitudes by measuring root mean square amplitudes within time windows 2.0 sec long for P and pP and 2.5 sec long for S (Figure 2-22). If, as before, s(t) is a seismogram and S(f) is its Fourier transform, then by Parseval's relationship (Weinberger,

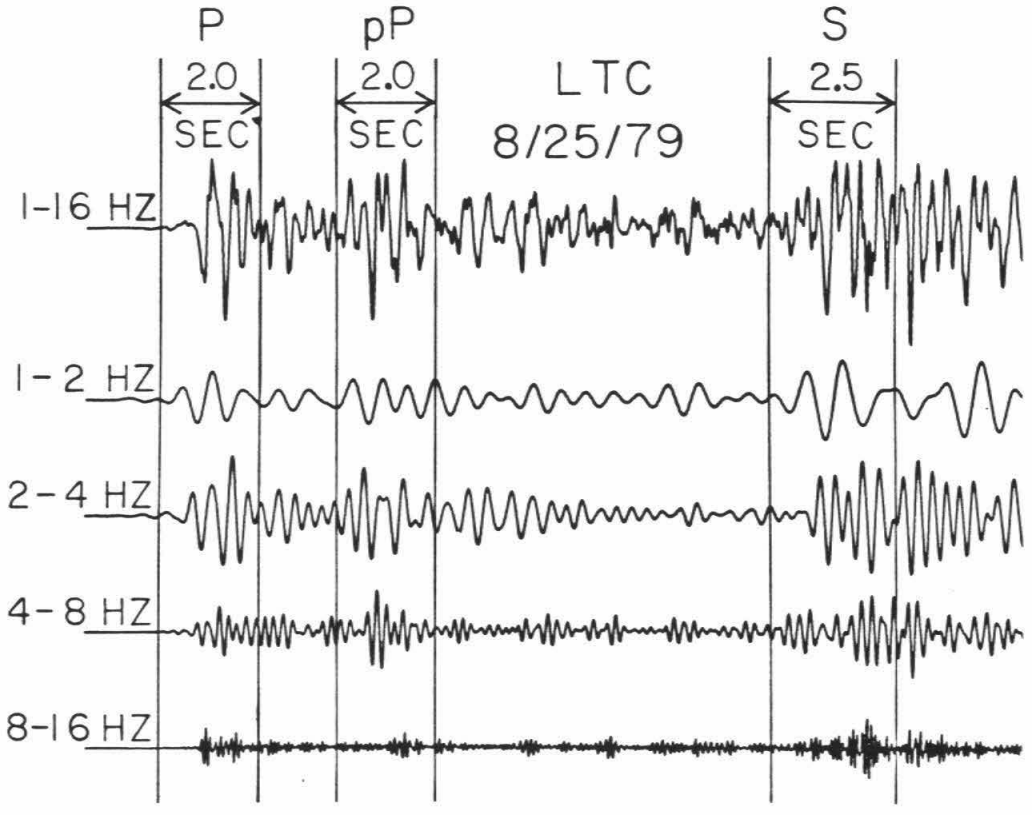

Figure 2-22. Deconvolved seismogram (top) filtered in four one-octave passbands. Time windows for spectral analysis of P, pP, and S phases are shown.

1965, p. 312)

$$\int_{-\infty}^{\infty} |S(f)|^2 \, df = \int_{-\infty}^{\infty} |s(t)|^2 \, dt$$

In the case of the filtered seismogram $s_f(t)$,

$$2\int_{f_1}^{f_2} |S(f)|^2 \, df = \int_{-\infty}^{\infty} |s_f(t)|^2 \, dt$$

If f_o is the center frequency of the passband and $S(f) \simeq S(f_o)$ for $f_1 < f < f_2$,

$$|S(f_o)| \simeq \sqrt{\frac{1}{2(f_2 - f_1)} \int_{-\infty}^{\infty} |s_f(t)|^2 \, dt}$$

For a time series of N samples separated by time ΔT,

$$|S(f_o)| \simeq \sqrt{\frac{N\Delta T}{2(f_2 - f_1)}} \sqrt{\frac{1}{N} \sum_{n=1}^{N} |s_f(n\Delta T)|^2}$$

This expression can be used to estimate $|S(f_o)|$ from the root mean square amplitude within a time window.

Figures 2-23, 2-24, and 2-25 show the results of spectral analysis of the records in Figures 2-5, 2-6, and 2-7, respectively. The plots show $|S(f_o)|$ at each station in three passbands as a function of time. These have been normalized to the amplitudes in the lowest-frequency passband used, 1-2 Hz. The crosses are the spectral amplitude ratios from the maximum envelope amplitudes, and the circles are the ratios from the root mean square amplitudes. All of the amplitudes were corrected for noise level by subtracting from each measurement an estimate of the noise amplitude taken from the 6 sec of record

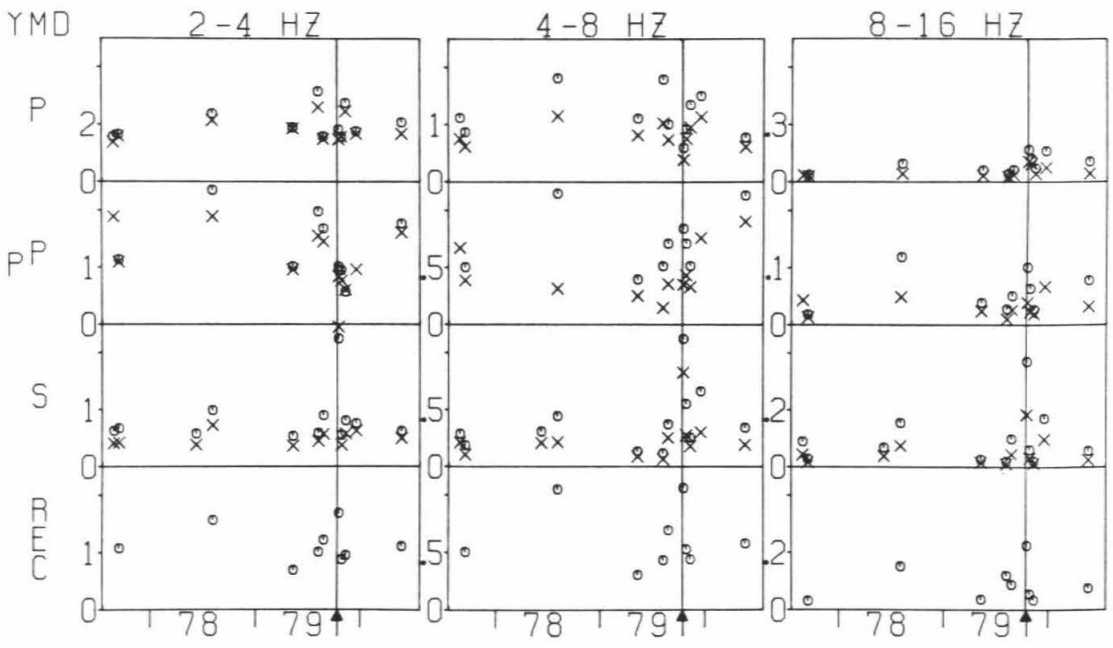

Figure 2-23. Spectral amplitudes as a function of time at station YMD for events from the dashed box in Figure 2-2. Graphs show average spectral amplitudes in the passbands 2-4, 4-8, and 8-16 Hz for the whole record (30 sec except for the December 17, 1979, event, starting with the P wave) and for the phases P, pP, and S. All have been normalized to the amplitudes in the passband 1-2 Hz. The crosses are spectral amplitude ratios from envelope amplitudes, and the circles are the ratios from root mean square amplitudes. Vertical lines indicate the time of the Imperial Valley mainshock.

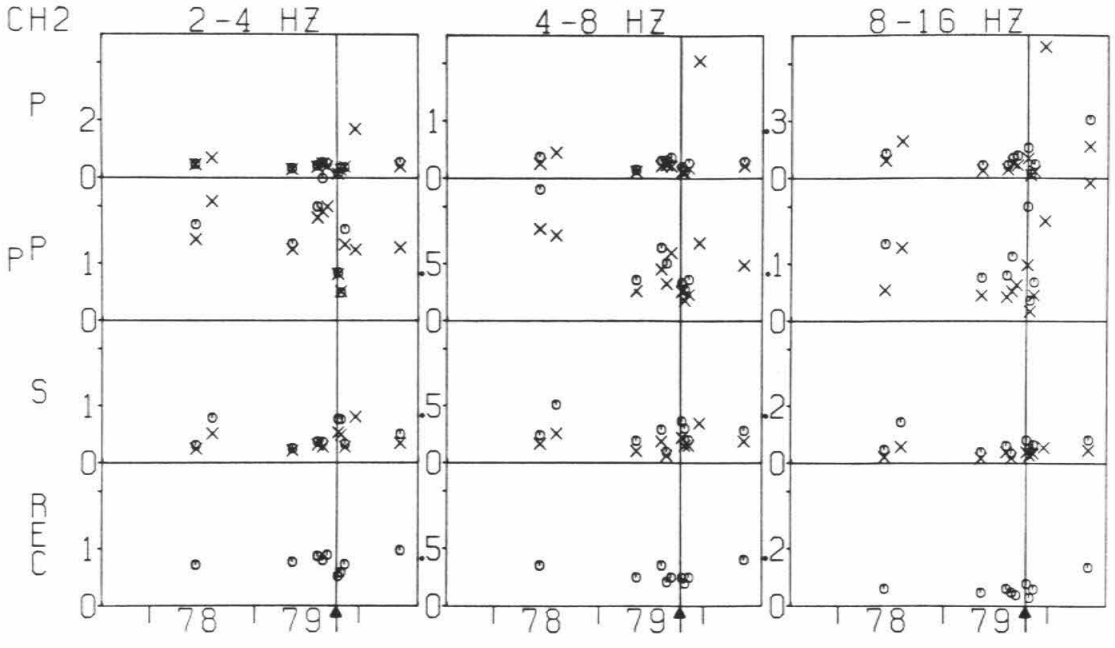

Figure 2-24. Spectral amplitudes as a function of time at station CH2 (see Figure 2-23).

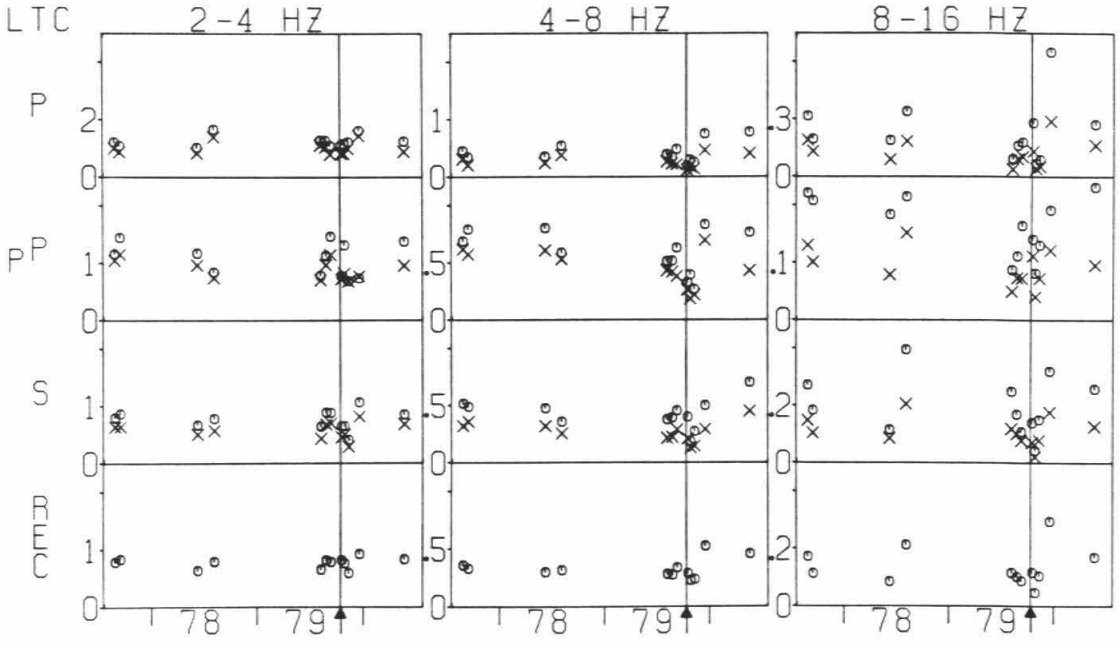

Figure 2-25. Spectral amplitudes as a function of time at station LTC (see Figure 2-23).

immediately preceding the P wave. Data for which the signal-to-noise ratio was less than three were not used. The time of the Imperial Valley mainshock is indicated by the arrows and vertical lines on the figures. The rows across correspond to P, pP, S, and the whole record (30 sec except for one event, beginning with the P wave). Although there is some scatter, all of the spectral amplitude ratios at all stations are stable with time. Thus, no temporal changes in frequency content from 1-16 Hz are observed for these records.

Several investigators (e.g., Saito and Masuda, 1981; Frankel, 1981 ; Archuleta et al., 1982) have presented evidence for a decrease in stress drop with moment for small earthquakes ($M_L < \sim 3$). These studies emphasize the importance of the relationship between event size and spectrum. This relationship is not very obvious in our data when spectral amplitude ratios are plotted versus amplitude in the lowest frequency passband used, 1-2 Hz. We therefore consider the variation in event size to be small enough so that it contributes relatively little to the scatter in Figures 2-23 to 2-25.

The seismograms of events from the second source area studied (Figures 2-14 and 2-15) show considerable variation in frequency content, with no overall temporal trends apparent. Within the December 7-9, 1978, swarm, however, seismograms of the later events appear to have more high-frequency energy than those of the earlier events. This observation is confirmed by spectral amplitude ratios for the whole record determined by the methods described above. Figure 2-26 shows these ratios as a function of event number for both preshock swarms.

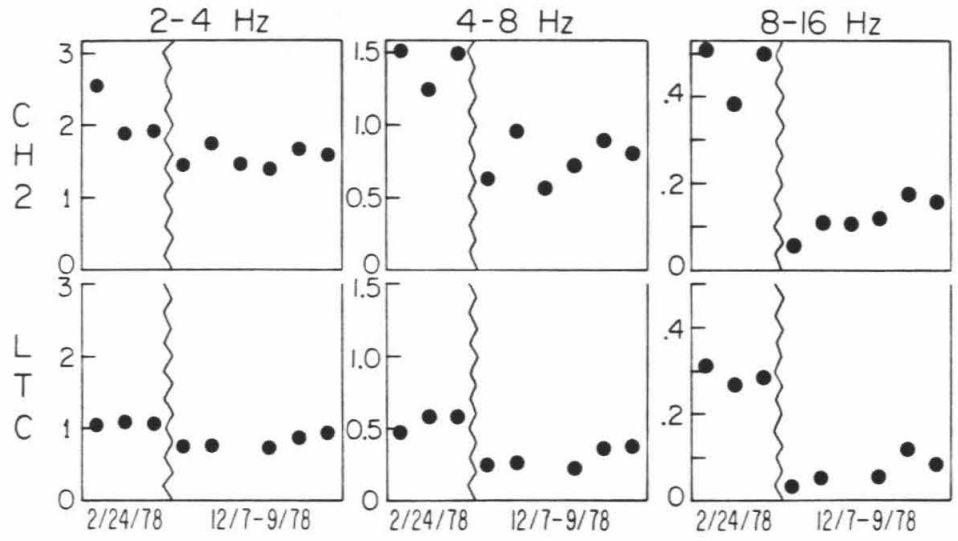

Figure 2-26. Spectral amplitudes derived from the root mean square amplitude of the whole record for preshock swarms from dashed box in Figure 2-3. These have been normalized to the amplitudes in the passband 1-2 Hz. Thirty seconds of record was used in these calculations except for the events noted in the captions for Figures 2-14 and 2-15. The effect of the instrument response has not been removed, but is the same for all records.

During the December 7-9, 1978, swarm the 8-16 Hz spectral amplitude increased relative to the 1-2 Hz spectral amplitude by about a factor of 3 at both stations CH2 and LTC. (Ratios from YMD are not shown because this station was not operating for most of the preshocks.) The other spectral ratios for this swarm are either stable with time or else show small increases (e.g., 4-8 Hz/1-2 Hz at LTC). Examination of the bandpass filtered records shows that the trends toward higher frequency with time occur over the entire record length. This suggests a systematic increase in stress drop during the December 7-9, 1978, swarm, assuming that simple kinematic source models (Aki and Richards, 1980, chapter 14) are applicable, because the variation in magnitude for these events is small and, in any case, random with time (Table 2-3). The February 24, 1978, events are clearly enriched in high frequency (4-16 Hz) relative to the December 7-9, 1978, events and show no temporal changes in spectra. These events, however, have predominantly dip-slip mechanisms (Figure 2-20a) and may not be associated with the Imperial fault, as discussed in the previous section.

In summary, there are no consistent spectral differences between preshocks and aftershocks in the frequency band 1-16 Hz. Thus, we find no evidence for coseismic changes in stress drop or apparent attenuation. During the tightly clustered preshock swarm on December 7-9, 1978, there is some indication of a systematic increase in stress drop. This was not observed for the preshock cluster near the mainshock epicenter. It appears that if there are increases in stress drop due to concentration of stress on unbroken asperities, they are not always

observable over these short time periods, even when the events have very similar mechanisms and locations within a few hundred meters. When the events are scattered over even a few kilometers, local heterogeneities in stress and velocity structure could mask this hypothesized effect if it is small. The relatively high-frequency events which preceded the 1971 San Fernando and 1952 Kern County earthquakes began about 2 years before these earthquakes (Ishida and Kanamori, 1978; 1980), so in some cases the detection of changes in average stress drop may require a longer period of observation than was available for this study.

Discussion

We find much stronger evidence to support the prediction of the asperity model regarding waveforms than the prediction about spectra. In particular, the waveform data show that the preshocks of the Imperial Valley earthquake originated from a relatively small number of highly localized sources in comparison to the aftershocks. This observation can be explained quite well by a version of the asperity model outlined in the introduction. In this model, immediately after a large earthquake the fault surface cannot slip because it is pinned at a large number of geometrical or mechanical irregularities, i.e., the asperities. Small earthquake activity is concentrated along these asperities, which decrease in number as the weaker ones fail under increasing stress. If we assume, for simplicity, that each small earthquake represents the failure of one discrete asperity, then groups of similar earthquakes represent failures of tightly clustered sets of

asperities. The larger clusters of asperities might be expected to fail last since they would be stronger than isolated asperities or smaller clusters, other things being equal. However, variations in the loading stress and in the strength and number of asperities are all likely to be important factors in determining the order in which the asperities fail. An alternative interpretation of the waveform data is that each cluster represents one asperity, and the stronger asperities which tend to be the last to fail require more events to completely fracture them. In either case when most, but not necessarily all, of the asperities have broken then the fault becomes unstable and large-scale slip can be triggered by the failure of a critical asperity, as discussed by Brune (1979), Kanamori (1981), and Das and Aki (1977).

Although we did not determine source parameters such as moment and stress drop for these events, standard scaling relations indicate that our conclusions about clustering do not imply unreasonable values for these parameters. Consider the case of the eight preshocks near the mainshock epicenter. From the similarity of waveforms we infer a maximum source separation of 200-400 m. If we assume that these events broke adjacent fault segments without significant overlap of the rupture areas, then the average rupture area per event is either $\pi(200/2)^2/8 = 3.9 \times 10^3$ m^2 or $\pi(400/2)^2/8 = 1.6 \times 10^4$ m^2, depending on which value we take for the maximum separation. This gives an estimated average rupture radius of about 35-70 m. These events have remarkably similar magnitudes, within ± 0.2 of M_L 2.4. Applying the empirical moment(M_o)-magnitude relationship of Wyss and Brune (1968) and Thatcher

and Hanks (1973),

$$\log M_o = 1.5M_L + 16.0$$

we estimate the moment of these events to be of the order of 4×10^{19} dyne-cm. The stress drop $\Delta\sigma$ for an earthquake of moment M_o on a circular fault of radius r is given by

$$\Delta\sigma = \frac{7}{16}\frac{M_o}{r^3}$$

(Eshelby, 1957; Keilis-Borok, 1959). Applying this expression, we get a stress drop for these events of approximately 50-400 bars. This is consistent with the results of Hartzell and Helmberger (1982), who estimate an overall stress drop for the mainshock of about 5-10 bars but localized stress drops of about 200 bars.

The calculated depths for both preshocks and aftershocks are concentrated within a surprisingly narrow range: 8-10 km for the southern study area (Figure 2-2, Table 2-2) and 9-11 km for the northern area (Figure 2-3, Table 2-3). Although the depths of events from south of the border may not be well constrained, the station distribution around the northern study area is reasonably favorable (Figure 2-19) and nearly all of the locations are quality B, which implies vertical errors of less than 5 km (Lee and Lahr, 1975; Lee et al., 1979). Furthermore, the depths of several nearby aftershocks determined by P. German (personal communication, 1982) with the aid of arrival times from both temporary and permanent stations are all between 8 and 9 km. These depths agree very well with those in Table 2-3.

The depths of the preshocks and aftershocks may give some clue as

to the nature of the assumed asperities or the distribution of stress. In both areas studied the events are concentrated within the lowermost few kilometers of the basement, which appears to be composed of metamorphosed sedimentary rock. The boundary between the basement and the subbasement, inferred to be mafic intrusive rock, dips about 4°NW along the axis of the Salton Trough (Fuis et al., 1982; McMechan and Mooney, 1980). One speculative hypothesis is that the asperities are related to irregularities in the basement-subbasement transition zone, which is being offset by the Imperial fault. Another possibility is that the asperities are evenly distributed and the concentration of activity near 10 km is due to a concentration of stress near the depth of the transition from brittle to ductile deformation. This transition is believed to occur near 10 km because this is the approximate depth of the seismic zone in the southern Imperial Valley and also the approximate depth to which faulting during the 1979 Imperial Valley earthquake extended (Hartzell and Helmberger, 1982). Stresses could be higher near this boundary if basal shear is important as a driving or resistive force. A third possibility is that the 1940 earthquake relieved most of the stress across the upper part of the fault in the regions studied. This would be consistent with the concentration of slip below 5 km in the model of Hartzell and Helmberger (1982) and also the lack of surface faulting near the 1979 epicenter. A more comprehensive study of the depth distribution of earthquakes along the Imperial fault might help to resolve some of these questions.

There is a significant difference between the temporal distribution

of the preshocks that we studied near the mainshock epicenter and those 10-12 km north of the border. The preshocks in the southern study area were spread out more or less uniformly over the time period examined, 1977-1979 (Table 2-2). In contrast, all of the preshocks in the northern study area with strike-slip mechanisms occurred during a 3-day swarm. In the context of the one asperity/ one earthquake model described above, these observations suggest that the asperities in the northern study area were comparatively weak, because the failure of one asperity apparently triggered the rapid failure of several others close by. The much larger number of aftershocks in the northern study area could also be explained by a tendency toward weaker and/or more numerous asperities there, but may also reflect a deficiency of coseismic slip along that section of fault as suggested by Hartzell and Helmberger (1982).

Although we favor the asperity model as an explanation for the waveform data, there are other models that can account for the change in waveform similarity at the time of the mainshock. Our model is crucially dependent on the assumption that the preshocks and the aftershocks we studied represent slip along the main fault. However, there is evidence that much of the small earthquake activity along the seismogenic zone linking the Imperial fault to the southern end of the San Andreas fault is associated with structures transverse to the trend of this zone and to the Imperial and Brawley faults (Figure 2-1) (Johnson and Hadley, 1976; Johnson, 1979; Johnson and Hutton, 1982; Hutton and Johnson, 1981). Earthquake swarms along these transverse

structures may be activated by creep events on connecting faults (Johnson and Hadley, 1976; Johnson, 1979). If these transverse structures also exist along the central portion of the Imperial fault where our study areas are, then some or all of the preshocks and aftershocks could be associated with them. C. Johnson (personal communication, 1982) has suggested that the greater variety of aftershock waveforms could be explained by the simultaneous activation of many different transverse structures by the coseismic and postseismic movement along the Imperial fault. Since our study areas are only a few kilometers long, this hypothesis requires a much higher density of transverse features than can be inferred to exist from the pattern of epicenters in the seismogenic zone to the north.

To help resolve which model best explains the difference between Imperial Valley preshocks and aftershocks, it is important to determine whether normal 'background' seismic activity is more like the aftershocks or the preshocks we studied. Some models, such as Johnson's, suggest that the diversity of small earthquake waveforms after the mainshock is temporary and that background seismicity and preshocks are both characterized by small-scale spatial clustering of successive events. The asperity model predicts in most cases a more gradual change from one waveform pattern to the other during the intervals between large earthquakes. Unfortunately, only a few studies of comparative waveform have been done, and these generally cover short periods of time. One of the more long-term data sets is that of Ishida and Kanamori (1978), who collected Wood-Anderson seismograms recorded at

Pasadena for all $M_L<3$ events which occurred within 15 km of the epicenter of the 1971 San Fernando earthquake ($\Delta\sim40$ km) during the period 1961-1971. Master event locations for this region show diffuse seismicity from 1961-1964, quiescence from 1965-1968, and clustering near the eventual hypocenter from 1969-1970. This pattern was confirmed by visual inspection of the waveforms, although Ishida and Kanamori note that it is much more obvious on the EW component than on the NS component. We applied our cross-correlation tests to the hand-digitized records of Ishida and Kanamori. The results are shown in Figures 2-27 and 2-28. Because of digitization noise and because only ~9-11 sec of record had a large enough amplitude to be digitized in most cases, these cross correlations are not as reliable as those performed with CEDAR data. Nevertheless, Figures 2-27 and 2-28 confirm the observations of Ishida and Kanamori that the events during 1961-1964 exhibit a greater variety of waveforms than those during 1969-1970, at least on the EW component. On the EW records, the last four events before the mainshock have very high peak correlations (~0.75), as do the first three events in 1961. Peak correlations between EW seismograms of other pairs of consecutive events are all less than 0.6 (Figure 2-27). The averages of the NS and EW maximum cross correlations for most of the event pairs are less than 0.6, except for average peak correlations among the last four events, the first three events, and events three through five (Figure 2-28). These results suggest that tight clustering of hypocenters of consecutive events does not occur very often, even if such clustering is not limited to the time period immediately before large earthquakes.

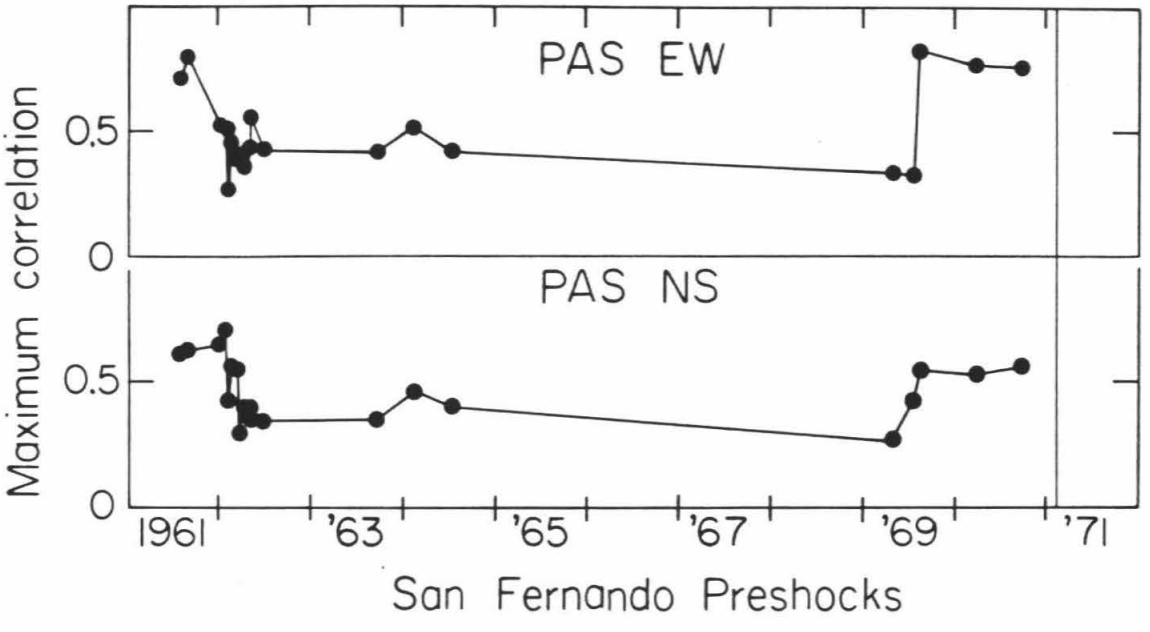

Figure 2-27. Maximum cross correlation between seismograms of consecutive events within a 15-km radius of the epicenter of the 1971 San Fernando earthquake, plotted as a function of time. Seismograms are shown in Figs. 2 and 3 of Ishida and Kanamori (1978). 9-11 sec of record were used in most cases, beginning with the S wave. Seismograms were recorded on Wood-Anderson torsion instruments located at Pasadena (Δ~40 km).

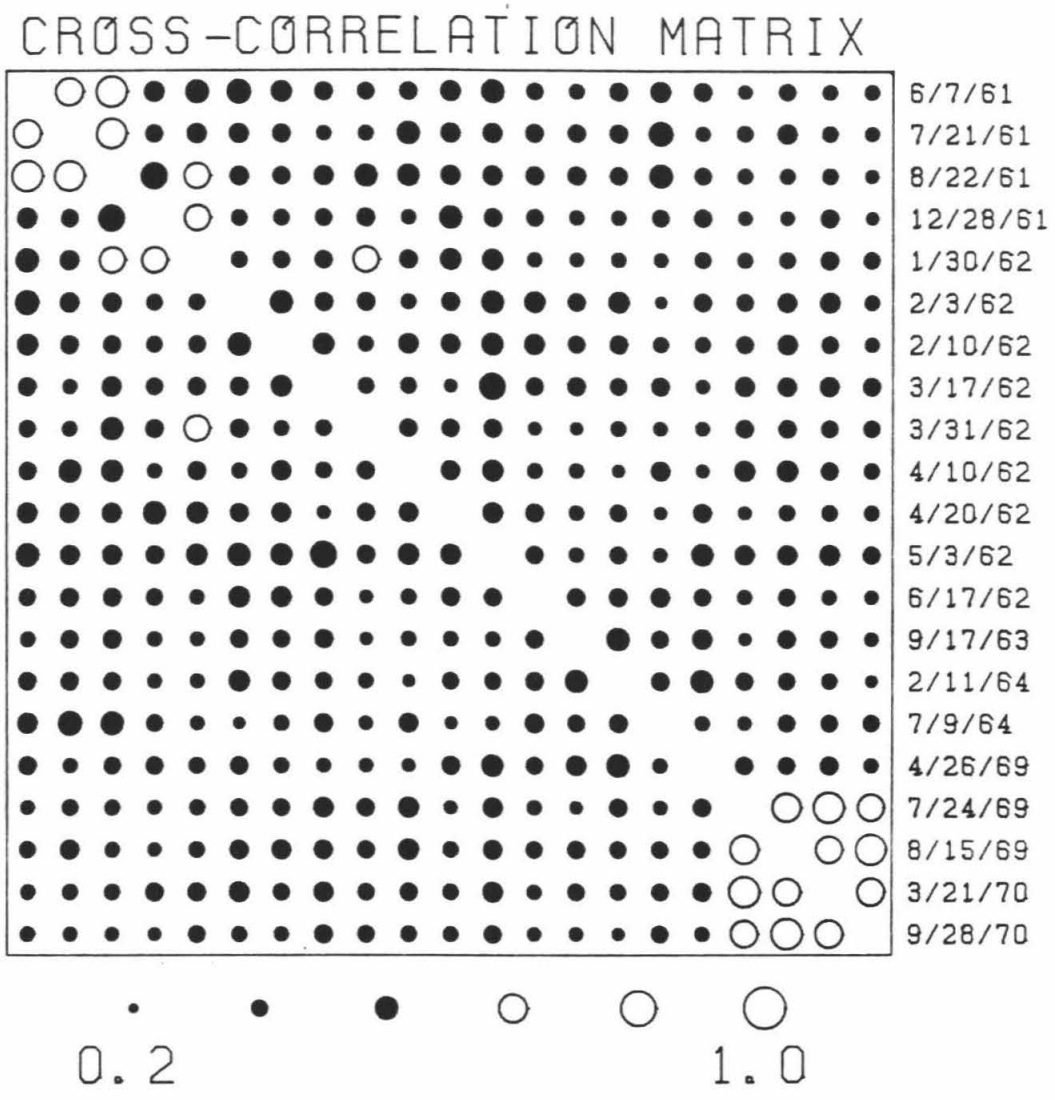

Figure 2-28. Complete cross-correlation matrix for events within 15 km of the epicenter of the 1971 San Fernando earthquake. Each circle represents an average of the peak cross correlations determined from the EW and NS Wood-Anderson seismograms recorded at Pasadena (Δ~40 km). See Figure 2-10 for explanation.

Hence, comparison of waveforms may be a useful tool for monitoring stress conditions along faults.

Conclusions

In summary, we find that preshocks of the 1979 Imperial Valley earthquake occurred in groups of events with strikingly similar waveforms over the entire length of record. The close match in waveform implies similar source mechanisms and clustering of hypocenters within $^1/_4$ wavelength ($\sim^1/_2$ km) or less. Aftershock waveforms are more variable from one event to the next, although groups of similar events were found during the aftershock period as well. These observations can be explained by the asperity model, which predicts localization of failure on strong, unbroken asperities along the fault during the period preceding moderate to large earthquakes. From our work and that of Ishida and Kanamori (1978) on the 1971 San Fernando earthquake, it appears that this period of enhanced clustering is at least 2-3 years long, but much more work needs to be done to evaluate the significance of this pattern. A second prediction of the asperity model, that of higher stress drop for preshocks, was not in general supported by our data. We did find evidence for increasing stress drop within a tightly grouped set of six preshocks from near the region of maximum surface displacement. However, the frequency content of these events does not differ significantly from that of nearby aftershocks, and no systematic temporal changes in spectra were found for the other preshock cluster we analyzed. It appears that the waveforms of small earthquakes are a more

sensitive indicator of seismic potential than are the spectra.

CHAPTER 3

A Preliminary Study of Waveforms of Small Earthquakes Along the San Jacinto Fault Zone, California

Introduction

Chapter 2 presented evidence that the seismicity for at least two years preceding the 1971 San Fernando earthquake and the 1979 Imperial Valley earthquake was characterized by clustering within source volumes less than 1/2 km in extent. This type of clustering, deduced from waveform similarity, was also observed after the Imperial Valley earthquake in one region studied, although compared to the pre-earthquake period many more sources were active simultaneously. In light of these results, it is clearly of interest to establish to what extent this behavior is typical of 'background' seismic activity. A cross-correlation analysis of ten years of waveform data from the San Fernando region, discussed in the last chapter, suggests that tight clustering of hypocenters is not very common. However, this analysis and some published waveform data (see introduction to Chapter 2) show that not all groups of earthquakes with similar waveforms are closely associated in time with major earthquakes. In order to determine how prevalent this clustering phenomenon is, it is necessary to systematically search for earthquakes with similar waveforms within many different small regions using some objective method such as the cross-correlation matrix technique developed in Chapter 2. Towards this

goal, we have determined cross-correlation matrices for small earthquakes within two different regions along the San Jacinto fault zone in southern California. This chapter reports the results of this study and a parallel study of focal mechanisms for the same events.

The San Jacinto fault zone consists of several en echelon strands along which significant Cenozoic right-lateral displacements have taken place (Sharp, 1967, 1975). In terms of numbers of earthquakes, both large and small, it is one of the most seismically active fault zones in southern California. Since 1890 at least six and as many as ten earthquakes greater than magnitude six were associated with faults in this zone (Sanders and Kanamori, 1983). On current seismicity maps of southern California, it is one of the few active fault zones which is delineated by a concentration of small earthquake activity (Allen, 1981), although in detail it is not easy to assign earthquakes to particular faults within the zone. The most outstanding feature of the distribution of seismicity along this zone is a 22 km long quiescent section near the town of Anza (Figure 3-1, SE of station KEE), bounded to the northwest and southeast by regions of exceptionally high activity. The quiescent section approximately coincides with one of two segments of the fault zone that Thatcher et al. (1975) concluded were deficient in slip based on a study of large, historic earthquakes. Thus, the segment of the fault zone near Anza appears to be a seismic gap in both senses in which this term is used, and is known as the Anza seismic gap.

Because different segments of the San Jacinto fault zone have

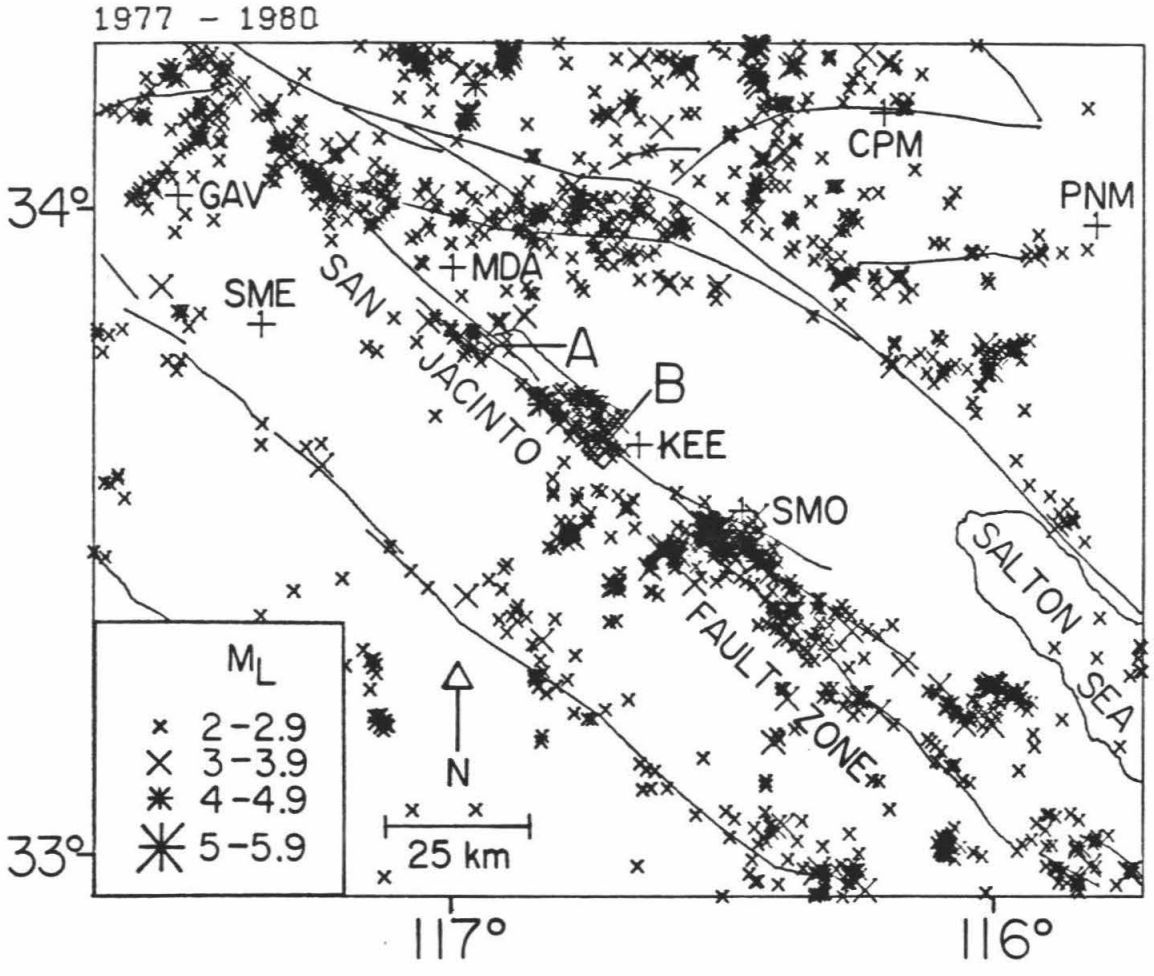

Figure 3-1. Map of San Jacinto fault zone and surrounding area showing epicenters of all $M_L \geq 2.0$ earthquakes from the Caltech/ U.S. Geological Survey catalog for the period 1977 to 1980. The +'s mark locations of seismographic stations used in waveform studies of earthquakes in regions A and B. Faults are generalized from Jennings et al. (1975). The northwest-striking faults southwest and northeast of the San Jacinto fault zone are the Elsinore and San Andreas faults, respectively.

ruptured at various different times since 1890, and other segments do not appear to have slipped at all during this time, this fault zone presents a good opportunity to study different stages of the seismic cycle within the limitations of a short data set such as CEDAR. For this reason, and because of the abundance of small earthquake activity in close spatial association with the major faults in this zone, the San Jacinto fault zone is a particularly good place for waveform cross-correlation studies. We consider this study to be preliminary because only two small (<5 km) regions northwest of the Anza gap were examined. Very little evidence for small-scale clustering was found within these regions for the period 1977-1980. Wood-Anderson seismograms of earthquakes during 1934-1980 in a 12 by 18 km region southeast of the gap look quite similar (H. Kanamori, personal communication, 1980), but a more quantitative analysis in this region using CEDAR data is desirable.

Waveform Analysis

Figure 3-1 shows epicenters from the Caltech/ U. S. Geological Survey catalog for all earthquakes of magnitude 2 and greater during 1977-1980 within the San Jacinto fault zone and the surrounding region. Digitally-recorded seismograms are available for all of these earthquakes and for more recent ones, but the more recent data are not easily accessible at present. A recurrence plot for earthquakes in this region suggests that the catalog coverage is complete for earthquakes of $M_L \geq 2$, in agreement with the uniform detection threshold estimated by

Johnson (1979) for this area. Although the catalog is still preliminary for some of this time period, the epicenters in this area are sufficiently well determined (< 5 km standard error) that it was not necessary to relocate them before selecting groups of events for waveform comparisons.

The two regions selected for study, designated A and B, are shown in Figures 3-1 and 3-2. All $M_L \geq 2$ events in these regions were included in the study, except for one earthquake from region B which could not be used because it was a double event. The largest events are magnitude 3. There are six events in region A, which is a 3 by 5 km box located near the epicenters of two large historic earthquakes which occurred in 1899 (M 7) and 1918 (M 6.8) (Richter, 1958, p. 496; Sanders and Kanamori, 1983). Nine usable events are included in region B, a 4 by 4 km box at the northwest edge of the Anza seismic gap. As a check on the accuracy of the epicenters, the $M_L \geq 2$ events in regions A and B were relocated using the master event technique of Johnson and Hadley (1976) with the computer program HYP071 (Lee and Lahr, 1975) (Table 3-1). The standard southern California velocity model (Figure 3-9) based on Hadley and Kanamori (1977) was employed. Only stations within 60 km of the epicenter were used in order to maximize the depth resolution. This still left at least 9 stations available for each location. The changes in horizontal location were all small, less than 1 1/2 km (Figure 3-2), but as expected some of the revised depths were significantly different. Most, but not all, of the revised depths are between 12 and 16 km (Table 3-1), which is relatively deep for

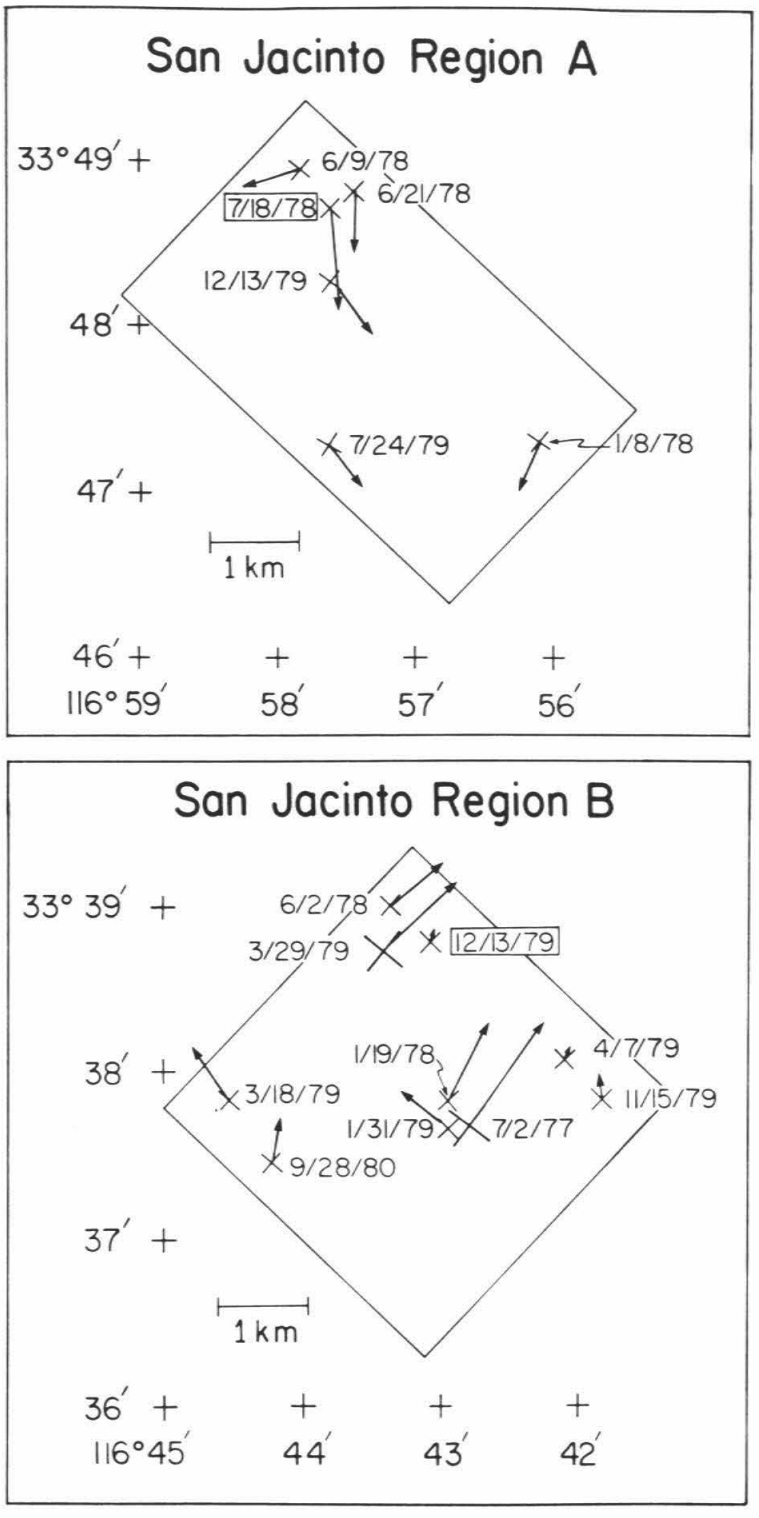

Figure 3-2. Epicenters of earthquakes in regions A and B (Figure 3-1). The X's show the catalog epicenters. Arrows point to relocated epicenters. Small X's are events of $2.0 \leq M_L < 3.0$ and large X's are $M_L \geq 3.0$ events. The boxed events are those used as master events in the relocations.

TABLE 3-1. Relocated Hypocenters in San Jacinto Study Areas

Date	Time	Latitude	Longitude	Depth,km	M_L	
		Region A				
Jan. 8, 1978	0839:54.56	33°47.05′	116°56.23′	8.0	2.0	
June 9, 1978	2247:06.33	33°48.86′	116°58.27′	14.7	2.1	
June 21, 1978	1126:29.60	33°48.49′	116°57.46′	14.0	2.2	
July 18, 1978	0229:59.41	33°48.16′	116°57.56′	14.0	2.5	+
July 24, 1979	1020:49.54	33°47.03′	116°57.39′	14.0	2.7	
Dec. 13, 1979	2207:28.92	33°47.95′	116°57.31′	6.0	2.2	
		Region B				
July 2, 1977	0122:37.67	33°38.27′	116°42.28′	13.6	3.0	
Jan. 19, 1978	0055:30.81	33°38.26′	116°42.67′	12.3	2.2	
June 2, 1978	0331:18.32	33°39.28′	116°42.96′	15.1	2.1	
Jan. 31, 1979	1825:05.07	33°37.90′	116°43.27′	15.6	2.0	
Mar. 18, 1979	1347:59.46	33°38.11′	116°44.76′	15.8	2.2	
Mar. 29, 1979	0217:11.24	33°39.14′	116°42.88′	15.9	3.0	
Apr. 7, 1979	1636:02.29	33°38.12′	116°42.07′	14.1	2.6	*
Nov. 15, 1979	0008:48.21	33°38.00′	116°41.84′	13.1	2.0	
Dec. 13, 1979	2105:10.90	33°38.83′	116°43.04′	14.1	2.1	+
Sep. 28, 1980	1727:27.39	33°37.67′	116°44.17′	2.5	2.7	

\+ Master event
* Unusable (multiple event)

earthquakes in southern California.

The choice of the recording stations for waveform comparison was determined entirely by the availability of on-scale high signal-to-noise records for the events of interest. After examining all of the data to see which seismograms were usable, stations MDA, KEE, SMO, GAV, and PNM were selected for study of the events in region A, and stations SMO, SME, CPM, and PNM were selected for study of the events in region B (Figure 3-1). Seismograms from the 1977 and 1978 events were filtered with a digital filter designed to correct for changes in instrumentation implemented at all of these stations in late 1978 (see Chapter 2). In addition, all of the seismograms from stations SMO and CPM were filtered with a highpass Butterworth filter with a corner at 1 Hz to remove long-period (3 sec and greater) electronic noise present on some records.

The corrected seismograms from regions A and B are shown in Figures 3-3 and 3-4, respectively. It is evident from these figures that there are large variations in frequency content from one station to another. Seismograms in Figure 3-4 of events from region B become longer period with increasing distance from the source, as is expected if regional scattering and attenuation is controlling the changes in frequency content. However, the frequency content of seismograms of events in region A (Figure 3-3) does not correlate with source-receiver distance. In particular, seismograms from stations SMO and GAV are much higher frequency than those recorded at stations MDA and KEE, which are closer to the source region. There is no obvious connection between frequency

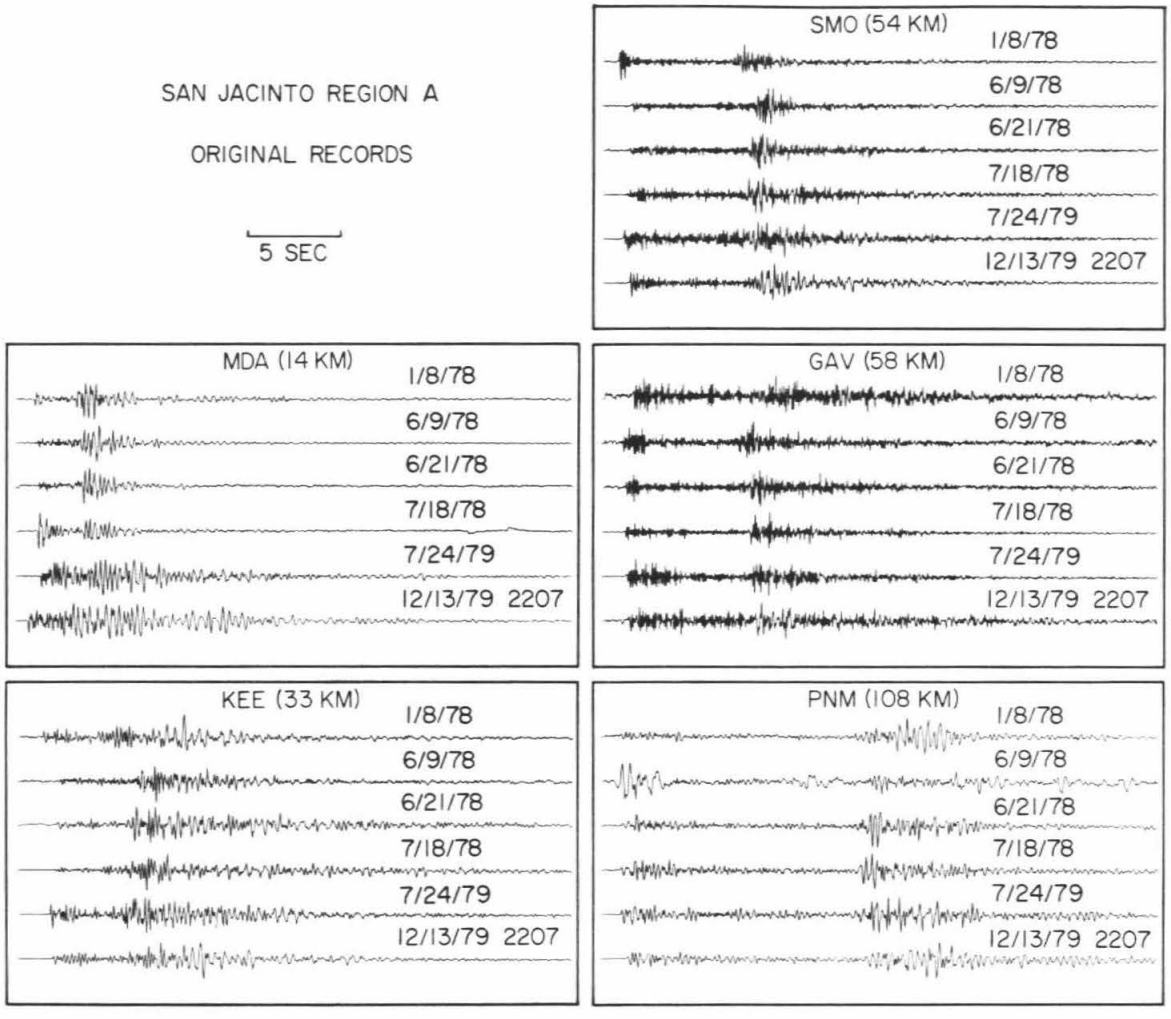

Figure 3-3. Vertical component seismograms of earthquakes in region A. These are the original records except for filtering to normalize instrument responses and remove long-period noise at some stations (see text). Seismograms are plotted with the same maximum amplitude and positioned horizontally within each box according to the catalog origin times.

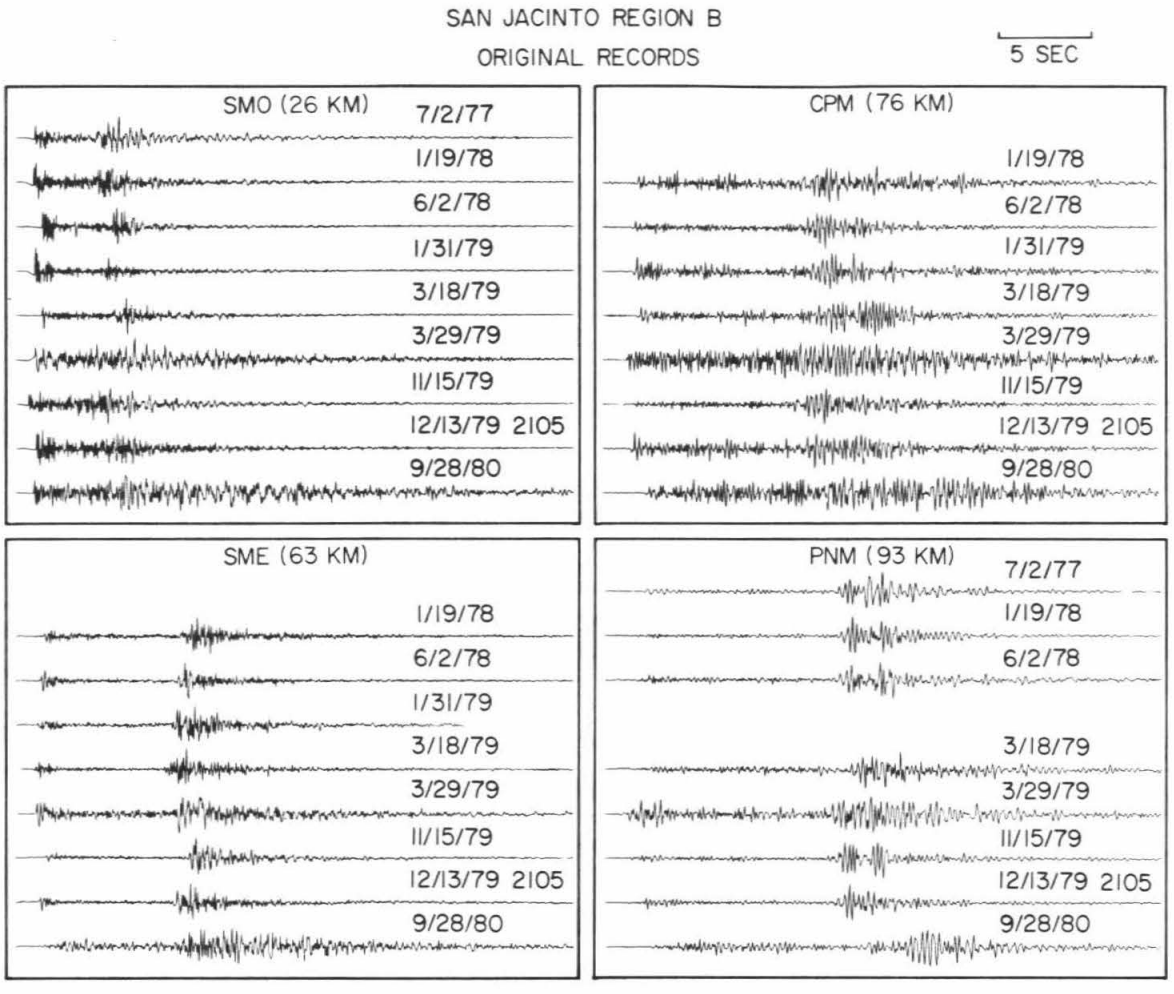

Figure 3-4. Vertical component seismograms of earthquakes in region B. See Figure 3-3 for explanation.

content and receiver azimuth or surface geology. For instance, stations KEE and SMO lie at nearly the same azimuth from region A, and both are on the northeast side of the San Jacinto fault zone on the same type of material, decomposed granitic rock. Yet, the records from station KEE at a distance of about 33 km have dominant frequencies of ~6-9 Hz whereas those from SMO at a distance of about 54 km typically have dominant frequencies of ~12-15 Hz. All seven stations used in this study have the same instrumentation except for the amplifiers, which are not important in determining the frequency response. Problems with the instrumentation cannot be ruled out without individually calibrating each station. It is possible, however, that the spectra of these seismograms are controlled by site response, as was determined by Frankel (1982b) for small earthquakes in the northeastern Caribbean. The problem of site response is discussed further in Chapter 4.

From inspection of the records in Figures 3-3 and 3-4, it appears that there are no groups of events in either study area that have similar waveforms at all of the recording stations. Because some of these seismograms have much more high frequency (>6 Hz) energy than those used for the Imperial Valley and San Fernando waveform studies (Chapter 2), we decided to compare filtered records to see if there might be more similarity at the longer periods. The passband chosen for the filter, 1-4 Hz, was the passband within which filtered seismograms of Imperial Valley preshocks near the mainshock epicenter were all nearly alike (Figure 2-13). After filtering, the seismograms still show considerable variety in waveform at each station (Figures 3-5 and 3-6).

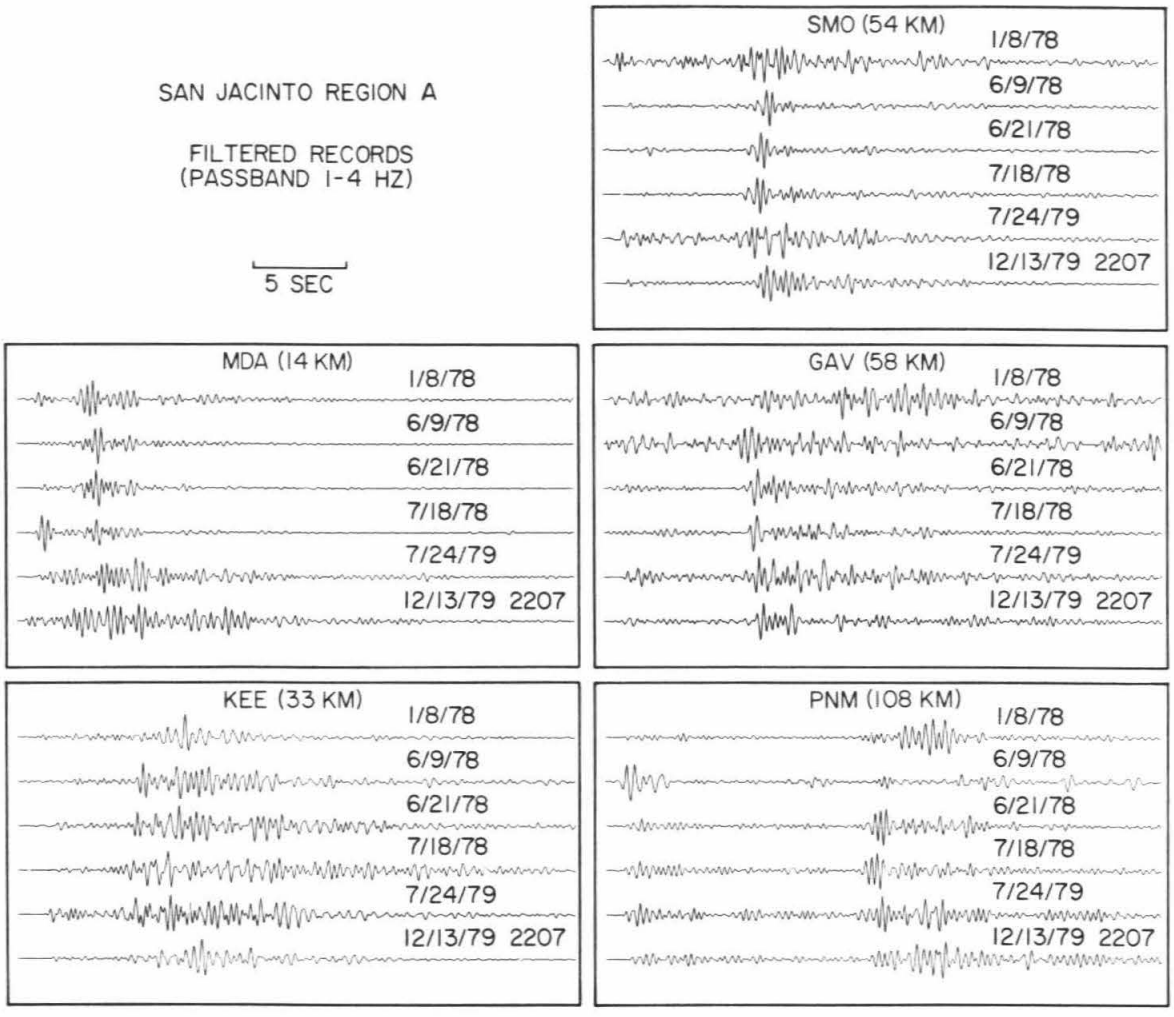

Figure 3-5. Filtered versions of seismograms in Figure 3-3. The filter used was a third-order phaseless Butterworth filter with a passband of 1-4 Hz.

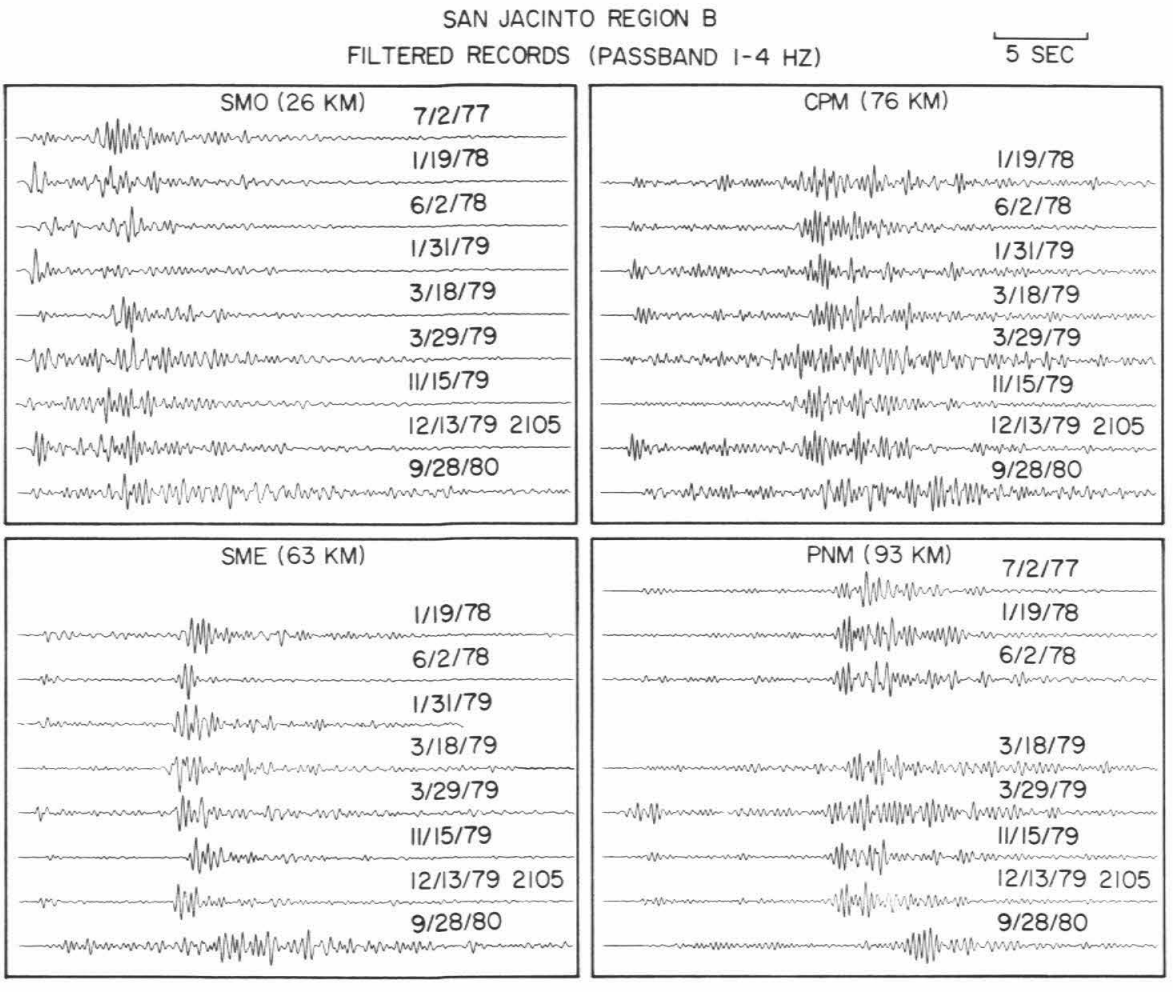

Figure 3-6. Filtered versions of seismograms in Figure 3-4.

Although there are groups of events having similar waveforms at some stations, these same events have very different waveforms at other stations. For example, the events in region A on June 9, 1978, June 21, 1978, and July 18, 1978, produced very similar 1-4 Hz waveforms at station SMO. The 1-4 Hz waveforms for the first two of these events are similar at MDA and KEE, but not at the other stations. These observations suggest that some of the differences in waveform are due to differences in focal mechanism. The first motion study presented in the next section confirms that there are differences in mechanism among these events. The seismograms in Figures 3-3 to 3-6 show that it is clearly desirable to use more than 1 or 2 stations in studies of waveform similarity.

Figure 3-7 shows complete cross-correlation matrices for regions A and B constructed from both unfiltered (left) and filtered (right) seismograms. Each correlation coefficient shown represents the mean of the values obtained for the different stations. Not surprisingly, the correlation coefficients derived from the filtered records are larger than those obtained from the unfiltered records. Nevertheless, there is very little evidence for repeated events with nearly the same location and mechanism, such as was observed before the 1971 San Fernando and 1979 Imperial Valley earthquakes. Figure 3-8 compares waveform cross-correlation matrices from this chapter and Chapter 2 for different small regions in southern California. It appears from this figure that the occurrence of consecutive small earthquakes with similar waveforms which preceded the Imperial Valley and San Fernando earthquakes was

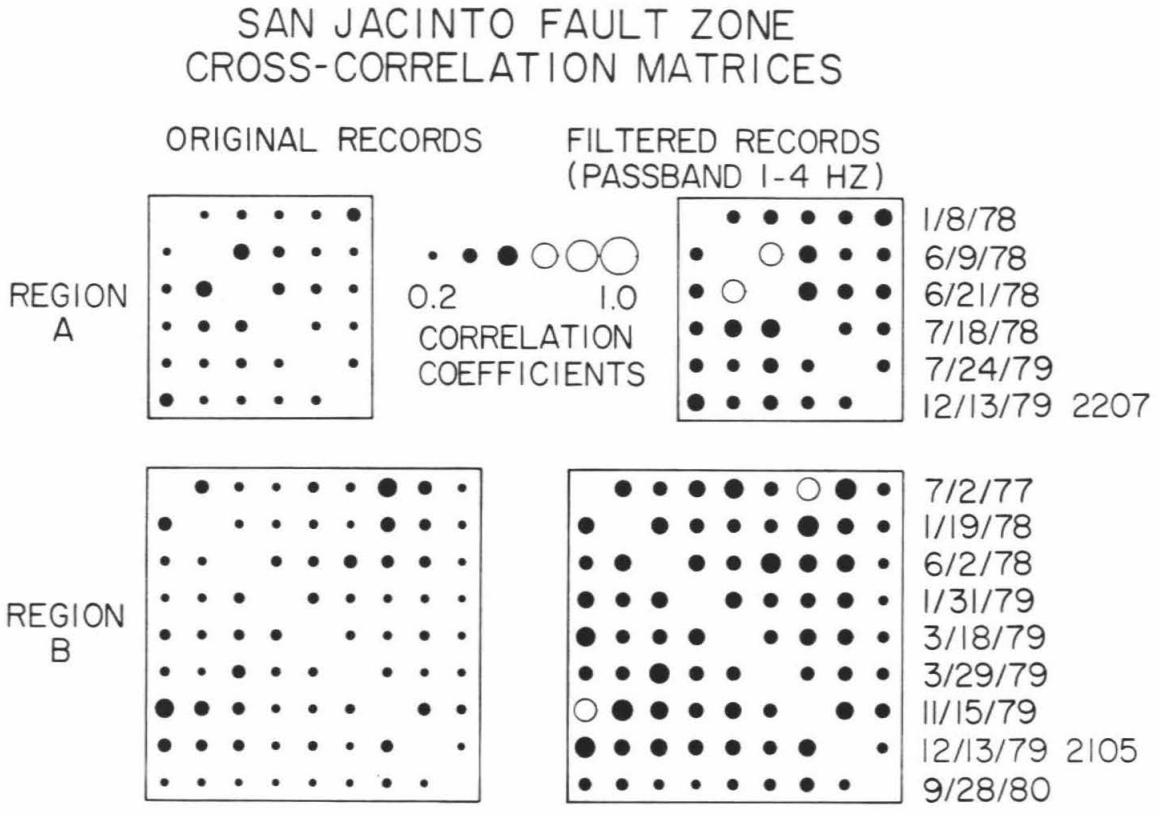

Figure 3-7. Cross-correlation matrices for filtered and unfiltered seismograms of earthquakes in regions A and B. Each circle represents the mean peak cross correlation for the event pair corresponding to its position in the matrix. The radius of the circle is proportional to the correlation value, and circles representing values less than 0.6 are solid. Peak cross-correlation values from stations MDA, KEE, SMO, GAV, and PNM were averaged to obtain the matrix elements for region A and values from stations SMO, SME, CPM, and PNM were averaged to obtain the matrix elements for region B. Thirty seconds of record were used in the cross-correlation calculations, except for the SME record of the January 31, 1979 event in region B (Figure 3-4).

Figure 3-8. Cross-correlation matrices for seismograms of earthquakes in the magnitude range 2-3 within the regions shown during the time periods indicated. See Figure 3-7 for explanation. Peak cross-correlation values from 2 to 5 different pairs of records were averaged to obtain each matrix element. Whole seismograms (usually 30 sec long) from CEDAR were used for these cross correlations except for the earthquakes from the San Fernando region, for which S waves hand digitized from Wood-Anderson records were used. The order of events within each matrix is chronological from top to bottom and left to right.

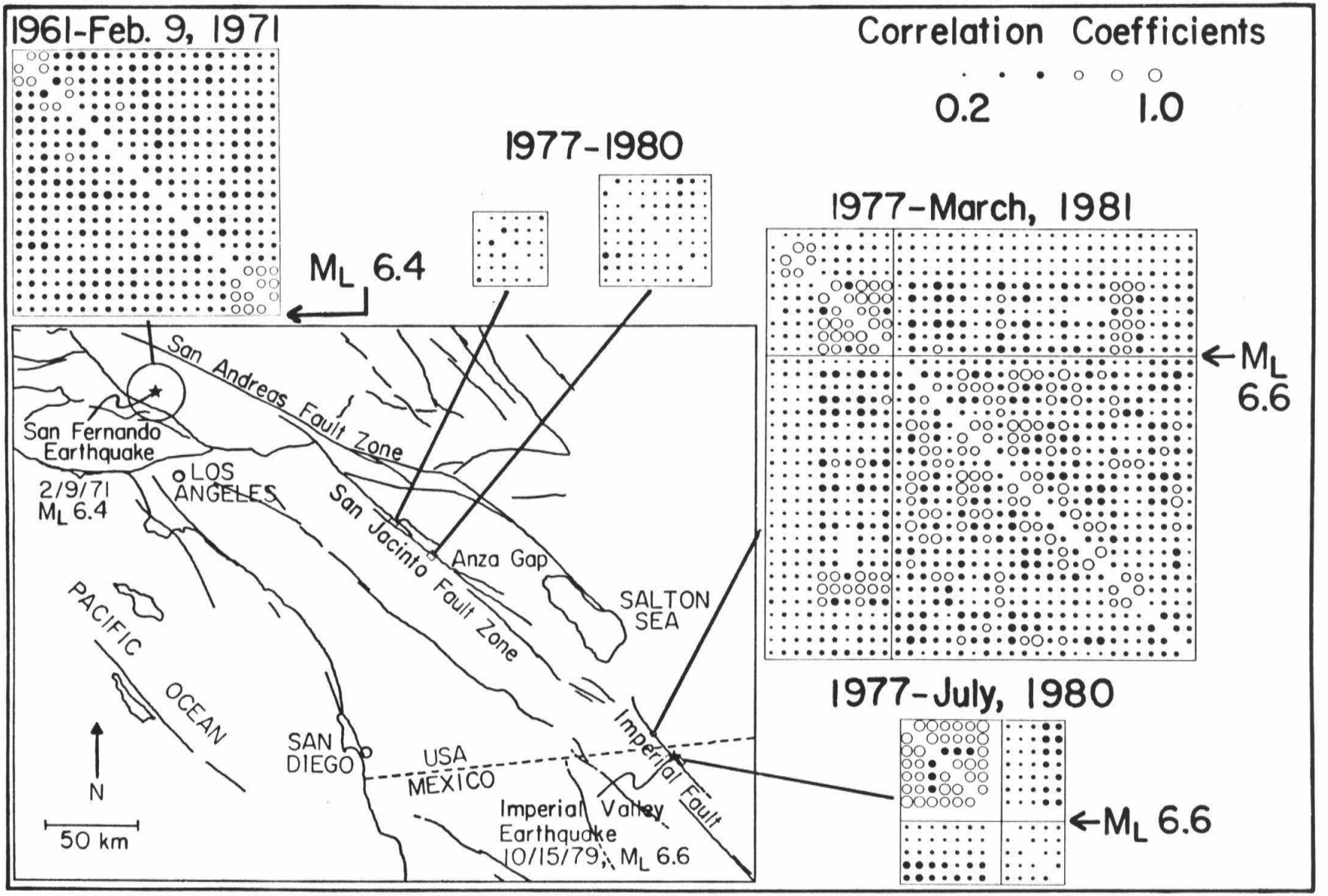
1961-Feb. 9, 1971
Correlation Coefficients
0.2
1.0
1977-1980
1977-March, 1981
M_L 6.4
M_L 6.6
San Andreas Fault Zone
San Fernando Earthquake
2/9/71
M_L 6.4
LOS ANGELES
San Jacinto Fault Zone
Anza Gap
SALTON SEA
PACIFIC OCEAN
SAN DIEGO
USA
MEXICO
Imperial Fault
Imperial Valley Earthquake
10/15/79, M_L 6.6
1977-July, 1980
M_L 6.6
N
50 km

unusual, although not strictly limited to the periods preceding major earthquakes.

Focal Mechanisms

To construct the focal mechanisms, first motions and arrival times for the events in regions A and B were reread from the digital CEDAR seismograms. In order to determine a realistic set of takeoff angles for the first-motion diagrams, plots of reduced travel time, $T-\Delta/6.0$, versus distance, Δ, were made for each event and compared with the predictions of various crustal models. Figure 3-9 shows a typical example. The Southern California model used for the relocations (inset, Figure 3-9a) is similar to the crustal model used for routine location of southern California earthquakes. It is essentially a model for the central Transverse Ranges based on Hadley and Kanamori (1977). The Southern California model fits all travel times reasonably well out to a distance of about 60 km, the distance cutoff used in the locations. It also fits arrival times for the more distant stations in the central Transverse Ranges and western Peninsular Ranges at azimuths of 135° to 315° (Figure 3-9b). However, this model gives a poor fit to the arrivals at stations in the eastern Transverse Ranges and Mojave Desert at azimuths of 315° to 135°, because it predicts apparent velocities of 6.7 km/sec beyond a distance of 65 km or less for the deeper earthquakes (>12 km), which is much faster than the 6.2 km/sec actually observed (Figure 3-9a,c). The Mojave model from Kanamori and Hadley (1975) and Hadley (1978) shown in the inset in Figure 3-9c provides a good fit to

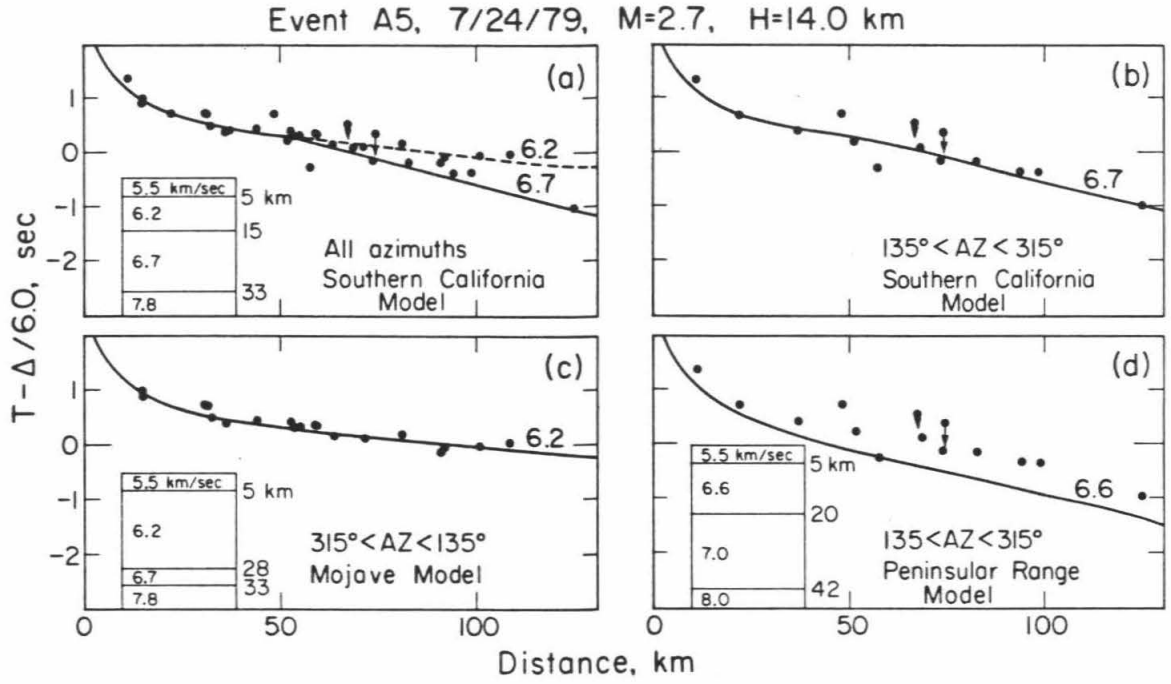

Figure 3-9. Plots of reduced travel time, T-Δ/6.0, versus distance, Δ, for the azimuth ranges indicated. The source is a local magnitude 2.7 event on July 24, 1979, in region A at a depth of 14 km. Solid curves show theoretical reduced travel times for various crustal models (insets). The location and origin time assumed is that of Table 3-1. Vertical arrows below some points indicate corrections for deep sediments determined by Raikes (1978).

the data at these azimuths. The Mojave model differs from the Southern California model only in the depth of the interface between the 6.2 km/sec upper crust and the 6.7 km/sec lower crust, the Conrad discontinuity. A model that differs significantly from both of these was derived by Nava and Brune (1982) from a NW-SE earthquake-explosion reversed refraction line in the Peninsular Ranges. It predicts travel times that are significantly faster than those observed for these earthquakes at the Peninsular Range stations, assuming the master event relocations are correct (Figure 3-9d). The earthquake origin times and depths could be adjusted to improve the fits for this model at the Peninsular Range stations, but this would degrade the fit of the Mojave and eastern Transverse Range data to the Mojave model. In general, the Southern California model seems to provide a better fit for the southward and westward travel paths. This may be because the high crustal velocities in the Peninsular Ranges are restricted to that part of the province west of the Elsinore fault, as suggested by Hadley (1978).

Based on the analysis of the travel-time curves, the takeoff angles for the focal mechanisms were determined from the Southern California (Transverse Range) model for stations at azimuths of 135^{o} to 315^{o} and from the Mojave model for stations at azimuths of 315^{o} to 135^{o}, using the master event relocations. An exception was made for the July 18, 1978, event in region A, for which the Mojave model was used at all azimuths because refractions from the Conrad discontinuity were not observed. This is probably because the first arrivals were missed at

the 3 or 4 stations where, based on data from the other earthquakes, such refractions were expected as first arrivals. Earthquakes with calculated depths greater than or equal to 15 km were assigned depths of 14 km for calculating the takeoff angles in order to put them above the 15 km discontinuity in the Transverse Range model. This makes the P* branch (6.7 km/sec apparent velocity) a refracted branch for all of these earthquakes, which seems most likely in light of the available data. The depth of the December 13, 1979, event in region A, 6 km, is near the 5 km velocity discontinuity present in all three crustal models considered above. As discussed in Chapter 1, earthquakes located near velocity discontinuities present particular problems in determining focal mechanisms, because the travel-time curves for a source located just above a discontinuity are nearly identical to those for a source located just below it, but the takeoff angles are quite different. In this case, however, the allowable mechanisms assuming a depth of 4 km are similar to those determined for a depth of 6 km, so we chose to present only the solution for the calculated depth of 6 km. The depth of the Sept. 28, 1980, event (region B) was changed from 2.5 km to 0 km to obtain a better fit to the observed 5.5 km/sec to 6.2 km/sec crossover distance.

Figures 3-10 and 3-11 show the P-wave first motion plots for the $M_L \geq 2$ events in regions A and B, respectively. The contours in these figures, determined with the aid of the computer program FOCPLT (see Chapter 1), enclose the locus of positions for slip vectors corresponding to solutions with no readings in error. The extent of the

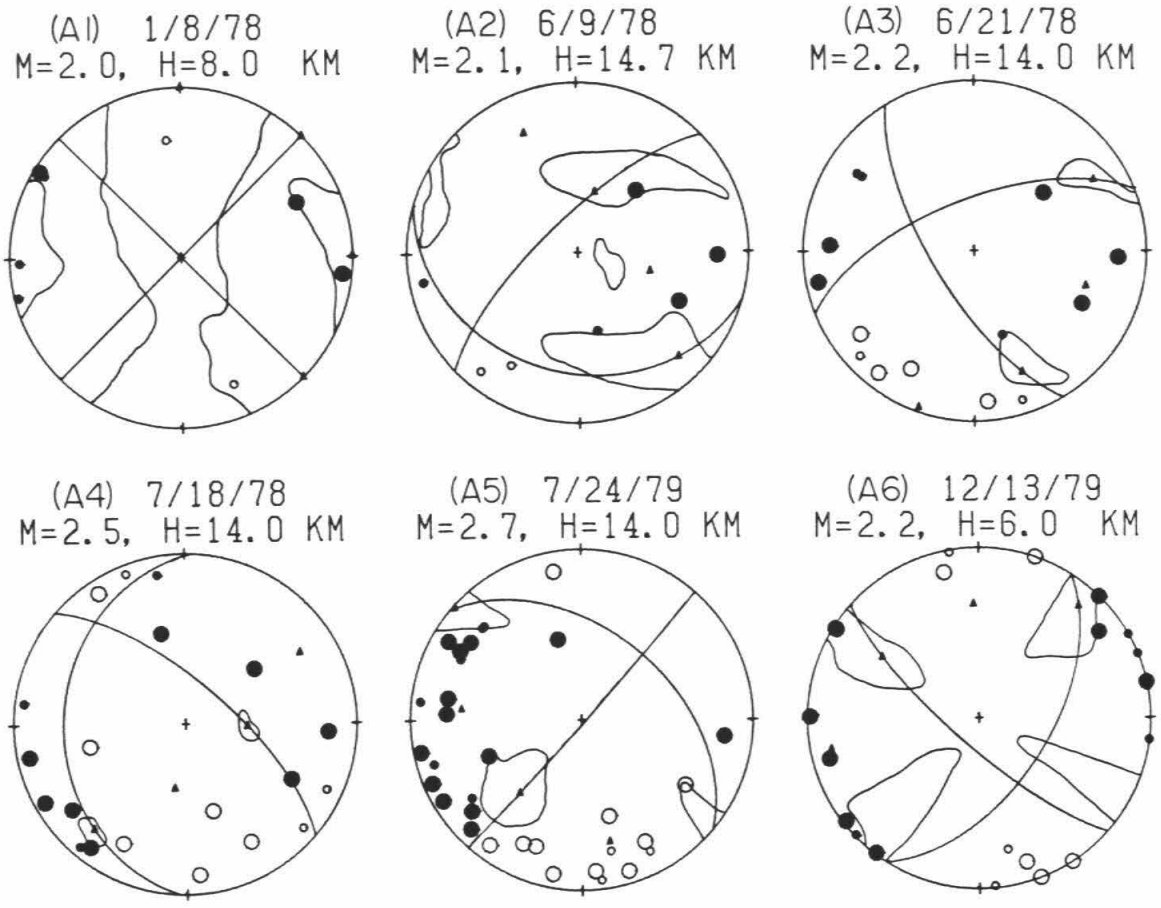

Figure 3-10. Lower hemisphere P-wave fault-plane solutions for events in region A. Solid circles indicate compressional first motions; open circles indicate dilatational ones. The large circles represent good-quality readings; the small circles fair-quality readings. Slip vectors, compression axes, and tension axes are shown with triangles. The date, local magnitude M, and depth H for each event is given. The contours indicate the range of positions for slip vectors corresponding to solutions with the minimum number of readings in error.

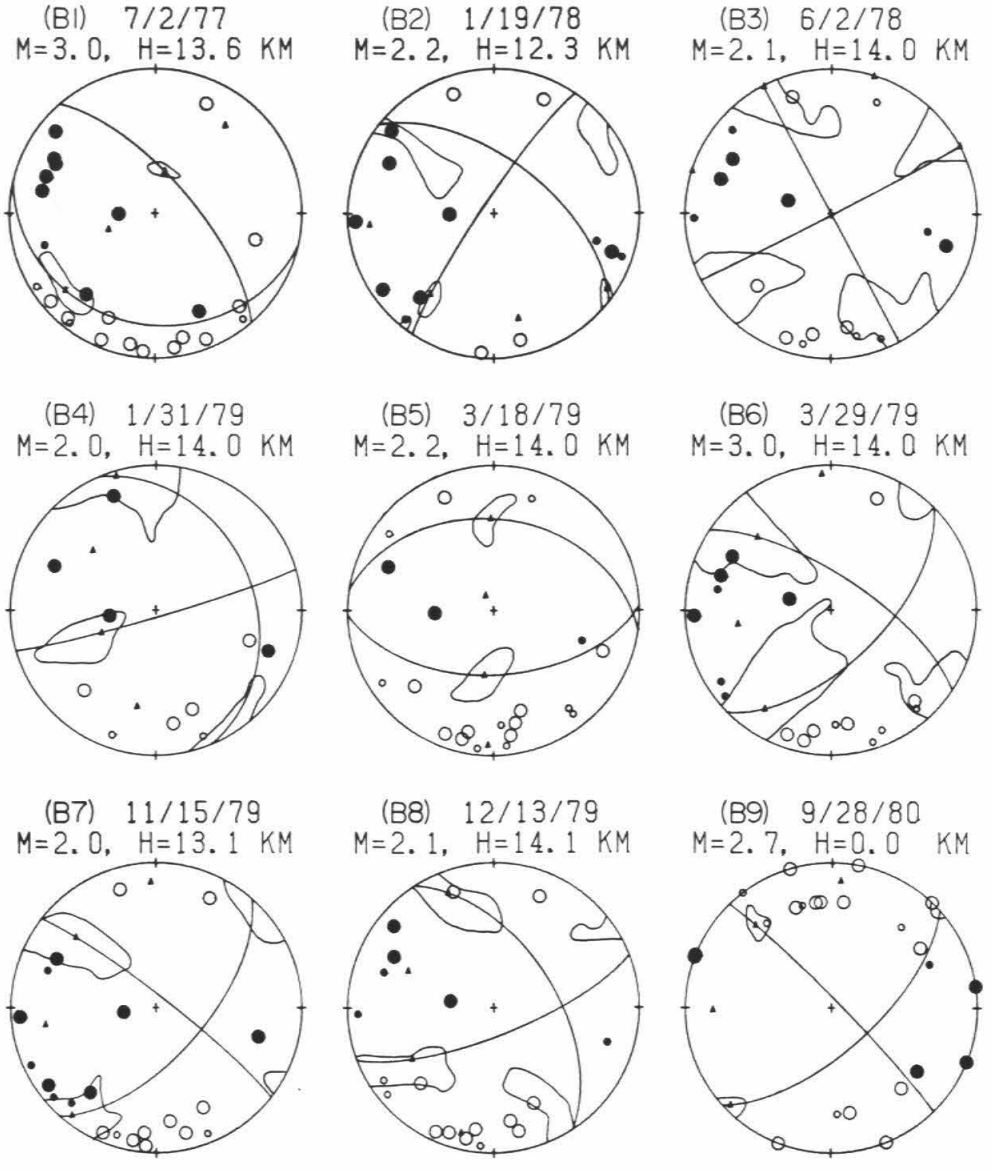

Figure 3-11. Fault-plane solutions for events in region B. See Figure 3-10 for explanation.

contoured regions on each plot is a measure of the degree of constraint of the mechanism, given the particular set of takeoff angles used. The nodal planes shown for each earthquake are, for the most part, those chosen by FOCPLT. These are not necessarily any more appropriate than other possible sets of planes that agree equally well with the data.

Most of the first motion diagrams in both study regions are consistent with right-lateral strike-slip motion on steeply-dipping faults that strike approximately northwest. This agrees well with the geologically determined faulting on the major branches of the San Jacinto fault zone (Sharp, 1965, 1967). Mechanisms A4, B1, and B5, however, are clearly different from the rest and are well constrained (Figures 3-10 and 3-11). Mechanisms A4, for the July 18, 1978, event in Region A, indicates normal faulting on a north- or northwest-striking fault plane. Region A is at the southeastern end of the San Jacinto Valley, a graben formed by a right step between two en echelon branches of the San Jacinto fault zone (Sharp, 1975). Therefore, some normal faulting is not particularly surprising here. Mechanisms B1 (July 2, 1977, region B) shows reverse faulting on either a northwest-striking plane dipping northeast or an east-striking plane dipping to the south. Sharp (1965, 1967) has mapped a thrust fault within region B that strikes northwest, parallel to the San Jacinto fault zone, and dips northeast. This fault provides a geologic analog to mechanism B1, although it may not be the same one on which the earthquake occurred. Similar thrust faults are found parallel to the fault zone further to the southeast. These thrust faults and mechanism B1 suggest compression

normal to the San Jacinto fault zone in the vicinity of the Anza seismic gap. Sanders and Kanamori (1983) hypothesize that this compression is due to the convergent fault geometries southeast of the gap (Figure 3-1) and may be responsible for locking the fault. Geodetic measurements of strain accumulation suggest that the regional stress field here has its most compressive principal stress oriented north-south (Savage et al., 1981b). North-south compression is consistent with right-lateral strike-slip motion on northwest-striking faults, as is observed both geologically and seismologically. It is also consistent with reverse faulting on east-west striking planes, as is seen in mechanism B5. Sharp's (1965) map shows an east-west trending thrust fault in crystalline rocks near Hemet Reservoir just northeast of region B, but this fault does not cut the youngest Quaternary sediments southeast of the reservoir and so it may no longer be active (Hill, 1981). Thus, although there is some variation in the types of mechanisms found for small earthquakes in regions A and B, the overall agreement between the mechanisms and the surface geology at these locations is remarkably good. This is certainly not always the case in southern California (e.g., Chapter 1).

Conclusions

Waveform studies of small earthquakes within two small (< 5 km) regions along the San Jacinto fault zone support the idea that ordinary 'background' seismic activity does not consist of clusters of similar events within localized source areas a few hundred meters in size.

However, more data are needed before the significance of such clustering, observed before the 1971 San Fernando and 1979 Imperial Valley earthquakes (Chapter 2 and Figure 3-8), can be fully evaluated. An especially interesting place for future studies is the region southeast of the Anza seismic gap where a magnitude 5.5 earthquake occurred on February 25, 1980.

Fifteen focal mechanisms of $M_L \geq 2.0$ earthquakes in these two areas suggest that most of the small earthquake faulting in the San Jacinto fault zone consists of strike-slip movement on steeply-dipping, northwest-striking faults, in agreement with the results of Sanders and Kanamori (1983). Displacements across this fault zone due to large earthquakes ($M \geq 6$) and creep are also dominated by right-lateral strike-slip motion on steeply-dipping faults, as inferred from geologic, seismologic, and geodetic evidence (Sharp, 1967; U.S. Geological Survey, 1972; Thatcher and Hamilton, 1973; Keller et al., 1978). The non strike-slip mechanisms found correlate well with local complications in the faulting patterns.

The concentration of small earthquake activity near the major faults of the San Jacinto fault zone and the general agreement between their faulting mechanisms and fault displacements mapped at the surface suggests that many of these earthquakes may be associated with the major strike-slip faults of this zone. Unfortunately, it is not possible to prove this hypothesis with the data at hand. In other parts of southern California, such as the central Transverse Ranges (Chapter 1), the diffuse nature of the seismicity and the poor correlation between small

earthquake focal mechanisms and nearby major faults argues that most of the small earthquakes occur along minor faults. The degree to which small earthquake activity is concentrated along major faults may depend on the strength of these faults relative to the strength of the surrounding blocks. It may also depend on the manner in which the faults are being loaded. A strain-rate profile extending through the Anza gap eastward to the San Andreas fault and westward to the Elsinore fault shows that the rate of accumulation of right-lateral shear strain parallel to these faults is significantly higher near the San Jacinto and San Andreas faults than it is elsewhere (King and Savage, 1982). This implies that slip at depth on the San Jacinto and San Andreas faults is loading the upper parts of these faults. The high level of seismicity along the San Jacinto fault zone may reflect this local concentration of stress caused by creep on the fault zone at depth (Sanders and Kanamori, 1983). If this is the case, then clearly other factors such as mechanical properties of fault zone materials must be important as well, because there is no analogous concentration of small earthquake activity along the San Andreas fault zone in this region (Figure 3-1).

It is clear that over the long term the major fault zones represent the primary zones of weakness because most of the deformation is taken up along them. Thus, if small earthquakes do occur on these faults, what prevents them from becoming larger earthquakes? The answer suggested in Chapter 2 is that the rupture dimensions are controlled by variations in mechanical properties along these faults. Specifically,

it is hypothesized that small earthquakes represent the failure of asperities, those parts of a fault with higher than average strength that prevent the fault from slipping. The next chapter discusses this hypothesis in light of recent source studies of small earthquakes.

CHAPTER 4

Source Studies of Small Earthquakes: A Review

If small earthquakes do indeed represent the fracture of asperities on faults, one might expect that some evidence for this could be obtained from source studies of small earthquakes. Unfortunately, the complexities of short-period wave propagation make it difficult to obtain reliable information about small earthquake source processes from local seismograms. This chapter reviews the literature on small earthquake source parameters and the problems involved in determining them.

Several investigators have found that stress drops for earthquakes with moments larger than about 10^{21} dyne-cm ($M_L \sim 3$) are independent of earthquake size and generally lie in the range 1 to 100 bars (Thatcher, 1972; Thatcher and Hanks, 1973; Kanamori and Anderson, 1975; Cohn et al., 1982). Results from source studies of smaller earthquakes, on the other hand, have led many authors to conclude that their stress drops decrease with moment (e.g., Tucker and Brune, 1973; Frankel, 1981; Saito and Masuda, 1981, Hauksson, 1982). Several workers have observed the transition between these two different types of scaling, although the transition does not always seem to occur at the same threshold size everywhere (Chouet et al., 1978; Rautian et al., 1978; Archuleta et al., 1982; Hasegawa, 1982).

The decrease in stress drop with moment for small earthquakes

($M_L < \sim 3$), if real, would seem to run counter to the asperity model. According to this model, the smallest earthquakes represent the failure of the smallest asperities and might therefore be expected to have large, although probably widely varying, stress drops. Larger earthquakes might tend to have lower and more uniform stress drops because these stress drops would represent an average over a larger area of the fault. An analysis by Rudnicki and Kanamori (1981) of one-dimensional static crack models involving asperities, however, indicates that the failure of an asperity can induce significant slip on adjacent sections of fault even if the stress drop outside the region of the asperity is zero. Thus, although the localized stress drop across a small asperity can be very high, the stress drop averaged over the whole slip zone is much lower and, in their model, is always less than the effective stress (the difference between the tectonic stress and the frictional stress along the fault). In fact, as the stress drop across the asperity approaches infinity in the limit as the ratio of asperity length to total slip zone length goes to zero, the average stress drop across the whole region of slip approaches zero. The same holds true for the case of a circular asperity on a circular fault (McGarr, 1981). However, at least in the case of the one-dimensional crack model, the average stress drop is not greatly different from the effective stress (within a factor of 2) unless the ratio of asperity length to total crack length is very small ($< .09$) (Rudnicki and Kanamori, 1981).

At this point, it is necessary to consider how stress drops are estimated for small earthquakes. If a single asperity ruptured on a

fault, would seismological techniques measure the localized stress drop across the asperity or the average stress drop across the entire area of triggered slip? Stress drops for small earthquakes are usually estimated from seismological determinations of the total moment and fault length, using the solution for a circular crack with uniform stress drop in an infinite elastic medium derived by Eshelby (1957) and Keilis-Borok (1959). The plane-strain results of Rudnicki and Kanamori (1981) suggest that this approach should give a reasonable estimate of the average stress drop over the whole region of slip even when the local stress drop varies considerably within the region, provided that no unbroken segments of fault or 'barriers' remain within the slipped region. Estimates of seismic moment for small (M_L<5) earthquakes are most commonly derived from measurements of the long-period spectral amplitude of P waves or S waves (Thatcher and Hanks, 1973), although the time windows used for the spectral analysis generally include arrivals other than direct P or S. Other techniques used involve measurement of the area underneath the P-wave displacement pulse in the time domain (Frankel, 1981), measurements of coda amplitude on bandpass-filtered records (Aki and Chouet, 1975; Chouet et al., 1978; Rautian et al., 1978), or amplitude comparisons between observed and synthetic seismograms (Cohn et al., 1982). Because the moment is, by definition, equal to the product of the elastic rigidity and the integral of the final slip over the fault area, this quantity is independent of the details of faulting and is usually one of the more well-determined source parameters, provided that the recording instrument has sufficient

bandwidth to record waves at periods that exceed the duration of the faulting.

Unfortunately, seismological estimates of source dimension are much more difficult to obtain than estimates of moment. For earthquakes larger than about magnitude 5, the dimensions of the fault rupture can often be estimated from the initial aftershock distribution or from surface faulting. Fault dimensions for smaller earthquakes must be inferred from estimates of the source duration derived from seismic records. For a smooth rupture in an infinite, isotropic elastic medium, the far-field displacement signal for any component of either the P or the S phase observed at some given point is a unidirectional pulse with a width controlled by the duration of the rupture and the angle between the ray and the direction or directions of rupture propogation (Savage, 1966; 1972). The time history of the pulse is known as the far-field time function and is determined by the time history of the faulting. In general, for propagating ruptures the far-field time function will depend on the point of observation, but for bilaterally or radially propagating ruptures the effect on the total duration of the pulse is not too large (less than a factor of two) and is often neglected. Thus, observationally, the source duration can be obtained from the width of the far-field time function which produces the best-fitting synthetic seismograms (Cohn et al., 1982) or, after appropriate corrections for instrument response and propagation effects, from direct time-domain measurements of the width of far-field body-wave pulses (Frankel, 1981) or from corner frequencies of P- or S-wave spectra (Thatcher, 1972;

Thatcher and Hanks, 1973; Tucker and Brune, 1973; Saito and Masuda, 1981) or coda-wave spectra (Chouet et al., 1978; Rautian et al., 1978). The duration of a far-field body wave pulse is inversely related to the corner frequency of its spectrum, defined as the intersection of the low- and high-frequency asymptotes (Savage, 1972; Helmberger and Malone, 1975; Madariaga, 1976). Thus, the time-domain and frequency-domain methods are equivalent when simple body wave pulses are available for analysis. In practice, such simple pulses are rarely recorded on short-period local seismograms because scattering from velocity heterogeneities in the lithosphere introduces multiple arrivals. These multiple arrivals can be either modeled or ignored when using time-domain techniques but must in general be included in time windows for spectral analysis in order to make them long enough to resolve the spectrum at frequencies lower than the corner frequency. Thus, the spectral techniques rely on an assumption that the multiple arrivals do not significantly affect the spectrum or, in other words, that the elastic Green's functions for the earth can be treated to a good approximation as white noise.

Estimation of source dimensions from source duration is highly model dependent. For small earthquakes which do not break the surface, circular fault geometry and radially outward rupture propagation are usually assumed. Theoretically, a time function is derived by summing the time derivatives of the dislocation history at all points on the fault surface with time lags that suitably account for the time it takes for the rupture to propagate to each point and the time required for

propagation of the wave to the receiver. Thus, the width of the time function depends on both the propagation time, which is the time it takes for the rupture front to propagate over the entire fault surface, and the rise time, which is the time it takes for each point on the fault to slip and which may, in general, vary along the fault surface. For constant or nearly constant rupture velocity, the propagation time clearly scales with fault radius. The average rise time is also expected to scale with radius if one assumes that the stress drop due to faulting is equal to the effective stress accelerating the fault as it ruptures (Geller, 1976). This is because the velocity of a sliding fault surface is roughly proportional to the effective stress (Brune, 1970; Sato and Hirasawa, 1973) and, for a circular fault, the final average dislocation is proportional to both the static stress drop and the fault radius (Eshelby, 1957). Numerous kinematic and dynamic source models are available which can be used to infer source radii from corner frequency or pulse width data, the most popular model being that of Brune (1970, 1971). See Aki and Richards (1980) for a review of earthquake source models.

Dynamic source models that involve heterogeneous stress drop are now being developed. All of these models assume a uniform tectonic shear stress and a uniform dynamic frictional stress. Under these conditions, nonuniformity in stress drop can result from nonuniformity in initial fault stress caused by preseismic slip along some sections of fault (the asperity model) or from nonuniformity in postseismic fault stress resulting from the presence of barriers which did not undergo

slip (the barrier model). Both of these scenarios implicitly assume some intrinsic variation in static friction along the fault. The more general models include random variations in static friction which, in conjunction with some fracture criterion, completely determine the faulting history (Mikumo and Miyatake, 1978). The distinction between asperities and barriers in these more realistic dynamic source models is somewhat artificial, because when a propagating rupture hits a strong patch on a fault this patch can, depending on the circumstances, either break immediately, break after the rupture has propagated past it or around it, or not break at all (Das and Aki, 1977; Mikumo and Miyatake, 1978).

The simplest heterogeneous faulting model, and one of the most appealing as far as small earthquakes are concerned, involves the rupture of a single asperity on an infinite fault plane (Das and Kostrov, 1983) or a circular fault plane (McGarr, 1981) where the sress drop is zero outside the asperity. McGarr's model assumes an elastostatic solution for the initial and final displacements on the fault and a source time history for both the asperity and the surrounding annulus similar to that assumed in the Brune model. The resulting far-field time function is the superposition of two pulses, a relatively narrow one from the asperity and a broader one from the fault as a whole. Madariaga (1979) obtained numerical solutions for the dynamic rupture on a fault with a single zone of zero stress drop flanked by two asperities and for a fault composed of two subfaults separated by an unbreakable barrier. Both models produced similar

far-field time functions consisting of two pulses whose individual widths were related to the rupture propagation time through the asperities or subfaults, although the total width of each time function was related to the rupture time for the whole fault. The spectra of these time functions contained two corner frequencies, although poorly defined, which likewise corresponded to the two characteristic rupture lengths in the models. It is clear that more complex source models will produce greater complexity in both the far-field time function and its spectrum and that, at least for larger earthquakes, the degree of complexity possible is nearly limitless (Mikumo and Miyatake, 1978; Das and Aki, 1977). Unfortunately, even moderate source complexity is difficult or impossible to distinguish from propagation effects on local short-period seismograms, although some progress has been made in unravelling source complexities from teleseismic body waves (e.g., Hartzell, 1980; Ebel and Helmberger, 1982; Stewart and Kanamori, 1982) and from the longer-period components of near-field strong-motion records (Hartzell and Helmberger, 1982). Nevertheless, if the structural effects are well-known or else not very severe, as often appears to be the case for direct waves propagating through hard rock, and if the bandwidth of the recording instrument is appropriate for the size of the earthquake, it should be possible in most cases to estimate the overall duration of small earthquake sources from local seismograms.

Returning to the problem of the apparent decrease in stress drop with moment for small earthquakes, the key observation is as follows. For earthquakes with moments larger than about 10^{21} dyne-cm ($M_L \sim 3$), the

measured source durations increase roughly in proportion to the cube root of the moment (Thatcher, 1972; Thatcher and Hanks, 1973; Cohn et al., 1982; Archuleta et al., 1982). Assuming a circular fault geometry and a rupture time proportional to the fault radius, this implies that the stress drop is approximately constant for moderate to large earthquakes, because for a circular fault the stress drop is directly proportional to the moment and inversely proportional to the cube of the radius. Circular fault geometry is probably a reasonable approximation for most earthquakes, except for large earthquakes on long, narrow strike-slip faults which are a separate problem (Scholz, 1982). In contrast to these results, studies of smaller earthquakes usually show that on the average their measured source durations increase with moment much more slowly, if at all, until some critical moment is reached (Tucker and Brune, 1973; Smith et al., 1974; Chouet et al., 1978; Rautian et al., 1978; Frankel, 1981; Saito and Masuda, 1981; Archuleta et al., 1982; Hauksson, 1982; Hasegawa, 1982). This critical moment, the minimum source duration, and the calculated range of stress drops all vary somewhat from one region to another, but the limiting corner frequencies for S waves are generally in the neighborhood of 10-20 Hz and are reached for earthquakes with moments less than about 10^{19}-10^{21} dyne-cm. When the displacement spectra have corner frequencies lower than the maximum corner frequency, a more rapid spectral amplitude falloff for frequencies greater than the maximum corner frequency can sometimes be discerned (Archuleta et al., 1982). This effect can be observed more easily on shear wave acceleration spectra

derived from strong motion records. Such spectra typically show a relatively flat maximum for frequencies between the corner frequency of the corresponding displacement spectrum and some higher frequency which, at least for California earthquakes, corresponds to the limiting corner frequency of about 10-20 Hz usually observed for shear-wave displacement spectra of smaller events (Hanks, 1982). Thus, there appears to be a high-frequency band limitation for seismic energy from earthquakes. This limit has been termed 'f_{max}' by Hanks (1979), although it is not as abrupt as the name implies. The f_{max} phenomenon has been observed in source parameter studies using P waves (Saito and Masuda, 1981; Frankel, 1981; Hauksson, 1982), coda waves (Chouet et al., 1978; Rautian et al., 1978) and S waves (summarized in Archuleta et al., 1982), although a study by Bakun et al. (1976) of corner frequencies for $0.9 \leq M_L \leq 4.1$ earthquakes in the Bear Valley region of central California suggests that f_{max} is not necessarily the same for P waves and S waves. The SH corner frequencies for these earthquakes reach an upper limit of about 15-20 Hz, but the PZ corner frequencies continue to increase with decreasing moment out to almost 30 Hz.

The most direct interpretation of the observation of maximum corner frequency (or minimum pulse width), and the one subscribed to by Chouet et al. (1978) and several subsequent investigators, is that there is a lower limit to the radius of faulting in earthquakes which is controlled by a characteristic spacing of strong barriers along faults. According to this hypothesis, these barriers are strong enough to stop most ruptures but may break in larger earthquakes. Thus, the calculated

stress drops decrease with decreasing moment for earthquakes which cannot break through the strong barriers, although it is presumed that these earthquakes might break weaker asperities or barriers in between. The problem with this hypothesis is that there is no obvious reason why a characteristic spacing for barriers should exist and moreover show such comparatively little variation from region to region. Furthermore, earthquake magnitude/frequency of occurrence statistics provide no support for the idea of a minimum rupture size for earthquakes (Hanks, 1982). Thus, if f_{max} is a source effect, it appears that the simple linear scaling of source duration with fault radius must break down for small earthquakes. One way this could happen is if the rupture velocity is not strictly constant but instead increases gradually to a terminal velocity, as expected on theoretical grounds (Andrews, 1976). Bakun et al. (1980) suggested that small earthquakes might stop before reaching terminal rupture velocity, and that therefore their source duration might approach some minimum as the radius of rupture decreased. Whether or not such a mechanism can explain all of the relevant observations cannot be answered without further theoretical work.

Before concluding that f_{max} is a source effect, one must eliminate other possibilities such as propagation effects or problems with the calibration of the seismic recording instruments at high frequencies. With regard to the latter, the studies cited above were done using a variety of different seismometers and recorders, so unless there is some unrecognized and pervasive problem in determining the response of short-period instruments, such as significant nonlinearity, it is

unlikely that miscalibration can explain these results. Propagation effects such as anelastic attenuation, scattering and diffraction can have a strong effect on seismic waves. It is well known that anelastic attenuation and scattering combine to diminish the amplitude of seismic waves as they travel through the earth, and that this effect is more pronounced at higher frequencies. Apparent attenuation (which includes energy losses due to both scattering and anelastic attenuation) can be measured by comparing the frequency content of seismograms recorded at various distances from some source whose spectral characteristics are nearly isotropic, although not necessarily known. Decreases in spectral amplitude with distance can usually be fit well with a simple attenuation operator of the form $\exp(-\pi ft/Q)$ where f is frequency, t is travel time, and $2\pi/Q$ is the average fractional energy loss per unit cycle. Corrections for apparent Q were made using the inverse of this operator in most of the studies cited above, except in cases where the path lengths were short enough for this correction to be inconsequential. In the coda-wave studies, a frequency-dependent apparent Q was evaluated and corrected for. Thus, attenuation and scattering cannot explain the observations of f_{max} unless the energy loss is concentrated within a relatively small portion of the travel paths, such as near the source or near the receiver. Laboratory measurements of attenuation in rocks at ultrasonic frequencies show a rapid increase in Q^{-1} with increasing strain when the strain exceeds some critical value, usually around 10^{-6} or 10^{-5}. (See Stewart and Toksoz, 1983, for a summary of these measurements.) Dynamic strains

exceeding these values are expected close to an earthquake source, so if this nonlinearity in attenuation also occurs at seismic frequencies then the rate of attenuation could be much greater in the near-source region than elsewhere. There are also reasons to believe that apparent attenuation could be much greater near the surface than it is deeper down. It is possible that frictional dissipation across cracks and joints is an important loss mechanism, and that the importance of this mechanism increases with decreasing depth (Hanks, 1982). Also, high frequency energy may be reflected off low velocity layers near the surface while low frequency energy is diffracted into these layers and trapped, giving the appearance of strong attenuation (Heaton and Helmberger, 1978).

Two lines of evidence suggest that f_{max} is a propagation effect which is at least partially dependent on the local conditions of the recording site. The first is that f_{max} often shows a small but resolvable variation from one recording site to another. This has been shown by Frankel (1982b) for limiting corner frequencies of P- and S-waves of earthquakes in the northeastern Caribbean, and by Hanks (1982), who measured f_{max} on shear wave acceleration spectra of aftershocks of the Oroville earthquake. In the latter case, there was a correlation between f_{max} and gross surface geology. The other evidence suggesting that propagation effects control f_{max} comes from source parameter studies performed at particularly close distances (< 5 km) in especially competent rock. In such studies, limiting corner frequencies are either not observed or are higher than those usually found (Hanks,

1982). Pearson (1981) determined corner frequencies ranging from about 200-900 Hz for S waves and about 300-1200 Hz for P waves on recordings made within a few hundred meters of microearthquakes generated by hydraulic fracturing experiments in granitic rocks. The calculated stress drops averaged about one bar. Spottiswoode and McGarr (1975) and McGarr et al. (1981) studied source parameters of tremors in a deep-level gold mine using a seismometer at the surface about 3 km from the activity and accelerometers in the mine at hypocentral distances of 50 m to 1.6 km. Propagation paths were through hard crystalline rock, predominantly quartzites. S-wave corner frequencies exceeding 100 Hz were observed. Calculated stress drops ranged from 1 to 100 bars and showed no consistent dependence on moment down to 5×10^{16} dyne-cm ($M_L \sim -1$). Marion and Long (1980) found S-wave corner frequencies as high as 200 Hz for earthquakes near the Clark Hill Reservoir along the South Carolina-Georgia border in the Piedmont Crystalline province at hypocentral distances of 0.5-5 km. There is no clear correlation between average stress drop (~0.1 bars) and moment for these events in the moment range 10^{13}-10^{18} dyne-cm, although the smallest stress drop estimates are for some of the smallest events. Fletcher (1980) observed S-wave corner frequencies of 10 to 43 Hz for small ($0.6 \leq M \leq 2.6$) aftershocks of the Oroville earthquake using records from a site on crystalline bedrock within 3-6 km of most of the hypocenters. Both P- and S-wave corner frequencies appear to reach a maximum for this data set, resulting in stress drop estimates that correlate with moment, but the scatter in the measurements and the relatively small size range for

these events (nearly all have moments between 10^{17} and 10^{19}) make it difficult to draw definite conclusions. Finally, Fletcher (1982) has recovered S-wave corner frequencies as high as 40-50 Hz for small events apparently induced by the filling of Monticello Reservoir in South Carolina, at hypocentral distances of 1-5 km through igneous and metamorphic rocks. Again, an apparent increase in stress drop with moment for these events implies that the corner frequencies are at or near saturation.

In contrast to these observations showing high limiting corner frequencies (>40 Hz) or no limit at all for short propagation paths (<5 km) through hard, crystalline rocks, S waves of microearthquakes associated with coal mines in eastern Utah recorded at comparable distances (1-3 km) through sedimentary rocks have corner frequencies which are nearly the same (10-14 Hz) over two orders of magnitude of seismic moment (10^{17}-10^{19} dyne-cm) (Smith et al., 1974). Thus, in some cases, limiting corner frequencies can be observed at very short distances. It must be emphasized that this phenomenon cannot be due to ordinary whole-path attenuation and scattering. Smith et al. corrected their spectra for attenuation using a Q_s of 100, which they judged to be an appropriate value for sedimentary rocks. Although the Q they used was only an estimate, at such short distances (<3 km) the corrected spectra are insensitive to the exact value used as long as it is within a reasonable range. Furthermore, whole-path attenuation should produce a distance-dependent f_{max}, which was not observed in the study of Smith et al. The fact that f_{max} appears to be related to the material through

which the seismic waves have propagated suggests that the removal of the high frequencies (or possibly the enhancement of the low frequencies) is a propagation effect, but this cannot be conclusively demonstrated with the data at hand. If f_{max} is caused by a propagation effect, it must be a localized one. A detailed study of wave propagation near the earth's surface using instruments located at various depths within a deep (> 1/2 km) borehole would help to resolve some of these questions.

In conclusion, presently available techniques for studying small earthquake sources cannot resolve such fine details as how a rupture starts and stops and therefore cannot provide any information about how individual small events are related to heterogeneities on faults. Even gross source parameters such as overall stress drop are not easy to determine reliably. Part of the difficulty is that velocity variations in the earth can introduce considerable complexity into short-period waveforms, and such complexity is difficult to distinguish from complexity caused by the source. Another problem is that numerous studies have found a high frequency band limitation to seismic energy from earthquakes that is unrelated to magnitude or moment. It is not known at present whether this is a source effect or a propagation effect, but circumstantial evidence suggests it is the latter. Until this is resolved, the widely published conclusion that stress drops increase with moment for small earthquakes should not be taken at face value. Because some data suggest that this high-frequency band limitation ('f_{max}') may not always be abrupt, it cannot be assumed that spectra are completely free from this effect at frequencies less than

f_{max}.

The fact that corner frequencies of smaller earthquakes ($M_L < \sim 3$) are usually found to be nearly independent of event size helps to explain some of the results presented in Chapter 2. The existence of limiting corner frequencies implies that waveforms of very small earthquakes are insensitive to the details of the source and are instead controlled by radiation pattern, attenuation, and scattering from velocity heterogeneities in the crust. Thus, for earthquakes this small, changes in stress drop with time may be difficult to observe even if they occur. On the other hand, these waveforms can provide important information on relative source locations because two earthquakes in the same place will produce nearly the same waveforms (except for amplitude) as long as both are below a certain critical size. It may be possible to use the waveforms of very small events ($M_L \leq 2$) as empirical Green's functions to correct seismograms of larger earthquakes for path effects so that their source properties can be studied (Frankel and Kanamori, 1982). Understanding source properties of small earthquakes is extremely important for understanding their relationship to major fault systems and the cycles of strain accumulation and release which occur on them.

REFERENCES

Aki, K. (1979). Characterization of barriers on an earthquake fault, J. Geophys. Res., 84, 6140-6148.

Aki, K., and B. Chouet (1975). Origin of coda waves: Source, attenuation, and scattering effects, J. Geophys. Res., 80, 3332-3342.

Aki, K., and P. G. Richards (1980). Quantitative Seismology: Theory and Methods, 932 pp., W.H. Freeman, San Francisco, Calif.

Allen, C. R. (1968). The tectonic environments of seismically active and inactive areas along the San Andreas fault system, in Proceedings of the Conference on Geologic Problems of the San Andreas Fault System, edited by W. R. Dickinson and A. Grantz, pp. 70-82, Stanford University Publications in the Geological Sciences, Vol. 11, Stanford University Press, Palo Alto, Calif.

Allen, C. R. (1981). The modern San Andreas fault, in The Geotectonic Development of California, edited by W. G. Ernst, pp. 512-534, Prentice-Hall, Englewood Cliffs, New Jersey.

Allen, C. R. (1982). Creep and strain studies in southern California, in Summaries of Technical Reports, National Earthquake Hazards Reduction Program, Vol. 13, U. S. Geol. Surv. Open-File Rep. 82-65, 225-227.

Allen, C. R., P. St. Amand, C. F. Richter, and J. M. Nordquist (1965). Relationship between seismicity and geologic structure in the southern California region, Bull. Seism. Soc.

Am., 55, 753-797.

Anderson, E. M. (1951). The Dynamics of Faulting, 206 pp., Oliver and Boyd, Edinburgh.

Andrews, D. J. (1976). Rupture velocity of plane strain shear cracks, J. Geophys. Res., 81, 5679-5687.

Andrews, D. J. (1980). A stochastic fault model, 1. Static case, J. Geophys. Res., 85, 3867-3877.

Archambeau, C. B. (1979). Earthquake hazards determinations based on tectonic stress measurements, Semi-Annu. Tech. Rep. 3, U. S. Geol. Surv. Contract No. 14-08-0001-16773.

Archuleta, R. J., E. Cranswick, C. Mueller, and P. Spudich (1982). Source parameters of the 1980 Mammoth Lakes, California earthquake sequence, J. Geophys. Res., 87, 4595-4607.

Bailey, T. L., and R. H. Jahns (1954). Geology of the Transverse Range province, southern California, in Geology of Southern California, edited by R. H. Jahns, Calif. Div. Mines Bull. 170, 83-106.

Bakun, W. H., C. G. Bufe, and R. M. Stewart (1976). Body-wave spectra of central California earthquakes, Bull. Seism. Soc. Am., 66, 363-384.

Bakun, W. H., and T. V. McEvilly (1979). Are foreshocks distinctive? Evidence from the 1966 Parkfield and the 1975 Oroville, California sequences, Bull. Seism. Soc. Am., 69, 1027-1038.

Bennett, J. (1977). Palmdale 'Bulge' update, Calif. Geol., 30, 187-188.

Bird, P., and K. Piper (1980). Plane-stress finite-element models of

tectonic flow in southern California, Phys. Earth Planet. Inter., 21, 158-175.

Brune, J. N. (1970). Tectonic stress and the spectra of seismic shear waves from earthquakes, J. Geophys. Res., 75, 4997-5009.

Brune, J. N. (1971). Correction (to Brune, 1970), J. Geophys. Res., 76, 5002.

Brune, J. N. (1979). Implications of earthquake triggering and rupture propagation for earthquake prediction based on premonitory phenomena, J. Geophys. Res., 84, 2195-2198.

Burford, R. O., and P. W. Harsh (1980). Slip along the San Andreas fault in central California from alinement array surveys, Bull. Seism. Soc. Am., 70, 1233-1261.

Castle, R. O., J. P. Church, and M. R. Elliott (1976). Aseismic uplift in southern California, Science, 192, 251-253.

Chavez, D., J. Gonzalez, A. Reyes, M. Medina, C. Duarte, J. N. Brune, F. L. Vernon, R. Simons, L. K. Hutton, P. T. German, and C. E. Johnson (1982). Mainshock location and magnitude determination using combined U. S. and Mexican data, in The Imperial Valley, California, Earthquake of October 15, 1979, U. S. Geol. Surv. Prof. Pap. 1254, pp. 51-54, U. S. Government Printing Office, Washington, D. C.

Chouet, B., K. Aki, and M. Tsujuira (1978). Regional variation of the scaling law of earthquake source spectra, Bull. Seism. Soc. Am., 68, 49-79.

Cipar, J. (1981). Broadband time domain modelling of earthquakes from

Friuli, Italy, Bull. Seism. Soc. Am., 71, 1215-1231.

Cohn, S. N., T. Hong, and D. V. Helmberger (1982). The Oroville earthquakes: A study of source characteristics and site effects, J. Geophys. Res., 87, 4585-4594.

Cramer, C. H., and J. M. Harrington (1979). Seismicity and tectonics of the eastern San Gabriel Mountains area, San Bernardino and Los Angeles Counties, California, U. S. Geol. Surv. Prof. Pap., in press.

Crook, R., C. R. Allen, B. Kamb, C. M. Payne, and R. J. Proctor (1979). Quaternary geology and seismic hazard of the Sierra Madre and associated faults, western San Gabriel Mountains, California, U. S. Geol. Surv. Prof. Pap., in press.

Das, S., and K. Aki (1977). Fault plane with barriers: A versatile earthquake model, J. Geophys. Res., 82, 5658-5670.

Das, S., and B. V. Kostrov (1983). Breaking of a single asperity: Rupture process and seismic radiation, submitted to J. Geophys. Res..

Eaton, J. P. (1979). Temporal variation in the pattern of seismicity in central California, in Proc. UNESCO Internat. Symposium on Earthquake Prediction.

Ebel, J. E. (1981). Evidence for Fault Asperities from Systematic Time-Domain Modeling of Teleseismic Waveforms, Ph.D. Thesis, Calif. Inst. of Technol., Pasadena, Calif.

Ebel, J. E. and D. V. Helmberger (1982). P-wave complexity and fault asperities: The Borrego Mountain, California, earthquake of 1968,

Bull. Seism. Soc. Am., 72, 413-437.

Eshelby, J. D. (1957). The determination of the elastic field of an ellipsoidal inclusion and related problems, Proc. R. Soc. London, Ser. A, 241, 376-396.

Farnbach, J. S. (1975). The complex envelope in seismic signal analysis, Bull. Seism. Soc. Am., 65, 951-962.

Flaccus, C. E., R. M. Richardson, M. L. Sbar, T. Engelder, and D. Yale (1980). Tectonic stress near the San Andreas fault from strain relief measurements, Eos Trans. AGU, 61, 1118.

Fletcher, J. B. (1980). Spectra from high-dynamic range digital recordings of Oroville, California aftershocks and their source parameters, Bull. Seism. Soc. Am., 70, 735-755.

Fletcher, J. B. (1982). A comparison between the tectonic stress measured in situ and stress parameters from induced seismicity at Monticello Reservoir, South Carolina, J. Geophys. Res., 87, 6931-6944.

Frankel, A. (1981). Source parameters and scaling relationships of small earthquakes in the northeastern Caribbean, Bull. Seism. Soc. Am., 71, 1173-1190.

Frankel, A. (1982a). Precursors to a magnitude 4.8 earthquake in the Virgin Islands: Spatial clustering of small earthquakes, anomalous focal mechanisms and earthquake doublets, Bull. Seism. Soc. Am., 72, 1277-1294.

Frankel, A. (1982b). The effects of attenuation and site response on the spectra of microearthquakes in the northeastern Caribbean,

Bull. Seism. Soc. Am., 72, 1379-1402.

Frankel, A. and H. Kanamori (1982). Use of rupture duration for the study of the regional variation of seismic stress drops in southern California, Eos Trans. AGU, 63, 1031.

Friedman, M. E., J. H. Whitcomb, C. R. Allen, and J. A. Hileman (1976). Seismicity of the Southern California Region, 1 January 1972 to 31 December, 1974, Contribution Number 2734, Division of Geological and Planetary Sciences, Calif. Inst. of Technol., Pasadena, Calif.

Fuis, G. S., W. D. Mooney, J. H. Healy, G. A. McMechan, and W. J. Lutter (1982). Crustal structure of the Imperial Valley region, in The Imperial Valley, California, Earthquake of October 15, 1979, U. S. Geol. Surv. Prof. Pap. 1254, pp. 25-50, U. S. Government Printing Office, Washington, D. C.

Geller, R. J. (1976). Scaling relations for earthquake source parameters and magnitudes, Bull. Seism. Soc. Am., 66, 1501-1523.

Geller, R. J., and C. S. Mueller (1980). Four similar earthquakes in central California, Geophys. Res. Lett., 7, 821-824.

Goulty, N. R., R. O. Burford, C. R. Allen, R. Gilman, C. E. Johnson, and R. P. Keller (1978). Large creep events on the Imperial fault, California, Bull. Seism. Soc. Am., 68, 517-521.

Gutenberg, B., and C. F. Richter (1949). Seismicity of the Earth and Associated Phenomena, 310 pp., Princeton Univ. Press, 1st Ed., Princeton, New Jersey.

Hadley, D. (1978). Geophysical Investigations of the Structure and

Tectonics of Southern California, Ph.D. Thesis, Calif. Inst. of Technol., Pasadena, Calif.

Hadley, D., and J. Combs (1974). Microearthquake distribution and mechanisms of faulting in the Fontana-San Bernardino area of southern California, Bull. Seism. Soc. Am., 64, 1477-1499.

Hadley, D., and H. Kanamori (1977). Seismic structure of the Transverse Ranges, California, Bull. Geol. Soc. Am., 88, 1469-1478.

Hadley, D. and H. Kanamori (1978). Recent seismicity in the San Fernando region and tectonics in the west-central Transverse Ranges, California, Bull. Seism. Soc. Am., 68, 1449-1457.

Hamaguchi, H., and A. Hasegawa (1975). Recurrent occurrence of the earthquakes with similar waveforms and its related problems (in Japanese), J. Seism. Soc. Jpn., 28, 153-169.

Hanks, T. C. (1979). b values and $\omega^{-\gamma}$ seismic source models: Implications for tectonic stress variations along active crustal fault zones and the estimation of high-frequency strong ground motion, J. Geophys. Res., 84, 2235-2242.

Hanks, T. C. (1982). f_{max}, Bull. Seism. Soc. Am., 72, 1867-1879.

Hartzell, S. (1980). Faulting process of the May 17, 1976 Gazli, U.S.S.R. earthquake, Bull. Seism. Soc. Am., 70, 1715-1736.

Harsh, P. W., R. O. Burford, and Y. Kinugasa (1978). Rates of fault slip during historic time in central California, Eos Trans. AGU, 59, 1209.

Hartzell, S., and D. V. Helmberger (1982). Strong motion modelling of

the Imperial Valley earthquake of 1979, Bull. Seism. Soc. Am., 72, 571-596.

Hasegawa, H. S. (1982). Spectral scaling of eastern Canada earthquakes using both eastern Canada telemetered network and standard station seismograms, Earthquake Notes, 53, 41.

Hauksson, E. (1982). Some source parameters of small earthquakes in the Shumagin seismic gap, Alaska, Earthquake Notes, 53, 40.

Heaton, T. H. and D. V. Helmberger (1978). Predictability of strong ground motion in the Imperial Valley: Modeling the M 4.9, November 4, 1976 Brawley earthquake, Bull. Seism. Soc. Am., 68, 31-48.

Helmberger, D. V., and S. D. Malone (1975). Modeling local earthquakes as shear dislocations in a layered half-space, J. Geophys. Res., 80, 4881-4888.

Hileman, J. A., C. R. Allen, and J. M. Nordquist (1973). Seismicity of the Southern California Region, 1 January 1932 to 31 December, 1972, Contribution Number 2385, Division of Geological and Planetary Sciences, Calif. Inst. of Technol., Pasadena, Calif.

Hill, R. I. (1981). Geology of Garner Valley and vicinity, in Geology of the San Jacinto Mountains, Annual Field Trip Guidebook No. 9, edited by A. R. Brown and R. W. Ruff, pp. 90-99, South Coast Geological Society, Santa Ana, Calif.

Housner, G. W. (1955). Properties of strong ground motion earthquakes, Bull. Seism. Soc. Am., 45, 197-218.

Hutton, L. K., and C. E. Johnson (1981). Preliminary study of the

Westmoreland, California earthquake swarm, Eos Trans. AGU, 62, 957.

Imamura, A. (1937). Theoretical and Applied Seismology, 358 pp., Maruzen, Tokyo.

Ishida, M., and H. Kanamori (1978). The foreshock activity of the 1971 San Fernando earthquake, California, Bull. Seism. Soc. Am., 68, 1265-1279.

Ishida, M., and H. Kanamori (1980). Temporal variation of seismicity and spectrum of small earthquakes preceding the 1952 Kern County, California earthquake, Bull. Seism. Soc. Am., 70, 509-527.

Jackson, D. D., and W. B. Lee (1979). The Palmdale Bulge - An alternate interpretation, Eos Trans. AGU, 60, 810.

Jahns, R. H. (1973). Tectonic evolution of the Transverse Ranges province as related to the San Andreas fault system, in Proceedings of the Conference on Tectonic Problems of the San Andreas Fault System, edited by R. L. Kovach and A. Nur, pp. 149-170, Stanford University Publications in the Geological Sciences, Vol. 13, Stanford University Press, Palo Alto, Calif.

Jennings, C. W., R. G. Strand, T. H. Rogers, M. G. Stinson, J. L. Burnett, J. E. Kahle, R. Streitz, and R. A. Switzer (1975). Fault map of California with locations of volcanoes, thermal springs and thermal wells, Calif. Geol. Data Map Ser., Map 1, Calif. Div. of Mines and Geol., Sacramento.

Johnson, C. E. (1979). I, CEDAR--An Approach to the Computer Automation of Short-Period Local Seismic Networks, II, Seismotectonics of the

Imperial Valley of Southern California, Ph.D. Thesis, Calif. Inst. of Technol., Pasadena, Calif.

Johnson, C. E., and D. M. Hadley (1976). Tectonic implications of the Brawley earthquake swarm, Imperial Valley, California, January 1975, Bull. Seism. Soc. Am., 66, 1133-1144.

Johnson, C. E., and L. K. Hutton (1982). Aftershocks and preearthquake seismicity, in The Imperial Valley, California, Earthquake of October 15, 1979, U. S. Geol. Surv. Prof. Pap. 1254, pp. 59-76, U. S. Government Printing Office, Washington, D. C.

Jones, L. M., and P. Molnar (1979). Some characteristics of foreshocks and their possible relationship to earthquake prediction and premonitory slip on faults, J. Geophys. Res., 84, 3596-3608.

Kanamori, H. (1981). The nature of seismicity patterns before large earthquakes, in Earthquake Prediction: An International Review, Maurice Ewing Ser., vol. 4, edited by D. W. Simpson and P. G. Richards, pp. 1-19, AGU, Washington, D. C.

Kanamori, H. and D. L. Anderson (1975). Theoretical basis of some empirical relations in seismology, Bull. Seism. Soc. Am., 65, 1073-1095.

Kanamori, H., and D. Hadley (1975). Crustal structure and temporal velocity change in southern California, Pure and Appl. Geophys., 113, 257-280.

Kanamori, H., and G. S. Stewart (1978). Seismological aspects of the Guatemala earthquake of February 4, 1976, J. Geophys. Res., 83, 3427-3434.

Keilis-Borok, V. (1959). On estimation of the displacement in an earthquake source and of source dimensions, Ann. Geofis., 12, 205-214.

Keller, R. P., C. R. Allen, R. Gilman, N. R. Goulty, and J. A. Hileman (1978). Monitoring slip along major faults in southern California, Bull. Seism. Soc. Am., 68, 1187-1190.

Kerr, R. A. (1981). Palmdale Bulge doubts now taken seriously, Science, 214, 1331-1333.

King, N. E. and J. C. Savage (1982). Strain-rate profile across the Elsinore, San Jacinto, and San Andreas faults near Palm Springs, California, Eos Trans. AGU, 63, 1106.

Knopoff, L., and J. O. Mouton (1975). Can one determine seismic focal parameters from the far-field radiation?, Geophys. J. R. Astron. Soc., 42, 591-606.

Kostrov, V. V. (1974). Seismic moment and energy of earthquakes and seismic flow of rock, Izv., Earth Physics, No. 1, 23-40. Translated by F. Goodspeed.

Lahr, J. C. and C. D. Stephens (1982). Alaska seismic zone: Possible example of non-linear magnitude distribution for faults, Earthquake Notes, 53, 66.

Langbein, J. O., M. F. Linker, A. McGarr, and L. E. Slater (1982). Observations of strain accumulation across the San Andreas fault near Palmdale, California, with a two-color Geodimeter, Science, 218, 1217-1219.

LeBras, R. (1981). A preliminary study for the inversion of strong

ground motion data from the 1979 Imperial Valley earthquake, Eos Trans. AGU, 62, 972.

Lee, W. H. K., and J. C. Lahr (1975). HYPO71 (revised): A computer program for determining hypocenter, magnitude, and first motion pattern of local earthquakes, U. S. Geol. Surv. Open File Rep. 75-311, 114 pp.

Lee, W. H. K., R. F. Yerkes, and M. Simirenko (1979). Recent earthquake activity and focal mechanisms in the western Transverse Ranges, California, U. S. Geol. Surv. Circ. 799, 1-26.

Lockner, D. A., J. B. Walsh, and J. D. Byerlee (1977). Changes in seismic velocity and attenuation during deformation of granite, J. Geophys. Res., 82, 5374-5378.

Madariaga, R. (1976). Dynamics of an expanding circular fault, Bull. Seism. Soc. Am., 66, 639-666.

Madariaga, R. (1979). On the relation between seismic moment and stress drop in the presence of stress and strength heterogeneity, J. Geophys. Res., 84, 2243-2250.

Marion, G. E., and L. T. Long (1980). Microearthquake spectra in the southeastern United States, Bull. Seism. Soc. Am., 70, 1037-1054.

Mark, R. K., J. C. Tinsley, E. B. Newman, T. D. Gilmore, and R. O. Castle (1981). An assessment of the geodetic measurements that define the southern California uplift, J. Geophys. Res., 86, 2783-2808.

McGarr, A. (1981). Analysis of peak ground motion in terms of a model

of inhomogeneous faulting, J. Geophys. Res., 86, 3901-3912.

McGarr, A., R. W. E. Green, and S. M. Spottiswoode (1981). Strong ground motion of mine tremors: Some implications for near-source ground motion parameters, Bull. Seism. Soc. Am., 71, 295-319.

McHugh, C. A. and Lester, F. W. (1978). Catalog of earthquakes along the San Andreas fault system in central California for the year 1976, U. S. Geol. Surv. Open File Rep. 78-1051, 91 pp.

McKenzie, D. P. (1969). The relation between fault plane solutions for earthquakes and the directions of the principal stresses, Bull. Seism. Soc. Am., 59, 591-601.

McMechan, G. A., and W. D. Mooney (1980). Asymptotic ray theory and synthetic seismograms for laterally varying structures: Theory and application to the Imperial Valley, California, Bull. Seism. Soc. Am., 70, 2021-2035.

McNally, K. C., H. Kanamori, J. C. Pechmann, and G. Fuis (1978). Earthquake swarm along the San Andreas fault near Palmdale, southern California, 1976 to 1977, Science, 201, 814-817.

McNally, K. C. and T. V. McEvilly (1977). Velocity contrast across the San Andreas fault in central California: Small scale variations from P-wave nodal plane distortion, Bull. Seism. Soc. Am., 67, 1565-1576.

Mikumo, T. and T. Miyatake (1978). Dynamical rupture process on a three-dimensional fault with non-uniform friction and near-field seismic waves, Geophys. J. R. Astron. Soc., 54, 417-438.

Mikumo, T., and T. Miyatake (1983). Numerical modelling of space and

time variations of seismic activity before major earthquakes, submitted to Geophys. J. R. Astron. Soc.

Murdock, J. N. (1979). A tectonic interpretation of earthquake focal mechanisms and hypocenters in Ridge Basin, southern California, Bull. Seism. Soc. Am., 69, 417-425.

Murphy, L. M., ed. (1973). San Fernando, California, Earthquake of February 9, 1971, U. S. Department of Commerce, National Oceanic and Atmospheric Administration.

Nava, F. A. and J. N. Brune (1982). An earthquake-explosion reversed refraction line in the Peninsular Ranges of southern California and Baja California Norte, Bull. Seism. Soc. Am., 72, 1195-1206.

Nur, A. (1978). Nonuniform friction as a physical basis for earthquake mechanics, Pure Appl. Geophys., 116, 964-991.

Oakeshott, G. B., ed. (1975). San Fernando, California, Earthquake of 9 February, 1971, Calif. Div. of Mines and Geol. Bull. 196. Sacramento, Calif.

Pearson, C. (1981). The relationship between microseismicity and high pore pressures during hydraulic stimulation experiments in low permeability granitic rocks, J. Geophys. Res., 86, 7855-7864.

Pechmann, J. C., and H. Kanamori (1982). Waveforms and spectra of preshocks and aftershocks of the 1979 Imperial Valley, California, earthquake: Evidence for fault heterogeneity?, J. Geophys. Res., 87, 10579-10597.

Prescott, W. H. and J. C. Savage (1976). Strain accumulation on the San Andreas fault near Palmdale, California, J. Geophys. Res.,

81, 4901-4908.

Rader, C. M., and B. Gold (1967). Digital filter design techniques in the frequency domain, Proc. IEEE, 55, 149-171.

Raikes, S. A. (1978). Regional Variations in Upper Mantle Compressional Velocities Beneath Southern California, Ph.D. Thesis (Part I), Calif. Inst. of Technol., Pasadena, Calif.

Rautian, T. G., V. I. Khalturin, V. G. Martynov, and P. Molnar (1978). Preliminary analysis of the spectral contents of P and S waves from local earthquakes in the Garm, Tadjikistan Region, Bull. Seism. Soc. Am., 68, 949-971.

Reyners, M. (1981). Long- and intermediate-term precursors to earthquakes--State of the art, in Earthquake Prediction: An International Review, Maurice Ewing Ser., vol. 4, edited by D. W. Simpson and P. G. Richards, pp. 333-347, AGU, Washington, D. C.

Rial, J. A. (1978). The Caracas, Venezuela earthquake of July, 1967: A multiple source event, J. Geophys. Res., 83, 5405-5414.

Richter, C. F. (1958). Elementary Seismology, 768 pp., W. H. Freeman, San Francisco, Calif.

Rodgers, D. A., and M. A. Chinnery (1973). Stress accumulation in the Transverse Ranges, southern California, in Proceedings of the Conference on Tectonic Problems of the San Andreas Fault System, edited by R. L. Kovach and A. Nur, pp. 70-79, Stanford University Publications in the Geological Sciences, Vol. 13, Stanford University Press, Palo Alto, Calif.

Rudnicki, J. W., and H. Kanamori (1981). Effects of fault interaction

on moment, stress drop, and strain energy release, J. Geophys. Res., 86, 1785-1793.

Saito, K., and T. Masuda (1981). Precursory change of spectral characteristics before the 1978 Miyagiken-oki earthquake, Sci. Rep. Tohoku Univ., Ser. 5, 27, 95-109.

Sato, T., and T. Hirasawa (1973). Body wave spectra from propagating shear cracks, J. Phys. Earth, 21, 415-431.

Sanders, C. O., and H. Kanamori (1983). A seismotectonic analysis of the Anza seismic gap, San Jacinto fault zone, southern California, preprint, Seismological Lab., Calif. Inst. of Technol., Pasadena, Calif.

Sauber, J., K. McNally, J. C. Pechmann, and H. Kanamori (1983). Seismicity near Palmdale California, and its relation to strain changes, J. Geophys. Res., in press.

Savage, J. C. (1966). Radiation from a realistic model of faulting, Bull. Seism. Soc. Am., 56, 577-592.

Savage, J. C. (1972). Relation of corner frequency to fault dimensions, J. Geophys. Res., 77, 3788-3795.

Savage, J. C., W. H. Prescott, M. Lisowski, and N. King (1978). Strain in southern California: Measured north-south regional contraction, Science, 202, 883-885.

Savage, J. C., W. H. Prescott, M. Lisowski, and N. E. King (1981a). Strain accumulation on the San Andreas fault near Palmdale, California: Rapid, aseismic change, Science, 211, 56-58.

Savage, J. C., W. H. Prescott, M. Lisowski, and N. E. King (1981b).

Strain accumulation in southern California, 1973-1980, J. Geophys. Res., 86, 6991-7002.

Scholz, C. H. (1982). Scaling laws for large earthquakes: Consequences for physical models, Bull. Seism. Soc. Am., 72, 1-14.

Sharp, R. V. (1965). Geology of the San Jacinto Fault Zone in the Peninsular Ranges of Southern California, Ph.D. Thesis, Calif. Inst. of Technol., Pasadena, Calif.

Sharp, R. V. (1967). San Jacinto fault zone in the Peninsular Ranges of southern California, Bull. Geol. Soc. Am., 78, 705-730.

Sharp, R. V. (1975). En echelon fault patterns of the San Jacinto fault zone, in San Andreas Fault in Southern California, edited by J. C. Crowell, Calif. Div. Mines Geol. Spec. Rep. 118, 147-152.

Sharp, R. V. (1976). Surface faulting in Imperial Valley during the earthquake swarm of January-February, 1975, Bull. Seism. Soc. Am., 66, 1145-1154.

Smith, R. B., P. L. Winkler, J. G. Anderson, and C. H. Scholz (1974). Source mechanisms of microearthquakes associated with underground mines in eastern Utah, Bull. Seism. Soc. Am., 64, 1295-1317.

Spieth, M. A., and R. J. Geller (1981). Precise relative locations of local earthquakes near San Juan Bautista, California, Eos Trans. AGU, 62, 958.

Spottiswoode, S. M. and A. McGarr (1975). Source parameters of tremors in a deep-level gold mine, Bull. Seism. Soc. Am., 65,

93-112.

Stauder, W., and A. Ryall (1967). Spatial distribution and source mechanism of microearthquakes in Central Nevada, Bull. Seism. Soc. Am., 57, 1317-1345.

Stewart, G. S., and H. Kanamori (1982). Complexity of rupture in large strike-slip earthquakes in Turkey, Phys. Earth. Planet. Int., 28, 70-84.

Stewart, R. R., and M. N. Toksoz (1983). Strain-dependent attenuation: Observations and a proposed mechanism, J. Geophys. Res., 88, 546-554.

Stierman, D. J., and W. L. Ellsworth (1976). Aftershocks of the February 21, 1973, Point Mugu, California, earthquake, Bull. Seism. Soc. Am., 66, 1931-1952.

Strange, W. E. (1981). The impact of refraction correction on leveling interpretations in southern California, J. Geophys. Res., 86, 2809-2824.

Thatcher, W., (1972). Regional variations of seismic source parameters in the northern Baja California area, J. Geophys. Res., 77, 1549-1565.

Thatcher, W., and R. M. Hamilton (1973). Aftershocks and source characteristics of the 1969 Coyote Mountain earthquake, San Jacinto Fault Zone, California, Bull. Seism. Soc. Am., 63, 647-661.

Thatcher, W., and T. C. Hanks (1973). Source parameters of southern California earthquakes, J. Geophys. Res., 78, 8547-8576.

Thatcher, W., J. A. Hileman, and T. C. Hanks (1975). Seismic slip

distribution along the San Jacinto fault zone, southern California, and its implications, Geol. Soc. Am. Bull., 86, 1140-1146.

Tsujiura, M. (1979a). The difference between foreshocks and earthquake swarms, as inferred from the similarity of seismic waveform (in Japanese), Bull. Earthquake Res. Inst., Tokyo Univ., 54, 309-315.

Tsujiura, M. (1979b). Mechanism of the earthquake swarm activity in the Kawanazaki-oki, Izu Peninsula, as inferred from the analysis of seismic waveforms, Bull. Earthquake Res. Inst., Tokyo Univ., 54, 441-462.

Tsumura, K., I. Karakama, I. Ogino, and M. Takahashi (1978). Seismic activities before and after the Izu-Oshima-Kinkai earthquake of 1978 (in Japanese), Bull. Earthquake Res. Inst., Tokyo Univ., 53, 675-706.

Tucker, B. E., and J. N. Brune (1973). Seismograms, S-wave spectra, and source parameters for aftershocks of the San Fernando Earthquake, in San Fernando, California, Earthquake of February 9, 1971, edited by L. M. Murphy, pp. 69-121, U. S. Department of Commerce, National Oceanic and Atmospheric Administration, Washington, D. C.

U. S. Geological Survey (1971). The San Fernando, California, earthquake of February 9, 1971, U. S. Geol. Surv. Prof. Pap. 733, U. S. Government Printing Office, Washington, D. C.

U. S. Geological Survey (1972). The Borrego Mountain earthquake of April 9, 1968, U. S. Geol. Surv. Prof. Pap. 787, U. S. Government Printing Office, Washington D. C.

Von Seggern, D. (1980). A random stress model for seismicity statistics and earthquake prediction, Geophys. Res. Lett., 7, 637-664.

Wallace, T. C., D. V. Helmberger, and J. E. Ebel (1981). A broadband study of the 13 August 1978 Santa Barbara earthquake, Bull. Seism. Soc. Am., 71, 1701-1718.

Weinberger, H. F. (1965). A First Course in Partial Differential Equations, 446 pp., Xerox College Publishing, Lexington, Ky.

Wesnousky, S. G., C. H. Scholz, K. Shimazaki, and T. Matsuda (1983). Earthquake frequency distribution and the mechanics of faulting, preprint, Lamont-Doherty Geological Observatory of Columbia University, Palisades, N. Y.

Wesson, R. L., R. Robinson, C. G. Bufe, W. L. Ellsworth, J. H. Pfluke, J. A. Steppe, and L. C. Seekins (1977). Search for seismic forerunners to earthquakes in central California, Tectonophysics, 42, 111-126.

Whitcomb, J. H. (1973). The 1971 San Fernando Earthquake Series Focal Mechanisms and Tectonics, Ph.D. Thesis (Part II), Calif. Inst. of Technol., Pasadena, Calif.

Whitcomb, J. H. (1978). P and S-phase data from local earthquakes in southern California for 1966 to 1975, Bull. Seism. Soc. Am., 68, 523-525.

Whitcomb, J. H., C. R. Allen, A. C. Blanchard, S. A. Fisher, G. S. Fuis, L. K. Hutton, D. J. Jenkins, C. E. Johnson, B. A. Reed, and K. J. Richter (1978). Southern California Array for Research

on Local Earthquakes and Teleseisms (SCARLET) Caltech-USGS Monthly Preliminary Epicenters for January 1977 to March 1978. Seismological Laboratory, Division of Geological and Planetary Sciences, Calif. Inst. of Technol., Pasadena, Calif.

Whitcomb, J. H., C. R. Allen, J. D. Garmany, and J. A. Hileman (1973). San Fernando earthquake series, 1971: Focal mechanisms and tectonics, Rev. Geophys. Space Phys., 11, 693.

Wu, F. T. (1980). Strength of fault zone materials above 15 km depth and tectonic stresses, in Proceedings of Conference IX, Magnitude of Deviatoric Stresses in the Earth's Crust and Upper Mantle, vol. II, U. S. Geological Survey, Menlo Park, Calif.

Wyss, M., and J. N. Brune (1967). The Alaska earthquake of 28 March 1964: A complex multiple rupture, Bull. Seism. Soc. Am., 57, 1017-1023.

Wyss, M., and J. N. Brune (1968). Seismic moment, stress, and source dimensions for earthquakes in the California-Nevada region, J. Geophys. Res., 73, 4681-4694.

Yerkes, R. F., and W. H. K. Lee (1979). Late Quaternary deformation in the western Transverse Ranges, California, U. S. Geol. Surv. Circ. 799, 27-37.

Zoback, M. D., H. Tsukahara, and S. Hickman (1980). Stress measurements at depth in the vicinity of the San Andreas fault: Implications for the magnitude of shear stress at depth, J. Geophys. Res., 85, 6157-6173.

Zoback, M. L. and M. Zoback (1980). State of stress in the

conterminous United States, J. Geophys. Res., 85, 6113-6156.